INVESTIGATIONS ON THE INFLUENCE OF DISK LOCATION AND UNBALANCE ON FLUID INDUCED VIBRATIONS OF A SHAFT-DISK-BEARING SYSTEM

BY

Ali M. Al-Shurafa

A Thesis Presented to the

DEANSHIP OF GRADUATE STUDIES

KING FAHD UNIVERSITY OF PETROLEUM & MINERALS

DHAHRAN, SAUDI ARABIA

In Partial Fulfillment of the
Requirements for the Degree of

MASTER OF SCIENCE

In

MECHANICAL ENGINEERING

June 2004

KING FAHD UNIVERSITY OF PETROLEUM AND MINERALS

DHAHRAN 31261, SAUDI ARABIA

DEANSHIP OF GRADUATE STUDIES

This thesis, written by

ALI M. AL-SHURAFA

under the direction of his thesis committee, has been presented and accepted by the Dean of Graduate Studies, in partial fulfillment of the requirements for the degree of

MASTER OF SCIENCE IN MECHANICAL ENGINEERING.

Thesis Committee

02/06/2004
Dr. Mehmet Sunar (Thesis Advisor)

١٤٢٥/٥/١٦
Dr. Yagoub Al-Nassar (Member)

05/06/2004
Dr. Muammer Kalyon (Member)

Dr. Faleh Al-Sulaiman
Department Chairman

Prof. Osama Ahmed Jannadi
Dean, Graduate Studies

7-6-2004
Date:

ACKNOWLEDGMENT

Acknowledgment is due to King Fahd University of Petroleum and Minerals for supporting this research. My deep and grateful appreciation goes to Dr. Mehmet Sunar, my thesis advisor for his help and guidance. My thanks are also due to the committee members: Dr. Yagoub Al-Nassar and Dr. Muammer Kalyon for their valuable comments and feedback.

This work could not have been achieved without the support I have received from my family members and close friends. I would like to thank them all.

TABLE OF CONTENTS

LIST OF TABLES

LIST OF FIGURES

THESIS ABSTRACT

Name: Ali Muhammed Ali Al-Shurafa
Title: Investigations on the Influence of Disk Location and Unbalance on Fluid Induced Vibrations of a Shaft-Disk-Bearing System
Field: Mechanical Engineering
Date: May 2004

Rotors mounted on fluid film bearings are suspected to experience fluid induced instabilities generating severe vibration problems. Fluid film bearings greatly contribute in the dynamic characteristics of these systems. Oil whirl and whip being the major examples of the fluid induced instabilities, they possess distinct and damaging symptoms (large forward circular precession with subsynchronous frequency).

In this thesis, the influence of rotor length, disk axial location and the disk unbalance on the fluid induced vibrations of a shaft-disk-bearing system is studied. Experiments on a rotor kit and numerical computations are carried out on the same setup. Shaft vibration data is collected and analyzed using standard instrumentations and computer software. This data is exported to spread sheet for further processing and extracting more results. In the numerical computations, a finite element software is used for mathematically modeling of the shaft, disk and bearings. The software has produced stiffness and damping maps for the bearings, the Campbell diagrams for the system and other plots used in the stability analysis.

Results indicate a clear increasing effect of the disk location on the stability threshold and instability frequency. The instability frequency of whip is affected clearly by the disk location. The disk location is the strongest factor among the three. The effect of shaft length is to decrease both threshold and the instability frequency. The shaft length and disk location do not have any noticeable effect on the instability amplitude. Although mass unbalance produces 1X order frequency vibration, this vibration influences the oil instability whose frequency is slightly less than 0.5X order. Explanation is found from the shaft average eccentricity ratio vector plots. The unbalance effect on the threshold is dependant on the disk location.

The shaft average eccentricity ratio plot shows that the system demands more conservative conditions to stabilize, after it gets into instability. The threshold order is not consistent in many cases. The relation between the rotor speed and instability is found to be linear despite of the ramp (startup or shutdown) in the transient conditions for the whirl instability.

MASTER OF SCIENCE DEGREE

KING FAHD UNIVERSITY OF PETROLEUM AND MINERALS

DHAHRAN, SAUDI ARABIA

ملخص الرسالة

الاسم: علي بن محمد بن علي الشرفاء

عنوان الرسالة: أبحاث حول موقع القرص و عدم الاتزان على الاهتزازات الناتجة عن المانع على عمود و قرص و حامل

التخصص: هندسة ميكانيكية

تاريخ الشهادة: يونيو 2004

ملخص البحث

إن أعمدة المعدات الدوارة المحمولة على حوامل سائلة تكون معرضة لحالات عدم استقرار بسبب سائل الحامل مما يؤدي لاهتزازات خطيرة. تساهم الحوامل السائلة بشكل أساسي في الخصائص الديناميكية لهذه المعدات أو الأنظمة. تمثل حالتي "الويب" و الورل" أهم حالات عدم الاستقرار هذه، كما أنهما تتميزان بسمات خاصة، منها أن تكون الاهتزازات عالية و في نفس اتجاه الدوران، و دائرية و لها تردد أقل من سرعة المعدة نفسها.

في هذه الرسالة، دُرست التأثيرات التالية على هذه النوعية من الاهتزازات: طول العمود و موقع القرص و عدم اتزانه. وقد أجريت تجارب عملية و حسابية في الوقت ذاته لنفس الهيكل تم فيها نقل إشارات اهتزازات العمود و حللت باستخدام أجهزة دقيقة و برنامج خاص. كما تم دراسة بيانات الاهتزازات واستخلاص النتائج. في الجزء الحسابي، استخدم الحاسب الآلي لمحاكاة الهيكل المكون من العمود و القرص و الحوامل. و كانت من مخرجات البرنامج رسومات بيانية موضحة للخصائص الديناميكية للحوامل و تحليل لمدى الاستقرار.

تشير النتائج الى وجود ارتفاع في مدى استقرار النظام و تردد الاهتزازات المصاحبة، مع تغيير موقع القرص. و كان لموقع القرص أثر واضح على ظاهرة "الوب". و من بين العوامل الثلاثة المدروسة، كان موقع القرص وهو الأكثر تأثيرا. لم يكن لطول العمود و عدم اتزان القرص أثر واضح على مقدار عدم الاستقرار. لكن رغم أن تردد عدم الاتزان هو 1X فقد كان له تأثير على عدم الاستقرار الذي ترده 0.5X. إحدى الرسومات المستخلصة لإشارات الاهتزازات تفسر هذه الظاهرة. يلاحظ إيضا أن بدأ حالة عدم الاستقرار مرتبطة بموقع القرص.

الرسم البياني لمعدل موقع العمود في خلوص الحامل يظهر أن النظام يحتاج إلى شروط أكثر صرامة ليتمكن من العوده إلى حالة الاستقرار، بعد أن يدخل إلى حالة عدم الاستقرار. تين النتائج أنه في حالة "الورل"، العلاقة بين سرعة العمود و تردد الاهتزازات علاقة خطية، بغض النظر عن كون السرعة تصاعدية أو تناقصية.

درجة الماجستير في العلوم

جامعة الملك فهد للبترول و المعادن

الظهران-المملكة العربية السعودية

Nomenclature

e: Eccentricity
h: Fluid film thickness
l: Shaft length
l': disk axial location
m: Mass
m_u: Unbalance mass
r: Radial direction *or* radius of m_u
t: Tangential direction
t: Time
x: Horizontal direction or displacement
y: Vertical coordinate
z: Axial coordinate *or* location

C: Clearance (radial)
CDS: Complex dynamic stiffness
$D(n)x$: Vibration displacement in the x-direction of station n
D: Damping
D: Diameter (of bearing or shaft)
F: Force
F_{max}: Maximum spectral frequency
H: Film thickness ratio
K: Stiffness
L: Length (of journal)
M: Mass (of rotor)
N: Shaft speed
P: Pressure (of lubricant fluid film)
R: Radius (of journal or bearing)
S: Sommerfeld Number
V: Velocity
W: Weight (on the journal)
X: Vibration frequency order

α: Velocity angle
ε: Shaft average eccentricity ratio
θ: Film thickness angle
λ: shaft average circumferential velocity ratio
μ: Oil viscosity
ρ: Lubricant density
σ: Modified Sommerfeld Number
τ: Sheer stress
φ: Journal attitude angle
ω: Frequency (natural or excitation)
Ω: Shaft speed

CHAPTER 1

INTRODUCTION

1.1 Background

This thesis is a study on *Fluid Induced Instabilities* which are damaging problems faced in large rotating machinery mounted on fluid film bearings, e.g., production turbines and compressors. The vibration of these problems is a substantial concern for industry because it limits the safe and efficient equipment operation. *Fluid Induced Vibrations* are self excited and include variant categories like: *Oil Whirl, Oil Whip*, Subsynchronous Resonance, Stall and others [1-5]. All these problems have common symptoms. Figures 1 below categorizes the instabilities based on the location in the machine itself.

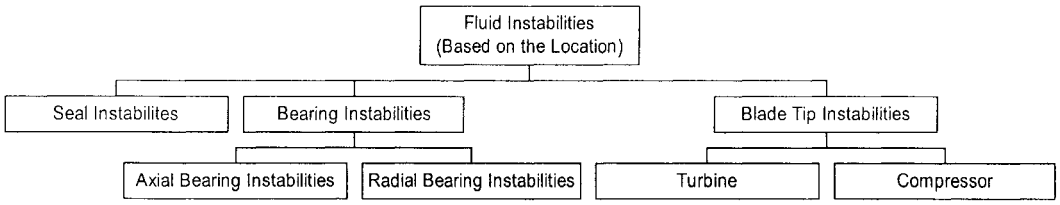

Figure 1-1 Instability based on location

In this chapter, thesis objectives and approach are highlighted and a literature review is given.

1.2 Objectives and Approach

This research concentrates on the most important case of the fluid induced instability: the vibrations generated in the radial fluid film bearings (Figure 1-1). The main goal of this research is to study the changes of vibration signature of a

shaft-disk-bearing system under different conditions of the disk axial location, shaft length and disk mass unbalance.

The approach to meet these objectives is through experimental and computational work. Hence, the report is arranged as follows:

- Conducting a series of experiments to acquire real vibration data of a rotor kit under the instability conditions. This data covered both steady-state and transient conditions. The data is processed and then analyzed using a standard software, and then is exported to spread sheets for further processing and analysis.

- Application of the existing analytical or numerical solutions to estimate the system's parameters to be studied in this work. The output of this part covers stiffness, damping and natural frequencies. The *Threshold of Instability* and the instability vibration amplitude will be studied as a result of the changes.

- Compiling and comparing the results found from different arrangements and deducing some concrete conclusions.

1.3 Literature Review

Though the problem of fluid induced instability was discovered before the 1950's, it remained of a great interest due to the industrial nature of this problem. Some progress in understanding and modeling the problem was found after the improvement in computers, vibration measuring instrumentation and analysis software, which were not well developed in those days.

In 1974, Lund published a paper proposing a model for flexible rotor instability [6] based on earlier papers by him and others [7,8]. The published works agreed on describing the fluid induced vibration problems as self-excited type of vibration. There is, however, a disagreement among the researchers and authors in explaining and relating relationships between rubbing, poorly lubricated bearings, insufficient preload and whirl/whip, due to the large number of factors affecting the dynamics of the fluid induced instabilities [1]. Usually oil whirl and oil whip are referred to as main examples of fluid induced instability. However, Elshman differentiated between these two instabilities and other types [9].

Modeling of bearing mechanical properties were investigated in a series of publications and books, which attempt to explain the transient rotor response with respect to the fluid film bearing properties [10-13].

The diagnostic symptoms of the oil whir/whip vibrations are given in [14] and can be summarized as:

1) High amplitudes, reaching to machine's danger limits.

2) Subsynchronous frequency, noticed in the frequency spectrum.

3) Circular or nearly circular orbits.

4) Forward precession, noticed in the full spectrum plots.

The actual value of the high amplitude generated by whirl/whip problems is dependent on the machine design and dimensions. Computational Systems Inc. (CSI) and Bently Nevada [15,16] recommend that the maximum allowable vibration amplitude of subsynchronous vibration is to be set less than the synchronous maximum allowable vibration amplitudes. A subsynchronous frequency, ω, is the one whose value is less than the value of the shaft running frequency , Ω, i.e., $\Omega > \omega$.

Many authors, especially associated with Bently Nevada Research Center, state that the order of vibration (vibration frequency to the shaft speed frequency ratio) is dependent heavily on the fluid circumferential velocity ratio [1,2,14,17] which is usually less than 0.5. According to the reference [18], the second symptom can be relaxed and oil instability may exist at a frequency even higher than the shaft speed.

Forward precession is an orbiting of the shaft about a center point, in the same direction of the shaft normal rotation. This symptom distinguishes oil instability from some common rubbing problems [4,5,14,18].

Though the fluid induced instabilities can be recognized in the steady-state conditions, the symptoms addressed above can be easily noticed from the transient condition plots (start up or shutdown). This is why most references use *cascade* plot in their presentation and discussion.

The factors affecting oil instability and their solutions drew interest in research and industrial community. Some of these solutions are highlighted in Chapter 2. Many of these solutions are not practical or have limitations. For example, a solution applied on bearing instability may not work for the seal fluid instability, e.g. seals cannot be grooved. Bearing factors such as clearance and anti-swirl were studied in [17-22]. Perturbation force technique was used in some works [23-25]. Muszynska interpreted phase angle changes of some instability problems as changes in modes of the instability vibration [26].

Complex Dynamic Stiffness (CDS) is relatively a new concept in rotor dynamics. Extension of the applications of the CDS was developed by Bently Nevada Rotor Dynamics Research Center [1,14,27]. Numerous works related to this subject were written by A. Muszynska and D. E. Bently. The CDS allowed a better understanding of rotor dynamics in general and fluid induced vibrations in

particular. However, treating the instability problems using the CDS is not widely used.

It is noticed that the effects of the mass unbalance, shaft length and the disk location along the shaft on the instability have not been given enough attention in the literature. There are no clear conclusions of these parameters on the stability threshold or instability amplitude. Understanding these factors and their effects is expected to be beneficial to both design and analysis sides of the instability problems. Therefore this research is undertaken to study these factors as related to fluid induced vibration problems in rotating machinery.

CHAPTER 2

BACKGROUND ON FLUID INDUCED INSTABILITIES

2.1 Introduction

The objective of this chapter is to establish the basis for the experimental and theoretical work for dynamics of a shaft-disk-bearing system. Hence, the rotordynamics basics for the system under consideration is presented. Then, the vibration caused by the instability of oil whirl and whip is explored. The last part of this chapter explains the facts behind approaches of the instability cures.

2.2 Rotor-bearing modeling

Fluid induced vibrations are heavily related to the natural frequencies of rotor systems. For a simple spring-mass-damper system (Figure 2-1), the characteristic equation and natural frequency are given as follows:

$$m\ddot{x} + c\dot{x} + kx = f(t) \tag{2-1}$$

$$\omega = \sqrt{\frac{k}{m}} \tag{2-2}$$

where m is the mass, c is the damping, k is the stiffness and $\ddot{x}, \dot{x}$ and x are the acceleration, velocity and displacement, respectively and ω is the natural frequency, which is constant, in this simple model.

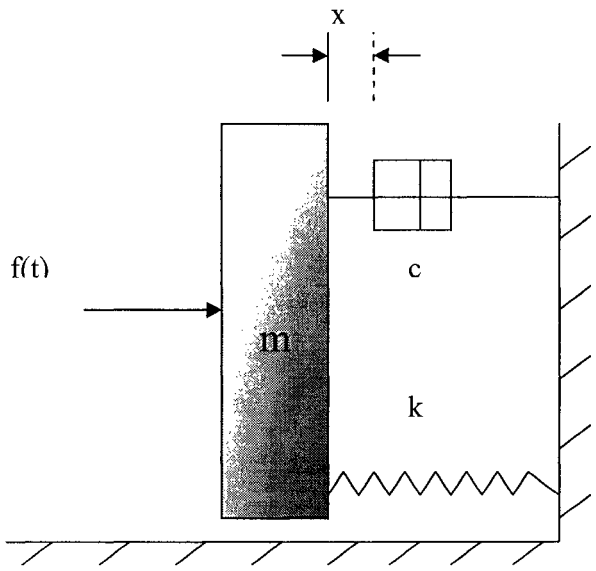

Figure 2-1 Mass-spring-damper system

Researchers developed simplified models for shaft-disk bearing systems like the one in Figure 2-2, where K_y is the bearing stiffness and Ω is the shaft speed. If an actual rotor is modeled, more complicated formulas and calculations are involved. The analysis of a rotor-bearing system, in addition to the rotor setup, depends greatly on the bearing details (type, dimensions, loading etc). Fluid film bearings, by softening the system, will reduce the natural frequency of the system and they also force the natural frequency to be speed dependent. The accurate modeling of the system is not an easy task especially if the rotor is mounted on fluid film bearings.

Figure 2-3 is a *natural frequency map* drawn for a real case rotor. Notice that because the fluid film bearing has a varying nature based on the operating conditions (e.g., load and shaft speed), the entire system will have a varying natural frequency map as well.

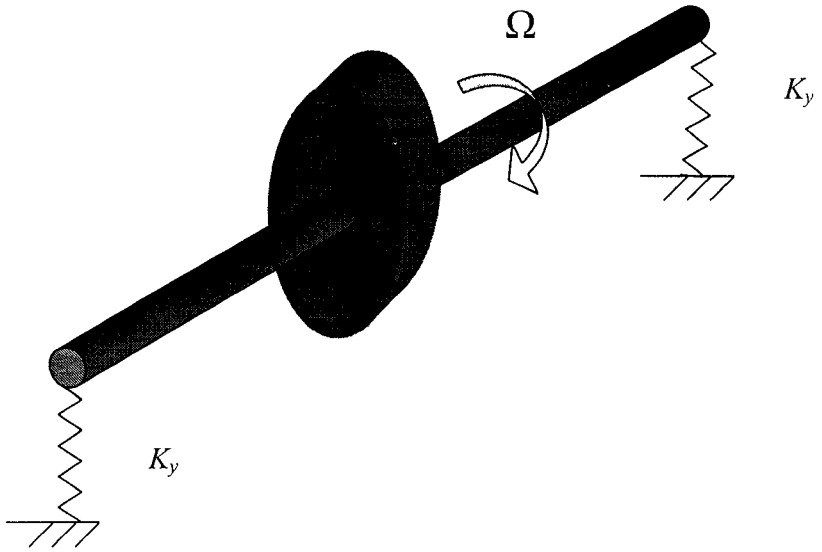

Figure 2-2 Simplified shaft-disk-bearing system

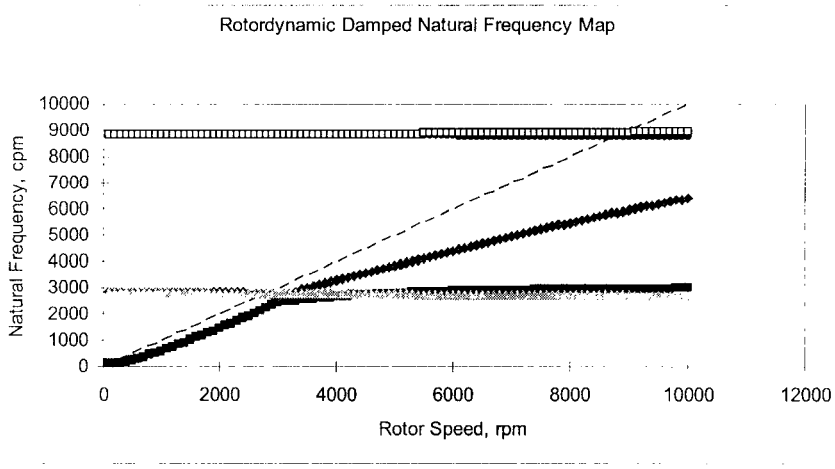

Figure 2-3 Frequency interference chart (Campbell)

In modeling an actual rotor, the bearings are considered as springs with variable stiffness. Figure 2-2 illustrates this idea if only the vertical stiffness K_y is considered. As will be seen in the theoretical part, the fluid film bearing is modeled with four stiffness components, which is widely accepted as a reasonable approximation. A direct reflection of bearing stiffness and damping properties is expected on the fluid induced vibrations.

2.3 Unbalance Force

When an amount of mass, m_u, is mounted at a distance, r, from the center of rotation of a rotating disk, it produces a radial synchronous force, F. The magnitude of the force is a function of the rotational speed according to the following formula:

$$F = m_u r \Omega^2 \tag{2-3}$$

where Ω is the rotational speed. This force induces a whirling action pushing the shaft journal to move away from the bearing center.

Though the unbalance force produces a synchronous vibration, it has been noticed that it also affects the subsynchronous vibration due to the fluid induced instability. This will be shown in the experimental part. The reason behind the mentioned effect is that the unbalance forces affect the dynamic properties of the fluid film bearing by changing *loading* and *eccentricity*. An important case is when the unbalance force excites the system's response at the critical speed. In this instance, the journal will move with a larger eccentricity in the bearing increasing the bearing load dynamically.

Consider the rotor illustrated in Figure 2-4. The response due to the unbalance force will not only depend on the unbalance mass, m_u, but it also depends on the rotor mass, M. The balancing standard ISO 1940-1 [28] provides details on this subject and some calculations on this subject are presented in Chapter 3.

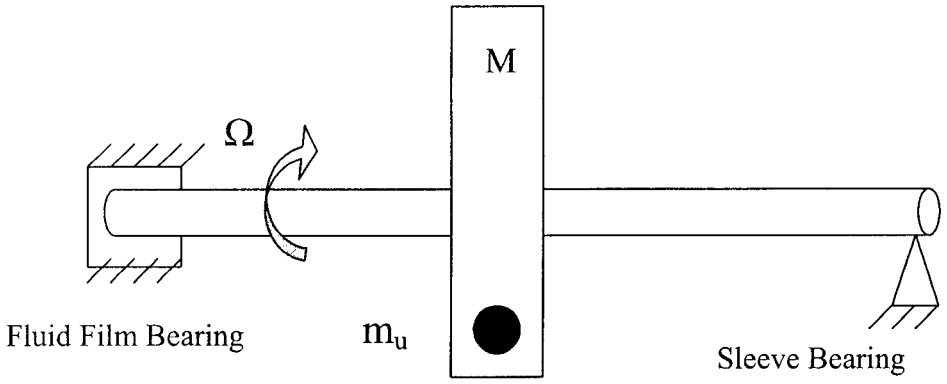

Figure 2-4 Unbalanced rotor

2.4 Nonlinearity

A major complexity faced in analyzing the oil whirl and whip problems is the nonlinearity of the dynamic properties of the system. Most of the nonlinearities in the oil whirl and whip vibrations come from the fluid film bearing.

In a linear system, the output response is directly proportional to the input excitation (as in Figure 2-1). For instance, the response displacement of the mass location in the simple mass-spring damper system is directly proportional to the magnitude of the applied force. Unbalance response in the absence of the fluid induced vibrations can be considered linear unlike a rotating system running under fluid induced vibrations [7,22,25].

To simulate the nonlinear fluid film bearing response, Figure 2-5 is provided. The mass *M* resembles the rotor mass and the mass location is the position of the journal inside the bearing clearance circle while the springs resemble the fluid film stiffness. When the mass moves to the left under a known force, the response could be predicted and its prediction is valid throughout the entire stroke, because x-displacement is dependent on x. However, if the same force is applied to the right, the system displacement response will be nonlinear because

it is dependent not only on the applied force but also on the location (which is the system response). In other words, the response depends on the force magnitude and direction, and these will result in deciding which springs will be compressed. A similar interpretation is valid for velocity response and the damping.

The simple model illustrated in Figure 2-5 is analogous to the scenario of the stiffness of the fluid film bearings (Figure 2-6). Shaft *eccentricity* is measured using shaft location inside the bearing. Shaft's eccentricity depends on the clearance between the shaft and the bearing. This is discussed later as an important parameter in rotordynamics and controlling the oil whirl and whip instabilities.

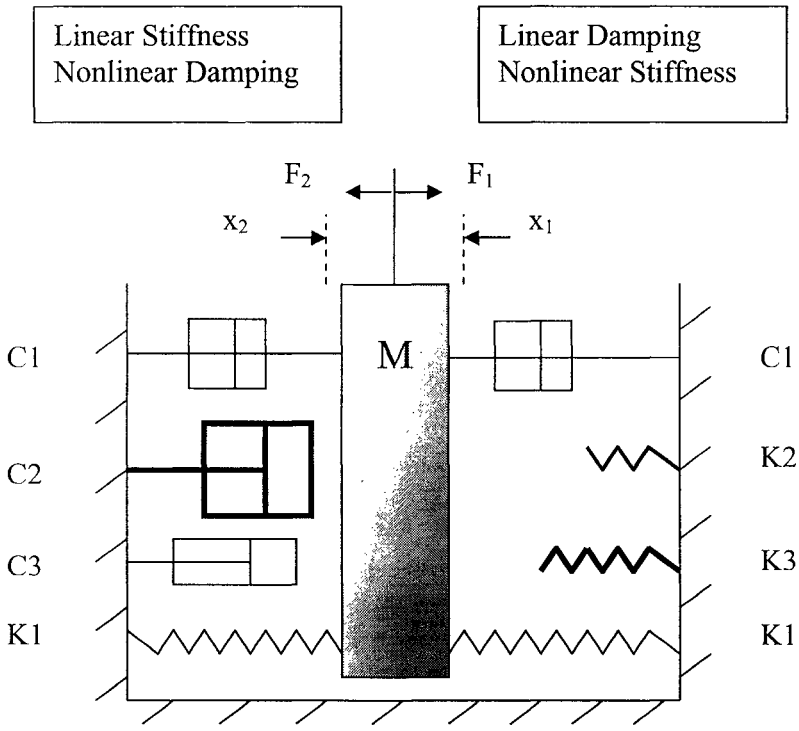

Figure 2-5 Model for a nonlinear system

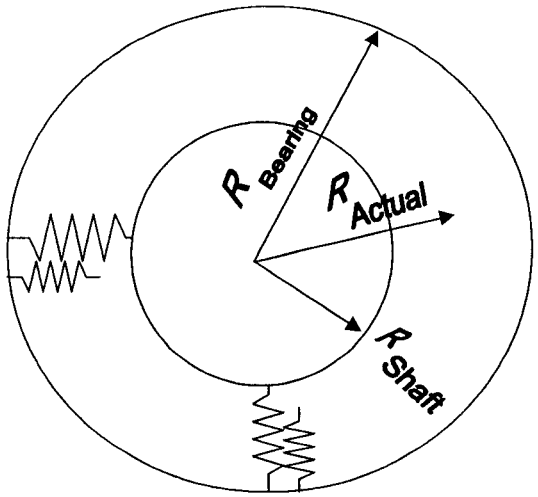

Figure 2-6 Explanation of nonlinearity of fluid film

2.5 Complex Dynamic Stiffness

From traditional theory of rotor dynamics, the whole machine stiffness is contributed by the shaft and bearing spring stiffnesses. And theoretically speaking, the amplification of the response at *resonance* will reach infinity because there are no resisting forces (stiffness) to absorb the excitation.

The *CDS* gives a deeper understanding of the rotor dynamics compared to the description given by the traditional stiffness. The CDS theory introduces the damping as a contributor to the system stiffness, which explains the ability of the system to withstand (to an extent) the vibration at resonance [2,3].

The core concept states that the total stiffness of a rotor is composed of two parts: real and imaginary. It is described as dynamic because its value is speed dependant. Thus, the rotor vibration can be defined as the system response due to the resultant forces applied on the system's CDS as given in Equation (2-4).

$$Rotor\ Response = \frac{Input\ Force}{CDS} \tag{2-4}$$

where $CDS = K_D + K_Q$ (2-5)

and where K_D and K_Q are called the direct and quadrature stiffnesses and are given as

$$K_D = K - M\omega^2 + K_B \tag{2-6}$$

and

$$K_Q = j[\omega(D_s + D) - D\lambda\Omega]. \tag{2-7}$$

In Equations (2-6) and (2-7) K is the system stiffness away from the bearing, M is the rotor mass, ω is the perturbation frequency, K_B is the bearing stiffness, D_s is the shaft damping, D is the bearing damping, λ is the *fluid average circumferential velocity ratio* and $j = \sqrt{-1}$ [2].

The oil whirl and oil whip arise when both direct and quadrature stiffnesses reduce to zero. K_B is very much dependent on the geometry of the fluid film bearing and the existence of external forces like preload or unbalance.

2.6 Fluid Average Circumferential Velocity Ratio

The *average circumferential velocity ratio (ACVR)*, λ, is a crucial parameter in controlling the rotor whirl/whip stability. It describes the complex motion of the lubricant through the annular area of the bearing clearance. This section will demonstrate its physical and mathematical significance on the fluid induced vibrations.

The fluid *average circumferential velocity* is a representative velocity of oil in the bearing clearance area which depends on the velocity profile. Typically, the oil weighted velocity average is less than the linear velocity average because of the physical behavior of the oil. The oil velocity profile tends to concave toward the linear behavior (see Figures 2-7 and 2-8).

The λ is a non-dimensional ratio of the fluid average circumferential velocity to the shaft velocity. Mathematically:

$$\lambda = \text{average circumferential velocity/shaft velocity} \tag{2-8}$$

The value of λ is dependent on many factors including the oil properties (e.g. viscosity and oil inlet pressure) and the geometry of the oil passage in the bearing (e.g. shaft eccentricity).

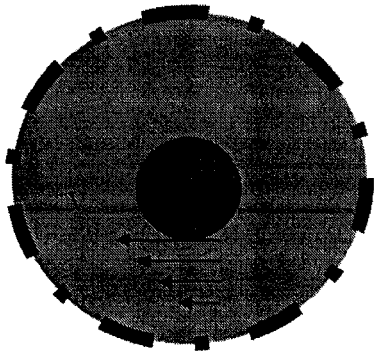

Figure 2-7 Effect of shaft speed on oil velocity

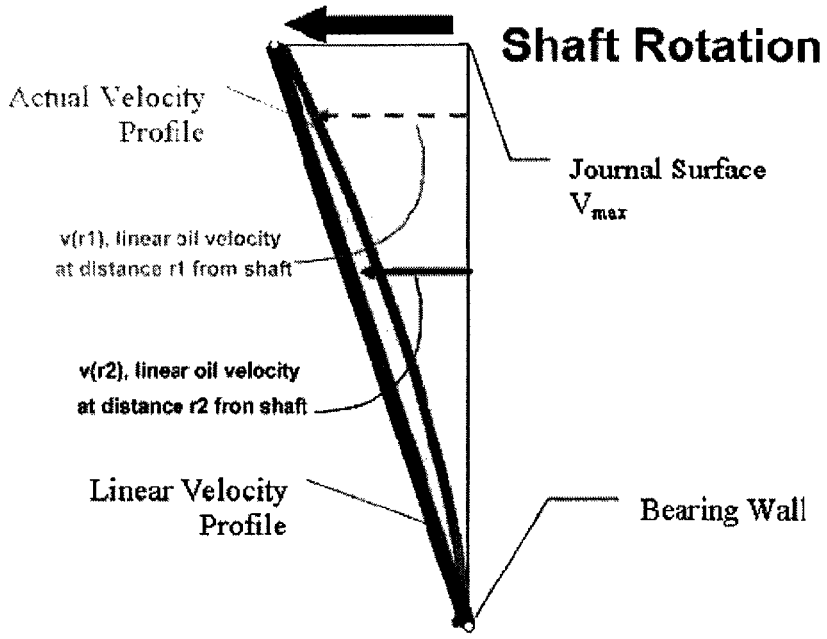

Figure 2-8 Oil velocity profile in the fluid film bearing

Consider the following three cases. First, λ is zero if the oil is not rotating relative to the shaft rotation. Second, λ is in the range of $0.43<\lambda<0.49$, where the oil whirl and whip may occur under certain conditions. Third, $1<\lambda$ which takes place when the lubricant velocity is greater than the shaft velocity (e.g. the oil flow rate coming from the forced lubrication system is very large).

2.7 Dynamics of Whirl and Whip

2.7.1 Interaction of Natural Frequencies

Machines mounted on radial fluid film bearings have two types of resonance: mechanical and fluid. The natural frequency of the whole system (not only the shaft) will be affected by the interaction of three elements: rotor, oil film and bearing. These elements are partially mechanical (solid materials) and partially fluid (lubrication oil).

The mechanical characteristics related to the rotor, e.g. the shaft mass, are generally speed independent while the fluid characteristics related to the fluid film bearing, e.g. the oil film thickness, are generally speed dependent. Notice the vibration frequency change in Figure 2-9. The natural frequency is changing as will be seen in the frequency maps. In the transient state, the instability frequency (in cpm) may be changing while frequency order (in nX where X is the shaft speed) is constant. The vice versa is also possible.

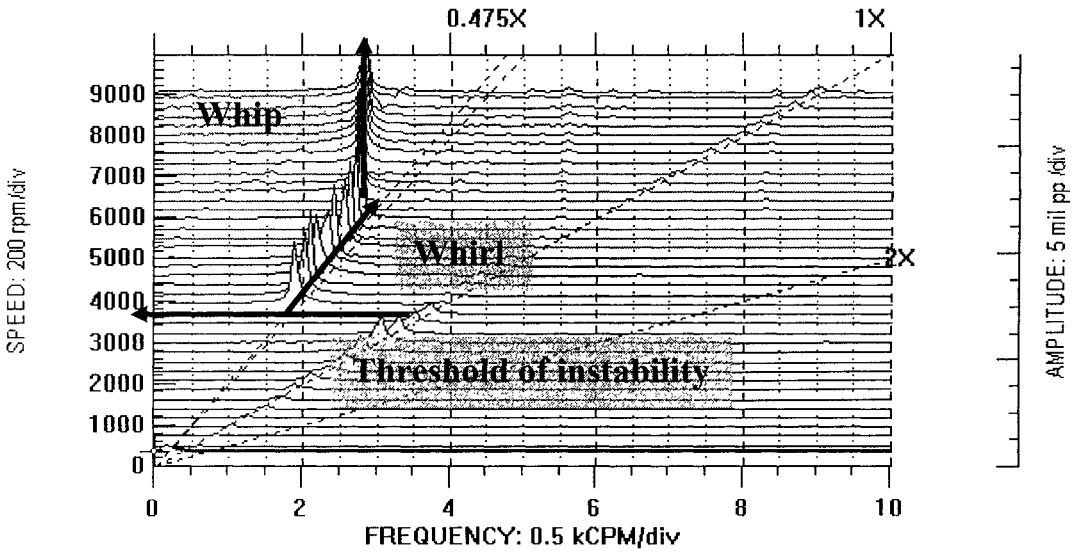

Figure 2-9 Cascade plot of instability

Typically, during the start up, the instability starts as the oil whirl. As the speed increases, the whirl continues and then converts into the oil whip thereafter. Though it is not unusual to notice that the whip follows the whirl, the mechanism of transition from the whirl to the whip has not been given sufficient attention so far.

The resonance of the whip occurs when the mechanical natural frequency of the rotor is excited by a subsynchronous excitation. Because the mechanical natural frequency is not dependent on the speed, the whip vibration frequency is independent of the rotor speed (i.e. the oil whip vibration frequency remains invariable even if the rotor speed is increased).

The resonance of the oil whirl occurs, however, when the fluid-related natural frequency of the rotor is excited. The (fluid-related) natural frequency of the rotating system increases as the rotor speed increases and hence the excitation frequency and the natural frequency coincide over a range of rotor speed, i.e. the whirl vibrations continue to be active as the rotor speed increases *at increasing frequency*. This can be illustrated clearly in the cascade plot, Figure 2-9. In this figure, it is noticed that the whirl amplitudes are active at an order line (about 0.5X). The whip frequency is basically constant with speed *(decreasing frequency order)*. The whip vibrations continue as the rotor speed increases but at *constant frequency*.

Remember that the natural frequency of a machine mounted on a fluid film bearing found by the impact test may not be representative and may not be accurate for such machines because it gives only the natural frequency at static conditions and for the mechanical components only. Impact test results are taken, actually, for bearing with the minimum fluid film thickness, possibly zero thickness, with no gyroscopic and no other dynamic or operational effects. This explains why a natural frequency value collected by an impact test varies sometimes from that observed while the machine is running during start up. To compensate this deficiency, frequency interface charts (natural frequency maps) are developed. These charts provide the machines natural frequencies as a function of the rotor speed and with a normal fluid film thickness. An example was given before in Figure 2-3.

2.7.2 Dynamics of Whirl and Whip

From cascade plots, it can be noticed that the whirl (or directly the whip) starts at a certain rpm and continues. The threshold of instability is a common term used to define the instability starting speed in rpm. For example, in the cascade plot of Figure 2-9, the instability threshold of the whirl is about 4100 rpm.

The oil whip is mainly influenced by the mechanical characteristics, which are, again, generally independent of the shaft rotational speed. Notice in the cascade plot of Figure 2-9 that the whip frequency is almost constant at about 2750 cpm. This value did not vary even if the shaft speed was increased from 6800 rpm to 9000 rpm.

On the other hand, the whirl frequency order is constant at about 0.45X since the instability has started at 3800 rpm up to the conversion of the instability to the whip at 6800 rpm. The oil whirl is mainly influenced by the fluid-related characteristics, which are, again, generally speed dependent. Table 2-1 below compares the whirl and the whip. Notice that the terms threshold of instability and stability threshold are both used in this thesis and refer to the same phenomenon.

Table 2-1 Whirl-Whip comparison

Instability	**Frequency**	**Order**
Whirl	Increasing	Constant
Whip	Constant	Decreasing

2.7.3 Instability Vibration Control

To control the fluid induced vibrations, the concept of resonance tuning (separating running speed from the natural frequency) is implicitly applied. The heart of the methods proposed is to control one or more of the following factors: eccentricity ratio (defined in the next section), shaft radial preload, bearing clearances, lubrication oil viscosity, lubrication oil inlet pressure, shaft dimensions (length and diameter), bearing geometry and surface and shaft speed.

Though the given methods seem to have different approaches, many of the parameters affecting the instability are quite related. These control methods can be categorized into three general classes. Each of the three classes has factors that are

to be controlled to cure the instability. The proper method to select depends on the application and restrictions. The three classes are:

- Rotor related: Applying external forces (unbalance, preload, etc.).

- Bearing related: Changing the bearing design (tilting pad, pressure dam, etc.).

- Oil related: Changing the oil system (temperature, pressure, etc.).

All the solutions are primarily working to control λ in one way or another. In most cases, decreasing λ reduces the instability threshold.

Oil system factors cover the oil properties inside the bearing such as inlet pressure, temperature and viscosity. The oil viscosity is known to influence the oil velocity profile while the oil temperature changes the viscosity. Moreover, the oil load capacity is dependent on the oil viscosity. In a lubrication system design, the oil pressure and flow are considered parameters for the energy and heat balance.

Bearing factors cover the type of bearing design and the existing clearances between the shaft and bearing. There are many fluid film bearing designs which are suitable for certain applications. According to an old survey (1979) [29, 30], 90% of large turbo-machinery in petrochemical industry use pressure dam and tilting pad bearings (Figure 2-10).

Generally speaking, bearing designs that preload the shaft away from the bearing center through pressure distribution tend to enhance the stability (e.g. pressure dam bearing). A bearing design that reduces the oil circulation around the

shaft also enhances the stability (e.g. tilting pad bearing). It is known that eccentric configurations are found to be more stable than concentric configurations [2,21]. Proper bearing design or selection should consider the instability as well as the other problems. In some cases of bearing modifications (e.g. changing from plane to grooved), an increase in the bearing temperature could be encountered.

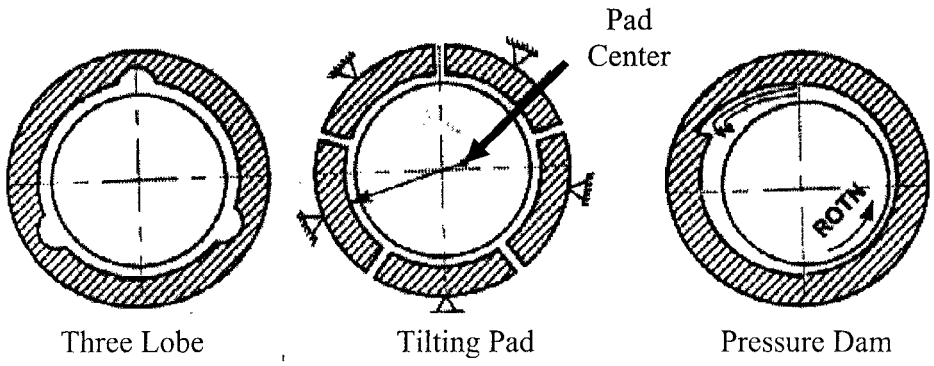

Figure 2-10 Examples of fluid film bearing designs

Despite the bearing design, the existing clearances play a major role in the whirl/whip instability. As a rule of thumb, the instability is more likely to occur as the clearances increase. Increasing the fluid film thickness in the bearing clearance circle reduces the entire system stiffness. Refer to [30-31] for more details.

The model in Figure 2-11 explains the effect of fluid film thickness. As the film thickness increases (longer spring to compress), the system becomes softer. As a result, the natural frequency is decreased. From a practical point of view, if a whirl/whip problem is to be solved through the bearing factors, adjusting the clearances will be the most affordable method for industrial applications.

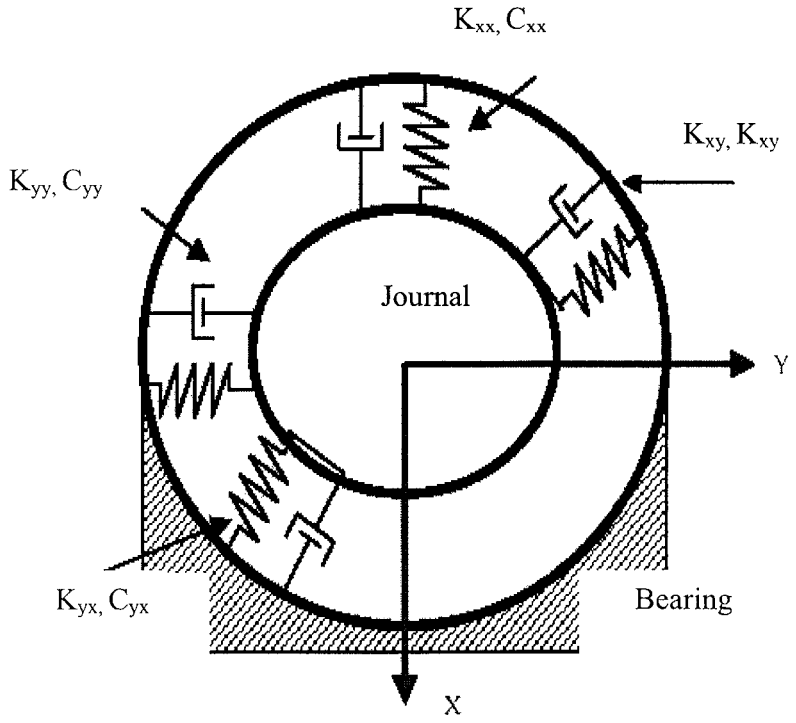

Figure 2-11 Modeling fluid film bearing as springs

The method of *Anti-Swirl* is based on the principle of injecting oil with proper pressures to control the shaft dynamics inside the bearing [19-20]. Other approaches consider redesigning of bearing parameters. Efforts have been put to overcome the instability problems and have resulted in different designs of radial journal bearings [22,23,25].

Another way to control the whirl/whip instabilities is through rotor factors which include four general approaches: mechanical properties (mass dimension/distribution and material) and rotor location in bearing (pre-load and unbalance). In those methods, shaft eccentricity is altered. Slight misalignment or unbalance may solve the problem, however, this should be done after calculations to anticipate the rotor response. The core of this research is related to these factors.

Any attempt to control the whirl and whip vibration should consider the following factors:

- The threshold of instability
- The amplitude of vibration.

2.8 Shaft Average Eccentricity Ratio

Eccentricity, *e*, is the distance between the bearing and journal centerline. It is zero when both centerlines coincide on each other and is maximum when the shaft surface touches the bearing's wall. Maximum eccentricity is the radial clearance, *C*, of the bearing. If the eccentricity exceeds this value, then it is either that the shaft rubs and penetrates the bearing white metal or the bearing clearance itself has increased. Mathematically,

$$0 \leq e \leq C \tag{2-9}$$

where

$$C = (D_B - D_S)/2 \tag{2-10}$$

and

$$e = \sqrt{(x^2 + y^2)} \tag{2-11}$$

where D_B and D_S are the diameters of the bearing and shaft, respectively. The last equation is an expression of eccentricity, where the bearing center is the origin (0,0) and the coordinates of the shaft center are (x,y) as illustrated in Figure 2-12.

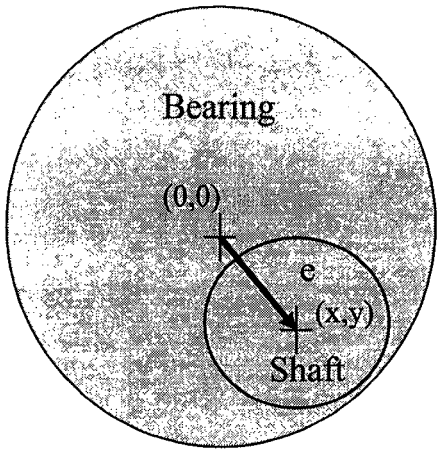

Figure 2-12 Exaggerated shaft eccentricity

Due to the dynamic motion and reaction forces of the rotor-bearing system, the eccentricity changes dynamically with time. Shaft average eccentricity (*SAE*) is developed as a representation of the eccentricity under certain dynamic conditions within a short period of time, Δt, say Δt= 10/shaft speed (in rpm). Notice that this is an artificial location of the shaft. The shaft average eccentricity is associated with the standard plot of shaft average centerline (Figure 2-13). The later plot is basically, y-*SAE* vs x-*SAE* where the y and x refer to the vertical and horizontal directions.

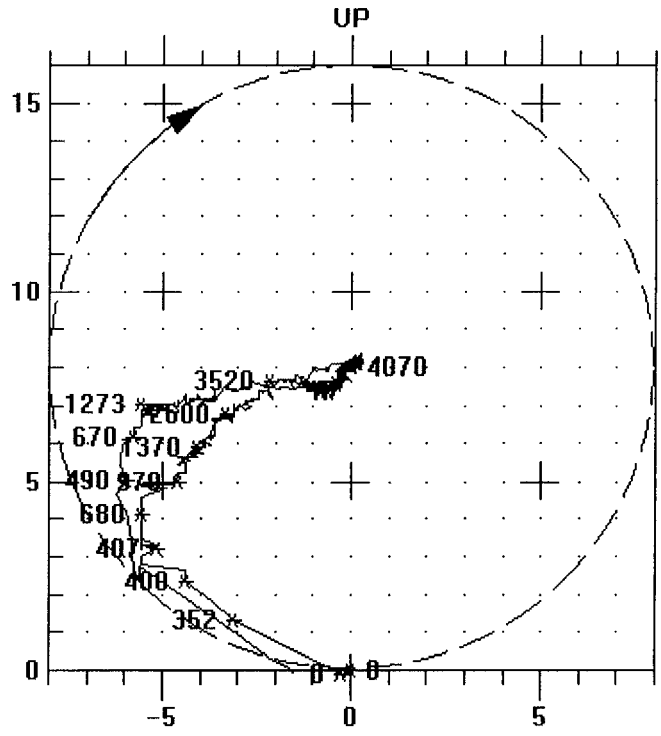

Figure 2-13 Shaft average centerline plot

Shaft average eccentricity ratio, ε, is the ratio of the shaft average eccentricity to the bearing radial clearance. The advantage of this representation is normalizing (independent of the bearing radius). In other words, an un-normalized shaft average eccentricity of 100 micron could be high and could be normal depending on the bearing clearance (of large and small clearances) unlike a value of 0.8 for ε. Mathematically,

$$\varepsilon = e/C \tag{2-12}$$

and

$$0 \leq \varepsilon \leq 1 \tag{2-13}$$

ε is a major contributor in controlling λ. The effect of journal location in the fluid film bearing is summarized in Table 2-2. The variables are compared with both speed and bearing load being constant.

Table 2-2 Conceptual summary of consequences as shaft eccentricity ratio increases

Parameter	Small Eccentricity	Large Eccentricity
Shaft in bearing		
Force on fluid film		
Velocity profile		
Bearing load, W	Same	Same
Shaft speed, Ω	Same	Same
Journal eccentricity ratio, ε	Small	Large
Minimum film thickness, h_{min}	Large	Small
Flow rate across h_{min}	Large	Small
Average circumferential velocity ratio λ	Large	Small
Bearing stiffness, K	Small	Large
Bearing damping, D	Small	Large
Instability vibration amplitude	Large	Small
Stability threshold speed, Ω_{st}	Low	High

CHAPTER 3

EXPERIMENTAL WORK

3.1 Introduction

In this chapter, the major components of the thesis experimental work conducted on the vibration instability are discussed. First, the experimental set up is briefly described. The setup includes mechanical components, instrumentation and software. Then, the test configurations are introduced and followed by the obtained results. The main configurations studied are: disk axial location, shaft length and disk unbalance. Pre-tests were conducted to verify the output signals. Impact tests were performed using modal hammer and the results for both the rotor and its foundation are presented. Row data was exported to spread sheets for further analysis as discussed at the end of the chapter.

3.2 Experimental Setup

3.2.1 Mechanical Components

The RK4 rotor kit [32] furnished with the vibration instrumentation was used. The setup included the following mechanical components: a shaft, sleeve bearing, fluid film bearing, disk with balancing holes and a provision for relocation, lubrication system and controllable speed DC motor which can be seen in Figures 3-1 to 3-5. The sleeve bearing (bushing) can be relocated axially to modify the shaft length (l) which is adjustable up to about 400 mm. The disk location (l') is also adjustable anywhere between the two bearings. The parameters l' and l are shown in Figure 3-2. As seen in this figure, the axial location is referenced from the fluid film bearing to the disk or to the sleeve bearing. The shaft diameter is 10 mm, disk thickness, diameter and weight are given as 25 mm, 75 mm and 800 g, respectively.

The diametrical clearance of the fluid film bearing is 0.4318 mm (17 thou) and its width is 25.4 mm (1 in). Journal diameter is also 25.4 mm (1 in).

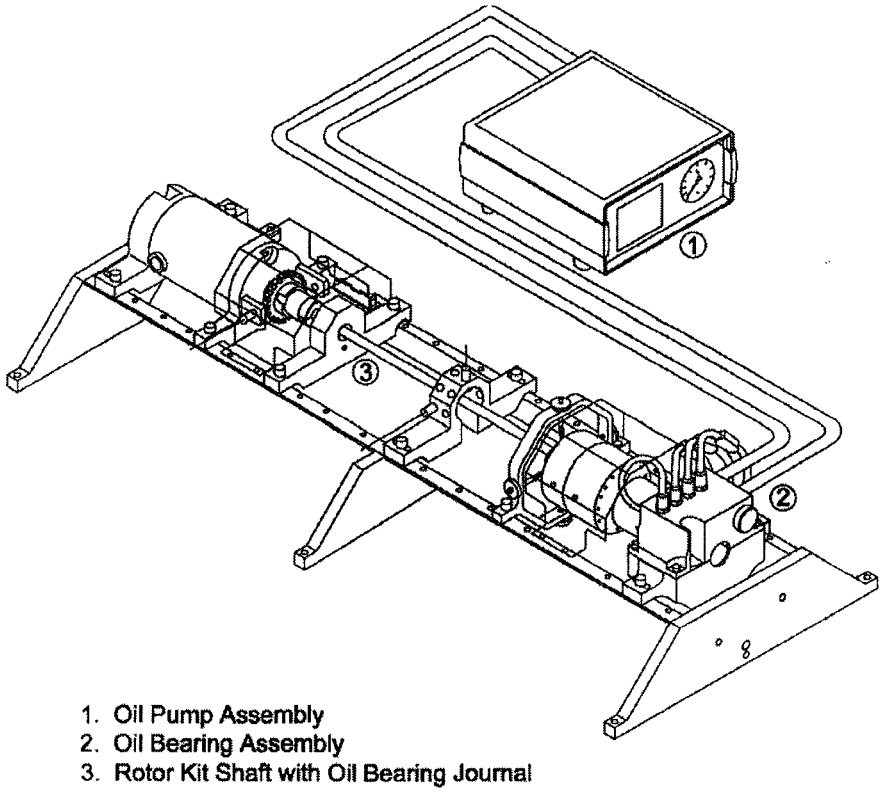

Figure 3-1 Schematic drawing for the rotor kit [32]

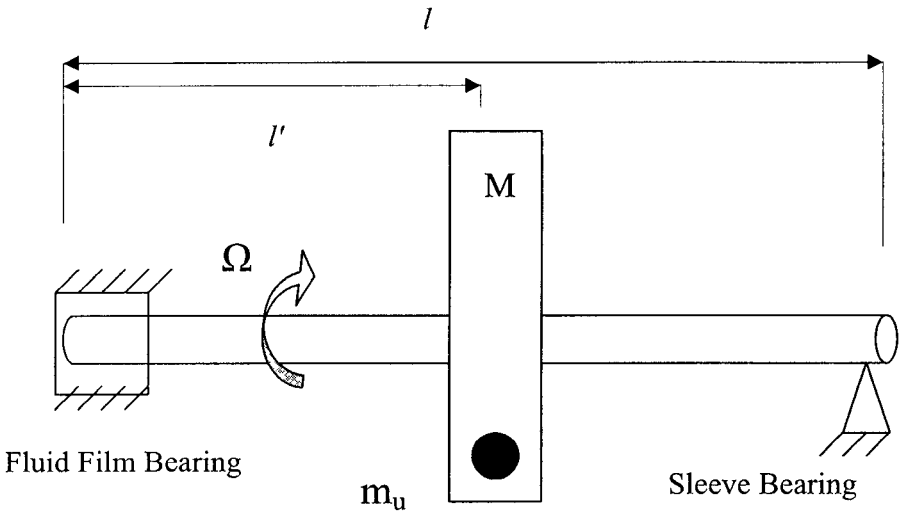

Figure 3-2 Definition of the parameters l and l'

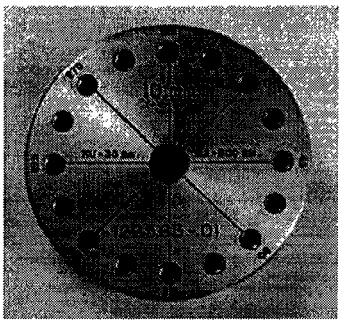

Figure 3-3 Disk with the holes for adding unbalance weight

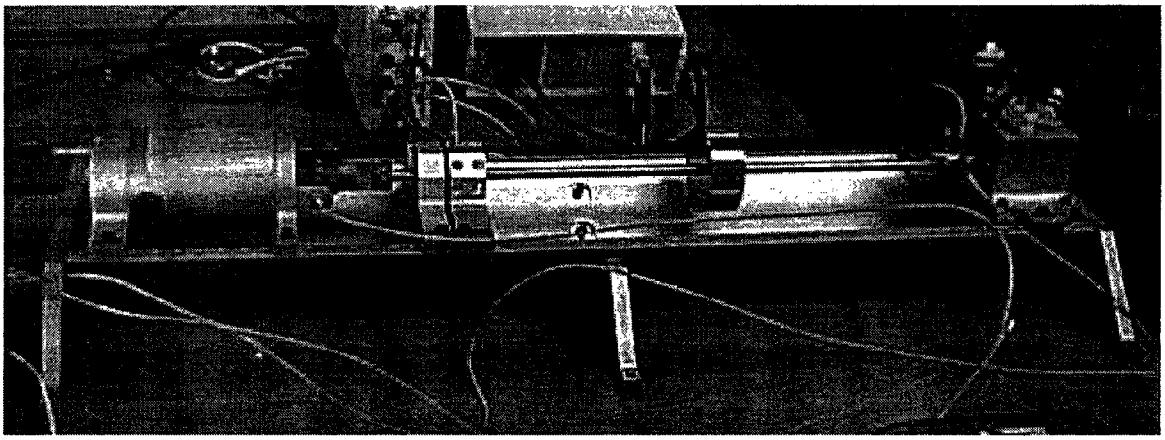

Figure 3-4 RK4 rotor kit assembly

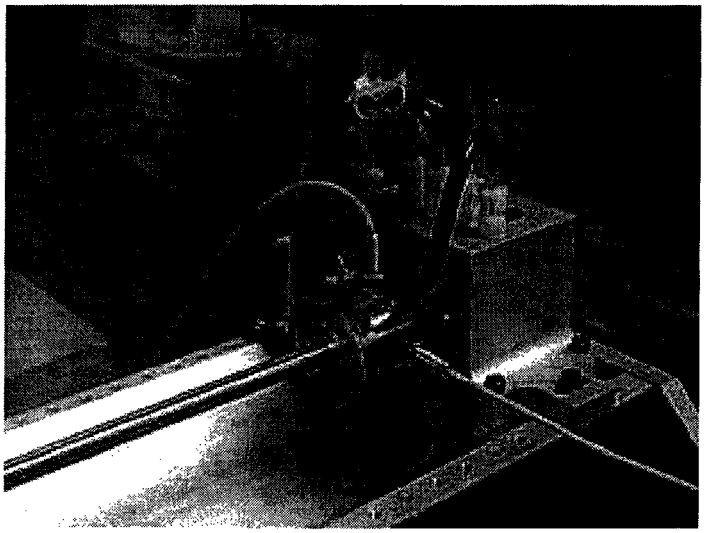

Figure 3-5 Fluid film bearing with the horizontal and vertical probes

3.2.2 Instrumentation

Instruments were used to collect the raw mechanical vibration signals. They perform some basic mathematical operations such as calculating the direct vibration readings. Then they send the data to the computer for further processing, analysis and storage. The following description is for major instrumentation components employed during the tests:

- *Eddy current (proximity) vibration probes*: to measure the radial relative shaft vibration with respect to bearing housing. Four probes were used, two on each bearing. They were mounted in the true horizontal and vertical directions.

- *Key phasor and speed pick up*: to give a signal per revolution (phase reference) and to measure rotor speed. Key phasor minimum reading is 100 rpm.

- *Proximitors (oscillator demodulator):* to convert the electrical signal to the desired engineering unit, in this case from mV to mils. Five proximitors were used, one for each probe.

- *Data acquisition interface unit (DAIU):* to capture data patches and digitize them. It also calculates the following: overall vibration level, 1X phase and amplitude and gap voltage. This data is instantaneously transferred to the computer through a special communication protocol.

- *Speed control unit:* to adjust both rotor speed and ramping rate online, through a closed feedback loop.

Figure 3-6 is a block diagram for the path of the vibration signal from the shaft until it is analyzed in the computer software. The fluid film bearing is abbreviated in this figure as FF and sleeve bearing as SB. ADRE is a software whose name is abbreviated from Automated Diagnostics for Rotating Equipment, used in the vibration analysis (from Bently Nevada).

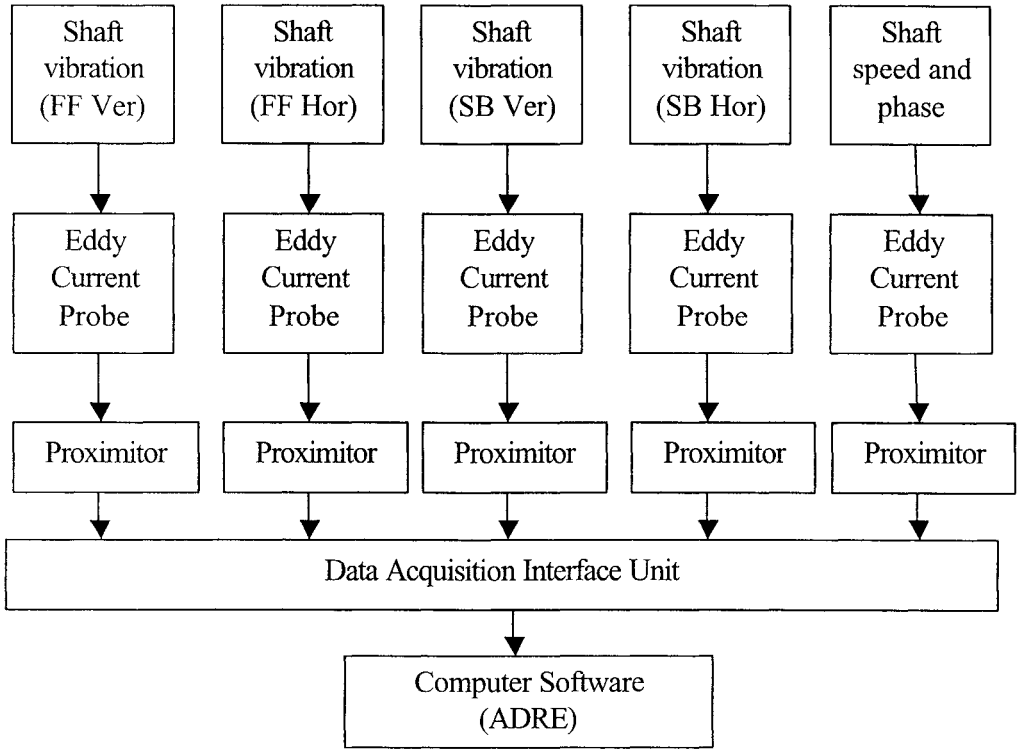

Figure 3-6 Vibration signal path through the instruments

3.2.3 Software

A computer was used to store and analyze the data through ADRE [33]. ADRE is programmed to communicate with the DAIU and to adjust the DAIU's configurations to match with the physical rotor setup. ADRE produces several plots that are used in the vibration diagnosis and analysis. The most important plots related to this research are:

1. *Time waveforms.*

2. *Half spectrum* and *full spectrum*: FFT of the waveform for single and dual probe configurations.

3. *Bode plot*: transient direct and filtered vibration of 1X amplitude versus rotor speed and filtered 1X vibration phase versus rotor speed.

4. *Cascade plot*: 3-D transient superimposed spectra over each other as rpm increases/decreases, where x-axis is frequency, y-axis is filtered amplitude and z-axis is speed.

5. *Orbit plot*: Two-dimensional dynamic plot of x and y-vibration readings.

6. *SACL*: shaft average centerline location in the bearing clearance circle, traced as speed varies.

3.3 Experimental Tests

The experiments were conducted in order to trace the instability response of the system as a result of changing the following parameters:

1. Disk axial location
2. Shaft length
3. Disk mass unbalance

All the experiments ran up to a speed of 9000 rpm. The ramp rates applied were 5000- 8000 rpm/min.

3.3.1 Pre-Tests

Pre-test checks were performed to verify the correctness of vibration signal acquisition and processing, including the gap voltage calibration. In addition, the four signals were compared with each other and were found in agreement. Final confirmation used the CSI 2115 and *RBM Consultant* (portable stand-alone FFT vibration analyzers from Computational Systems, Inc.) to counter check the instrumentation system as a whole from the probe up to the output of ADRE software on the computer. Both CSI and Bently Nevada instruments matched each other and no noise in the signal was noticed.

A comparison of vibration signals from the vertical and horizontal probes shows a 87 deg phase shift between the two responses due to 1X excitation (unbalance). Refer to Figure 3-7 for more details.

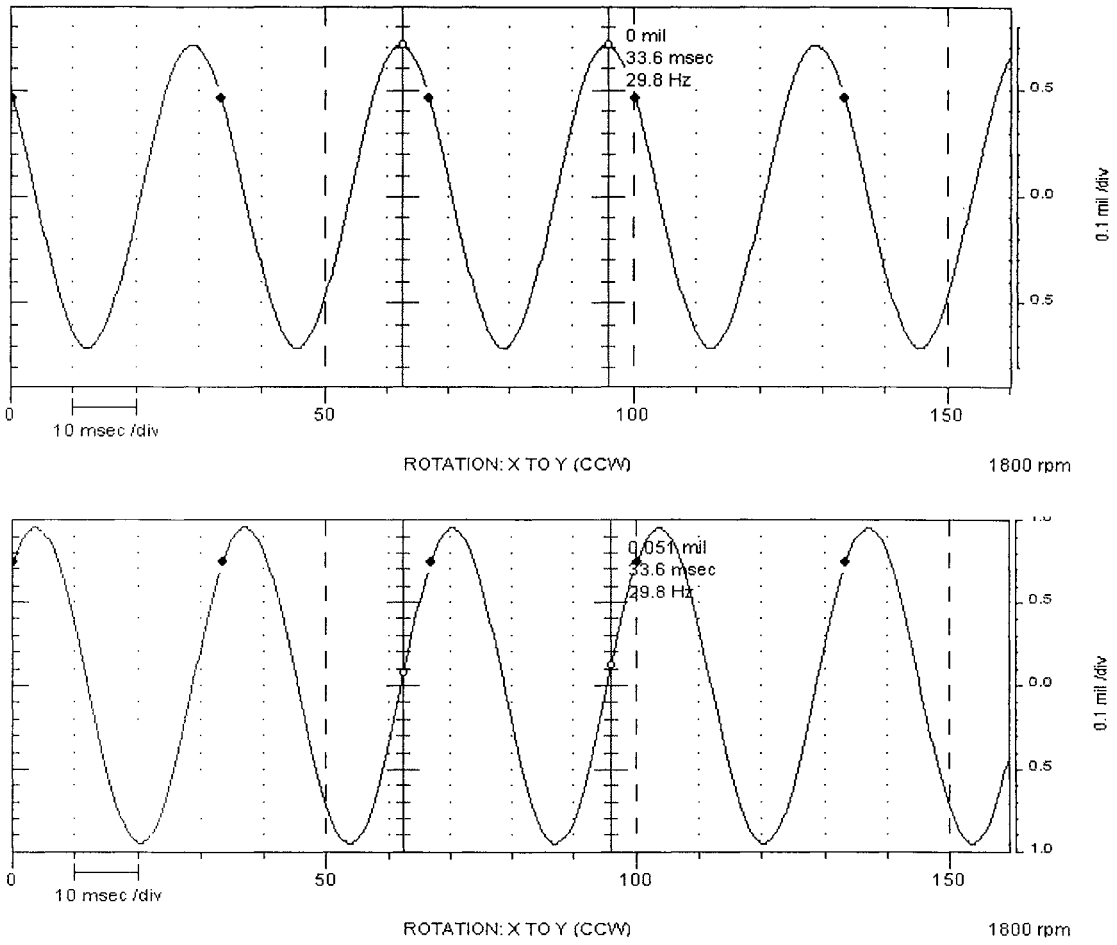

Figure 3-7 Vertical (up) and horizontal (down) probe unbalance vibration signals

3.3.2 General Observations

After conducting the pretests, several common observations were noticed in most setups, which can be good starting points to the experimental results. First, the instantaneous plots (whose maximum data acquisition time covers eight shaft revolutions or less) are discussed and then the transient plots are considered.

Figures 3-8 to 3-13 show a comparison of the vibration response before and after the instability starts at 2320 and 2550 respectively, collected from the same probes under the same conditions. Notice the waveform in Figure 3-8 before the instability, where the dominant vibration cycle is the 1X rpm. Figure 3-9 shows the waveform of the vibration signal after the instability develops. In the spectra of Figures 3-10 and 11, notice the minor amplitude of 1X compared to the major instability amplitude at about 0.5X.

The circular forward precession can be seen from the orbit plots, since both the directions of the vibration signal and the shaft rotation are the same (Figures 3-12 and 3-13). After the occurrence of the instability, the orbit shape magnifies accommodating the sub-harmonic frequency as can be seen from the spectrum plot of Figure 3-11.

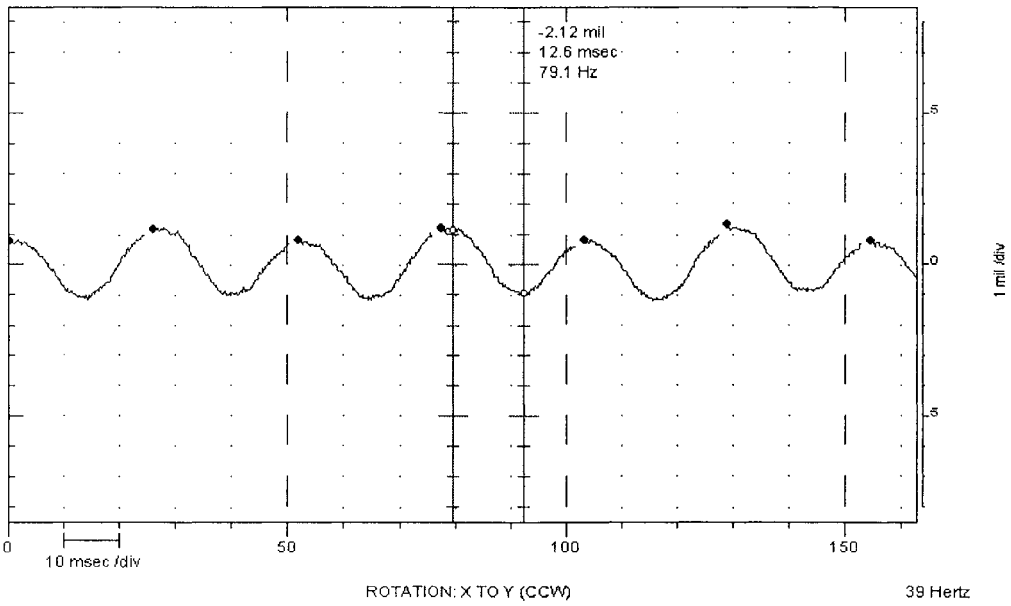

Figure 3-8 Waveform before the instability

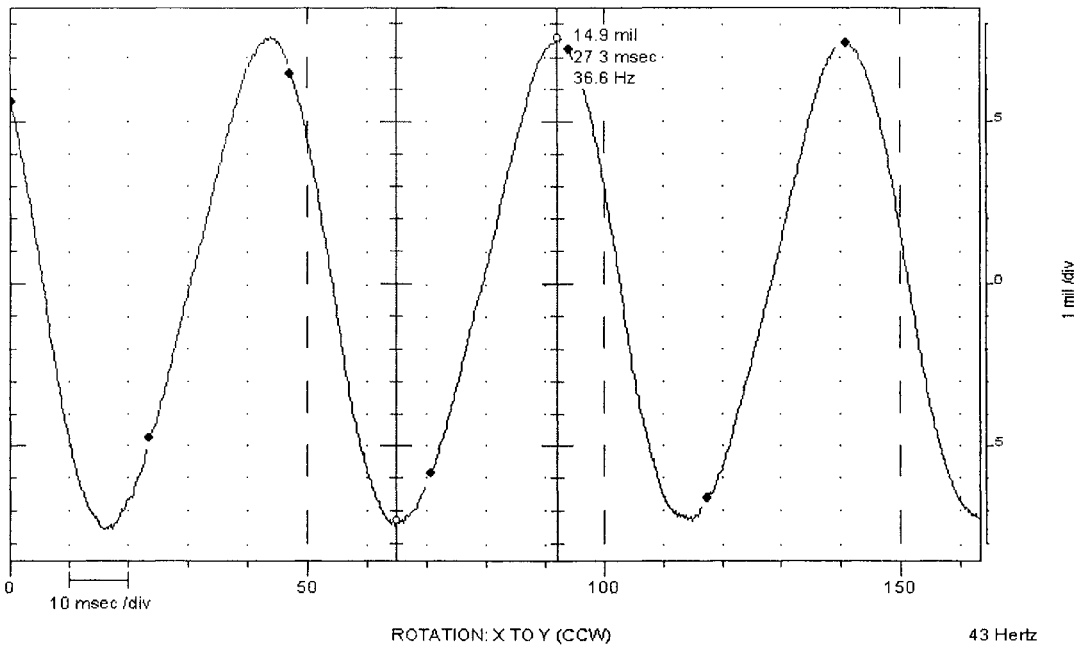

Figure 3-9 Waveform after the instability

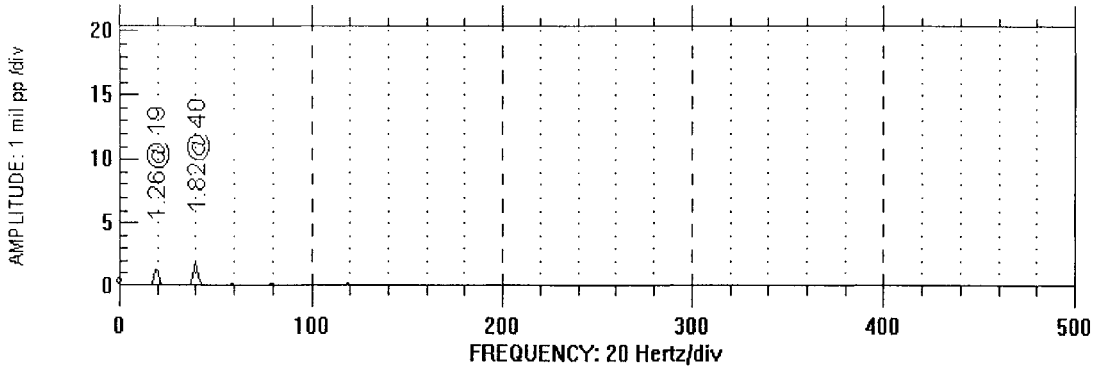

Figure 3-10 Spectrum before the instability

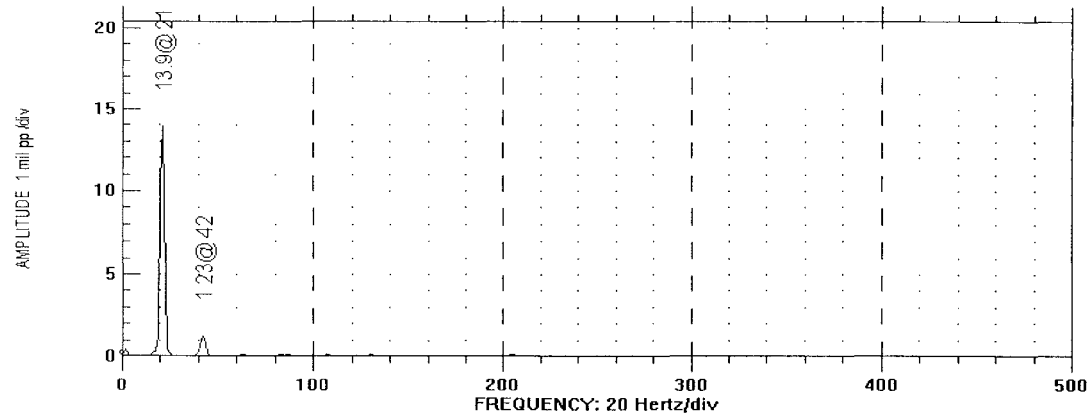

Figure 3-11 Spectrum after the instability

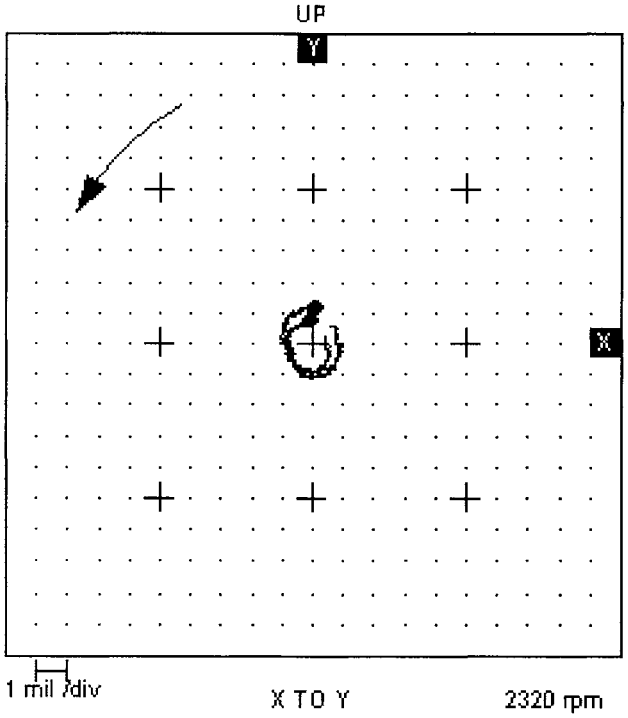

Figure 3-12 Orbit before the instability

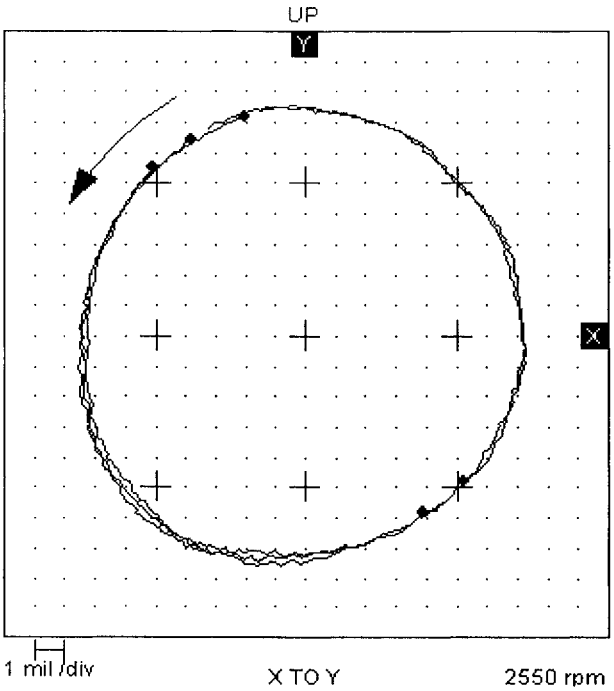

Figure 3-13 Orbit after the instability

The Bode plot of the fluid film bearing shown in Figure 3-14 demonstrates a typical relation between the overall vibration level and the unbalance during instability. Notice the sudden fluctuation in 1X phase just after the system gets into instability. Also, though the amplitude of 1X may increase/decrease, the overall vibration level is maintains its value steadily. This is because the vibration amplitude is covering almost all possible space for motion, i.e. the bearing clearance, and there is no room for the amplitude increase. This scenario is seen in most cases, yet other cases were highlighted in the unbalance section. In this particular test, the instability is active in the range of 2400 rpm up to the maximum speed of 10000 rpm.

On the other hand, the Bode plot of the sleeve bearing is qualitatively different (Figure 3-15). Both the 1X and overall vibration levels increase as the speed increases. Also, the change in the 1X phase is gradual and smooth unlike the sudden change in the fluid film bearing case.

The plot of the shaft average center line given in Figure 3-16 illustrates the eccentricity of the journal in the fluid film bearing. It is noticed that the shaft, with the speed increase, moves towards the center of the bearing, decreasing the eccentricity. In fact, most cases had the instability occurring in a circle of about 3 mils from the center of the bearing.

The difference between the vibration behavior in the sleeve bearing and fluid film bearing is related to the shaft movement (position). For comparison, the vertical shaft center movements (gap voltage) for both bearings are given as a function of speed in Figure 3-17. Notice the continuous and gradual increase in the sleeve bearing compared to the asymptotic increase in the fluid film bearing. The asymptotic line is clearly seen by the instability threshold at about 2500 rpm.

Cascade plots are used to show the sequence of changes in filtered vibration amplitudes when the instability starts. The cascade plot given in Figure 3-18 records a

threshold of instability at 2550 rpm when the subharmonic amplitude suddenly rises. The overall vibration level will also jump and this was seen in the Bode plot in Figure 3-14. However, Bode plot does not provide amplitude information of the instability frequency, as in this case. In the cascade, notice the oil whirl behavior at constant relative vibration order at about 0.47X rpm and then the oil whip behavior with a constant vibration frequency at about 3850 cpm.

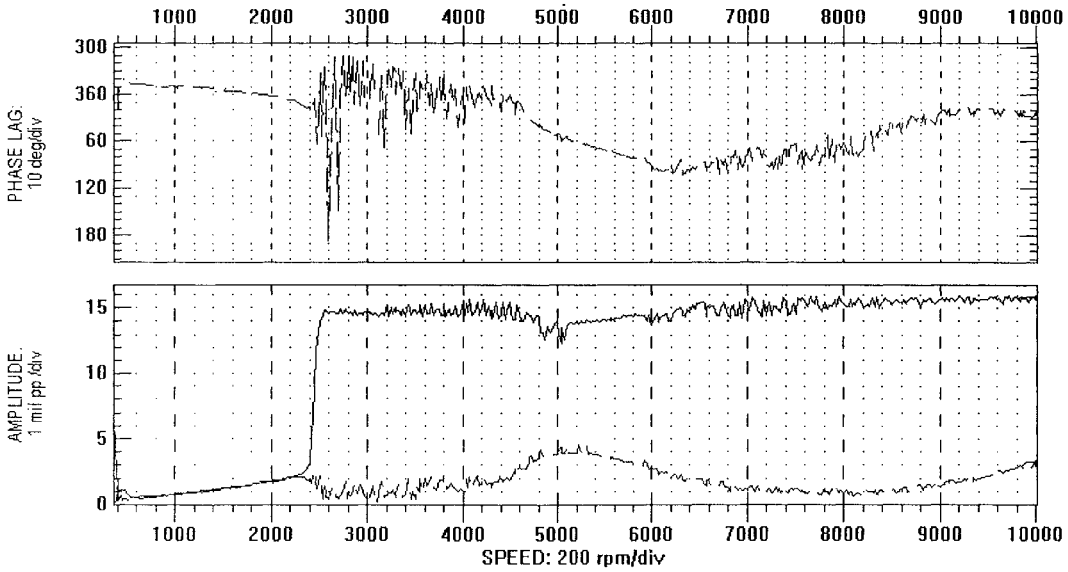

Figure 3-14 FF bearing Bode plot

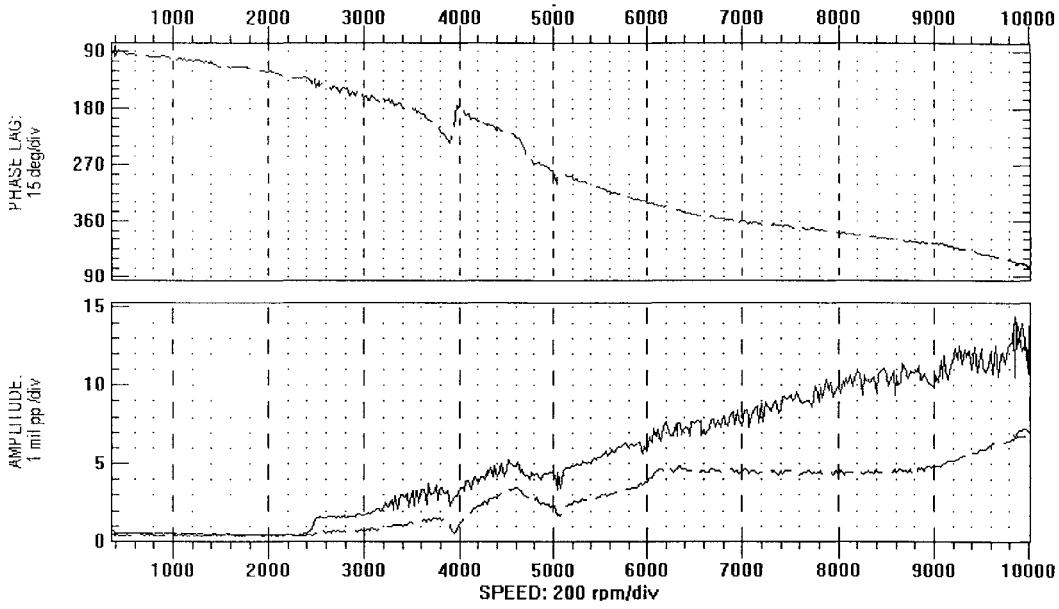

Figure 3-15 Sleeve bearing Bode plot

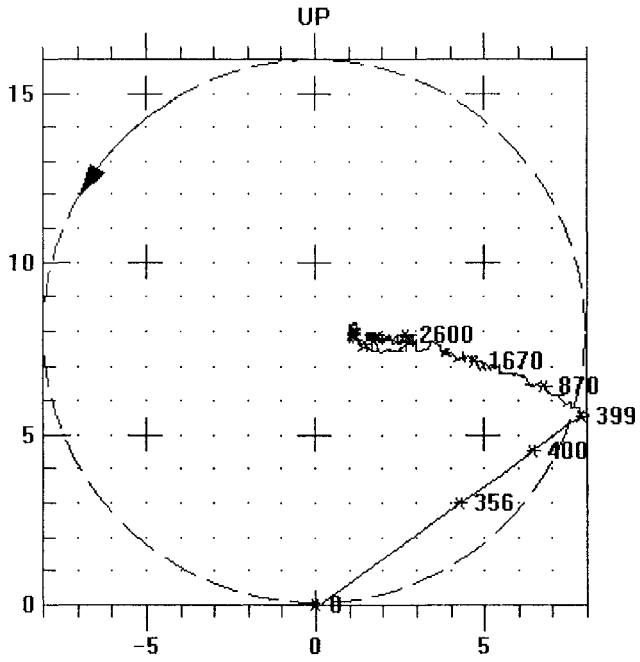

Figure 3-16 Trend of shaft average center line

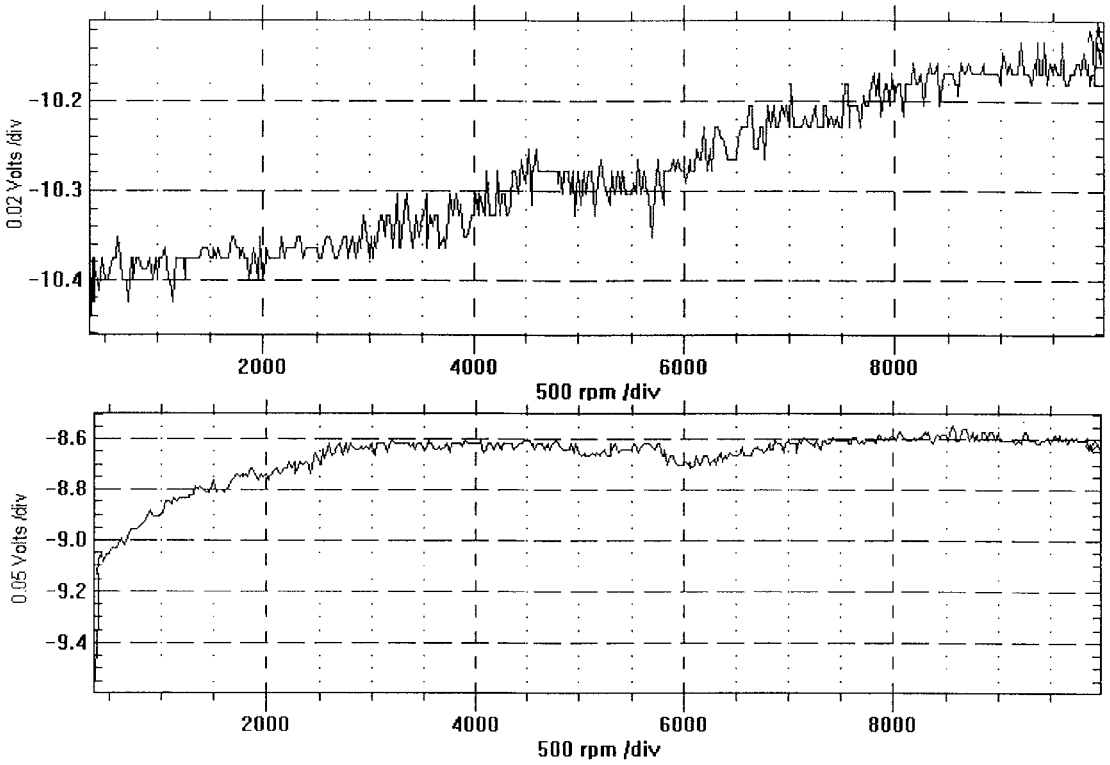

Figure 3-17 Gap voltage trends, SB (top) and FF bearing (bottom)

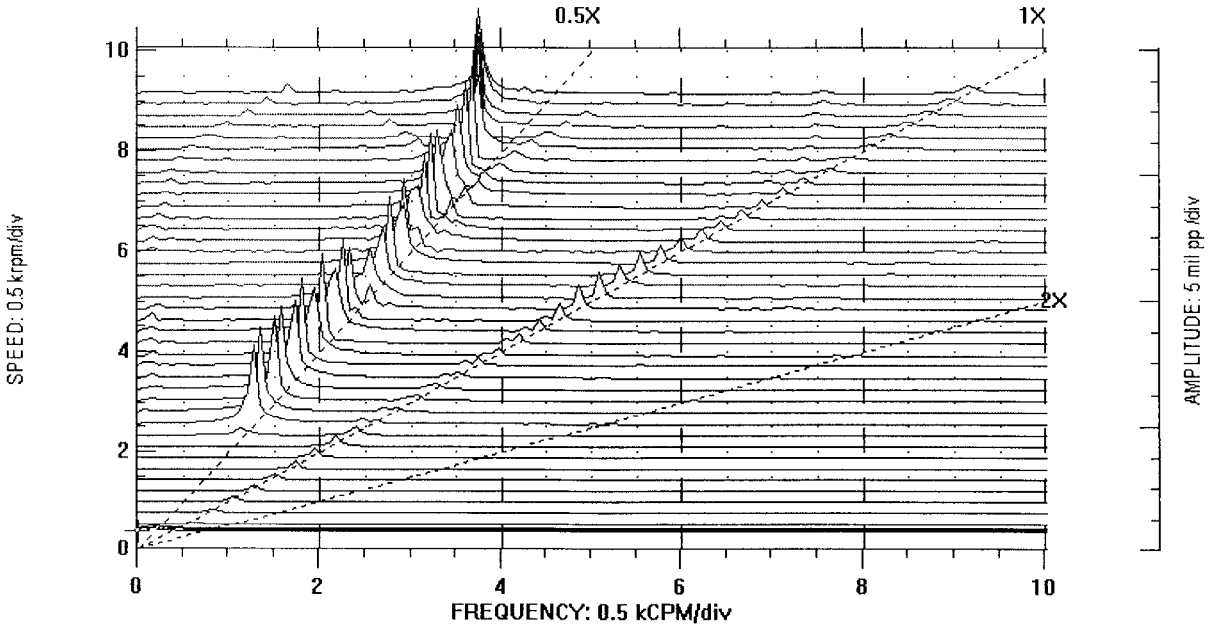

Figure 3-18 Cascade plot

Figure 3-19 shows the consistency of the results collected from the two probes on the fluid film bearing. Results are taken from eight experiments. The threshold of instability is given in terms of the shaft speed (rpm). It can be noticed that there is a good matching between the results collected from both horizontal and vertical probes.

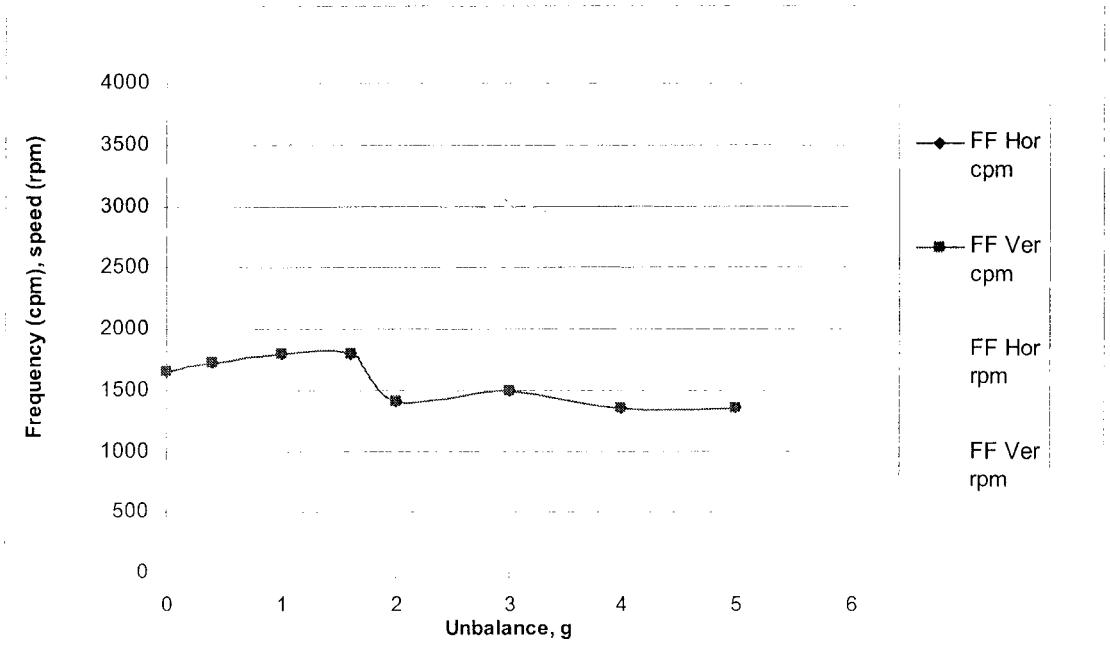

Figure 3-19 Instability frequency and threshold collected from four probes

In the following section, the rotor set up was fixed except for the parameter which was altered to examine its effect on the instability. Results were gathered to generate trends. More attention was oriented to the threshold of instability.

3.3.3 Disk Location

The plots given in Figures 3-20 and 3-21 were generated from four runs under the following conditions: rotation is counter clockwise, shaft length is l=300 mm and no unbalance mass is added. With the increase of disk location, the instability threshold frequency is increasing while its order (ratio of the vibration frequency to the shaft speed frequency) is decreasing. No effect was noticed on the instability amplitude by this factor

and the effect on the instability frequency is minor except for the high speed when the instability becomes a whip. This is illustrated in Figure 3-21.

Figure 3-22 shows the plots for the effect of disk location on the instability threshold for different shaft lengths. Again, the frequency of instability threshold is increasing with the increase in disk location.

The effect of the axial disk distance between the disk and the fluid film bearing (l') is clear on the threshold of instability. It was found that the parameter (l') is the strongest factor in affecting the threshold of instability and in the qualitative change of rotor response.

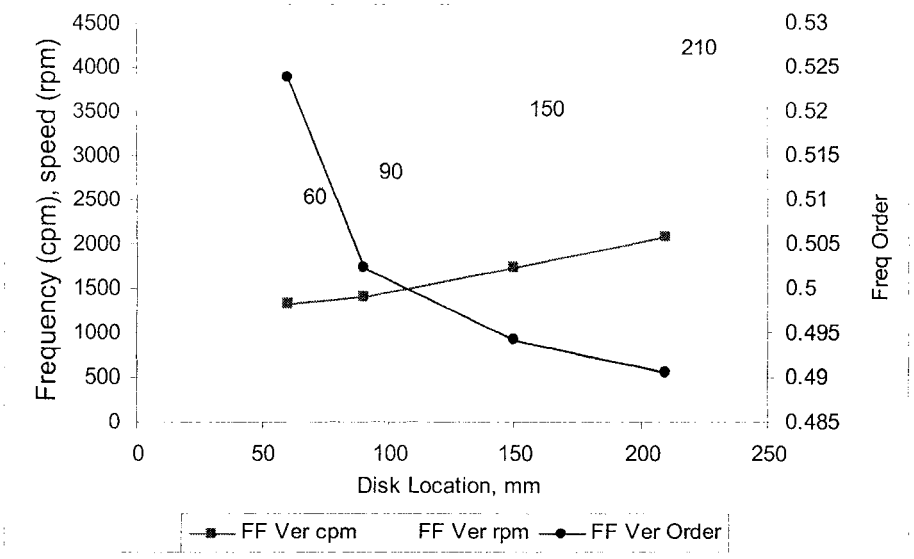

Figure 3-20 Instability threshold, frequency and its order.

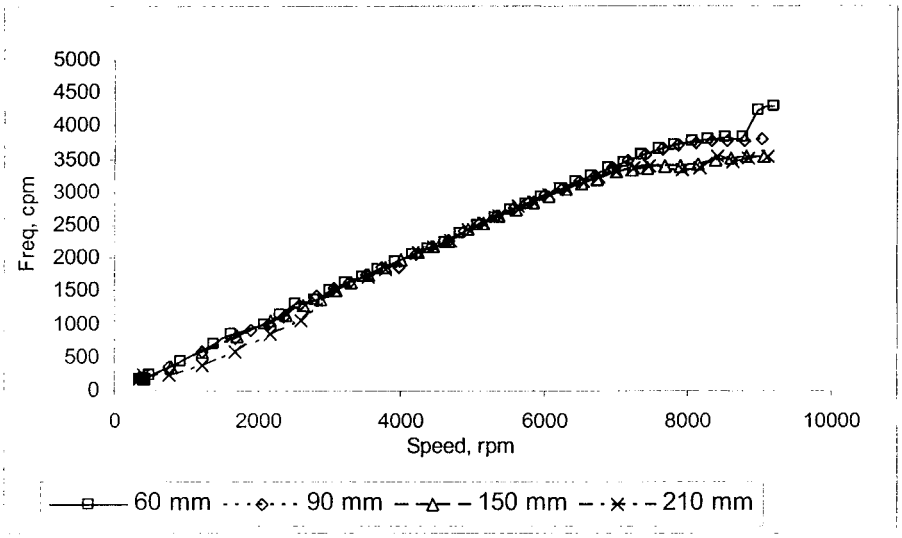

Figure 3-21 Effect of disk location on Instability frequency

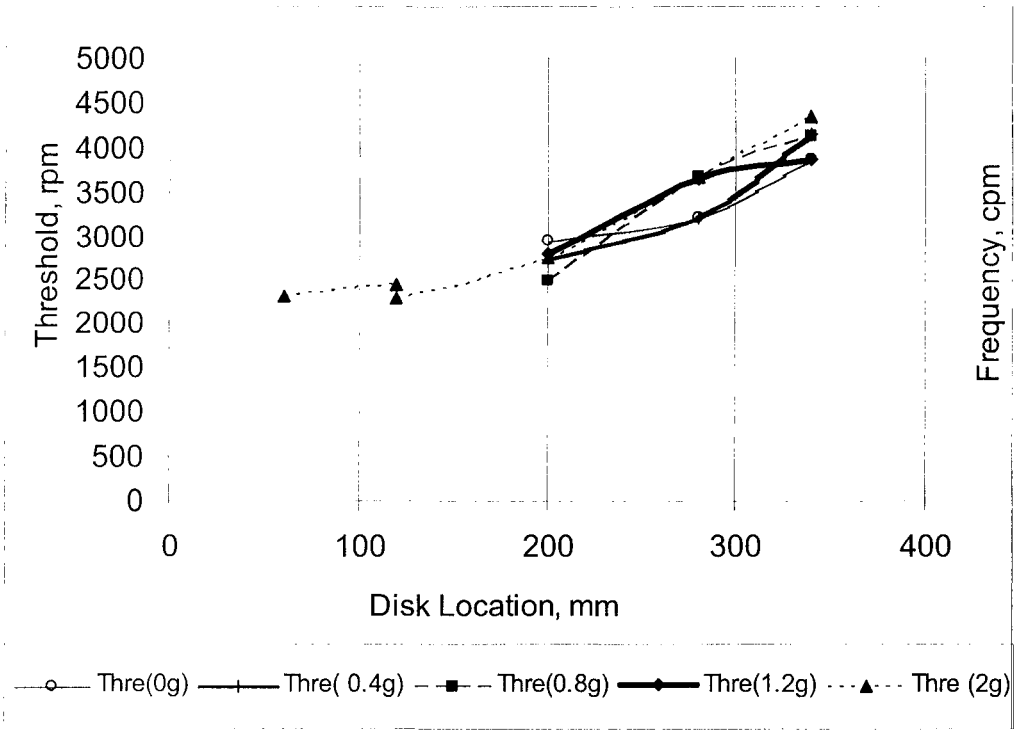

Figure 3-22 Effect of disk location on instability threshold with different shaft lengths

3.3.4 Shaft Length

The span between the fluid film bearing and the sleeve bearing (l) was examined as a factor affecting the instability threshold. Tests revealed a decreasing trend. It was clear from the experimental result that the smaller the shaft length, the higher the frequency of instability threshold. This is possibly due to the fact that a shorter shaft length yields a higher eccentricity, which consequently results in a higher instability threshold. This parameter has no affect noticed on the instability amplitude.

Figure 3-23 is a sample result taken from tests for shaft lengths l= 200, 300 and 400 mm. In order to exclude the effect of disk location the disk was kept in the mid-span in all cases.

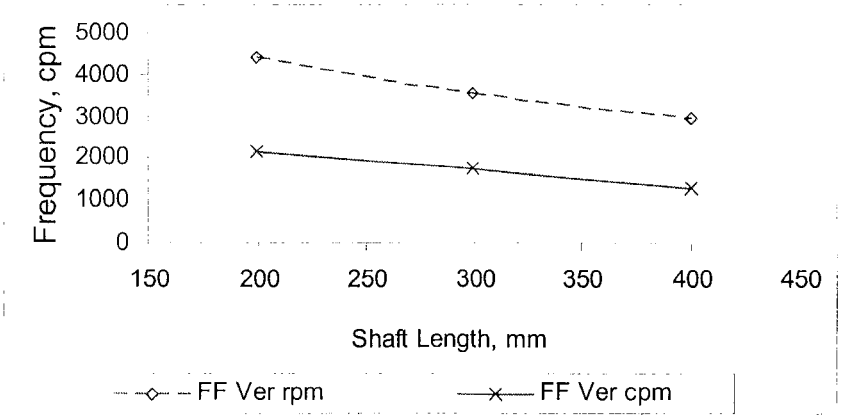

Figure 3-23 Effect of shaft length on the threshold of instability

3.3.5 Mass Unbalance

The effect of unbalance on the fluid induced instability behavior was studied for a single disk. The setup was adjusted to have the best alignment so that the bearing can generate the oil instability. The experiments started with the response of the system with no unbalance. The amount of unbalance was increased gradually in a series of tests. The example sample cascade plot, given in Figure 3-18, shows the minor change in the 1X

amplitude compared with the major change in the instability frequency at about 0.5X. Figure 3-24 is a result of the exported data trend of instability amplitude. Notice the decrease- increase amplitude between samples 20-30 due to unbalance resonance. It is even clearer when the unbalance increases as shown in Figure 3-25.

No general rule can be drawn for the unbalance, but it increases the threshold of instability most of the cases especially with the higher values of *l'*. Otherwise it decreases the threshold. The results can be summarized as follows:

- Increasing the weight results in rising the threshold of instability if the ratio *l'/l* is large.

- Increasing the weight results in lowering the threshold of instability if the ratio *l'/l* is small.

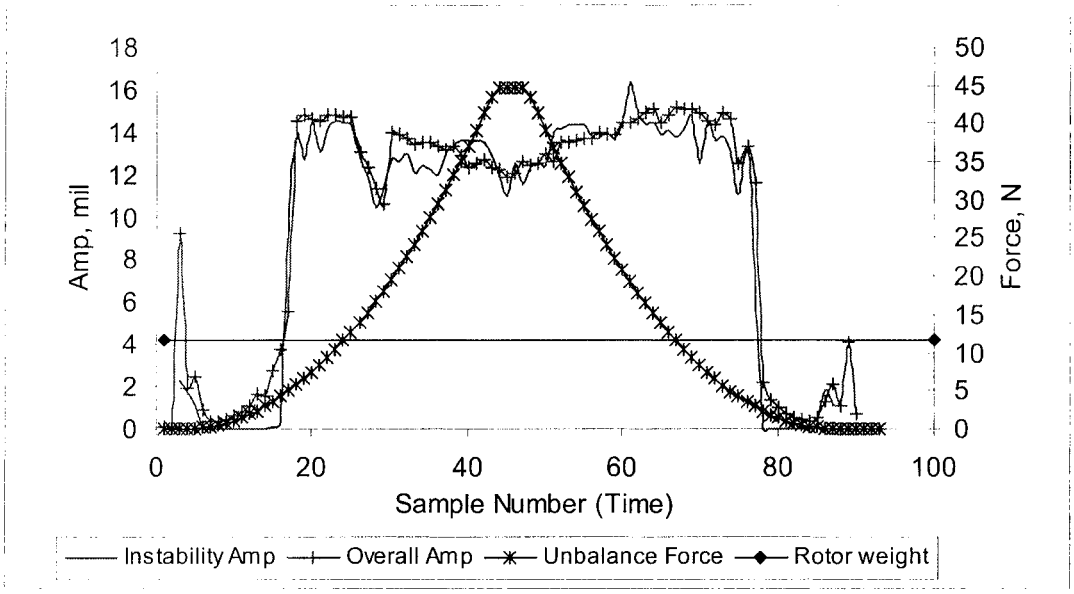

Figure 3-24 Unbalance and weight comparison in a transient response

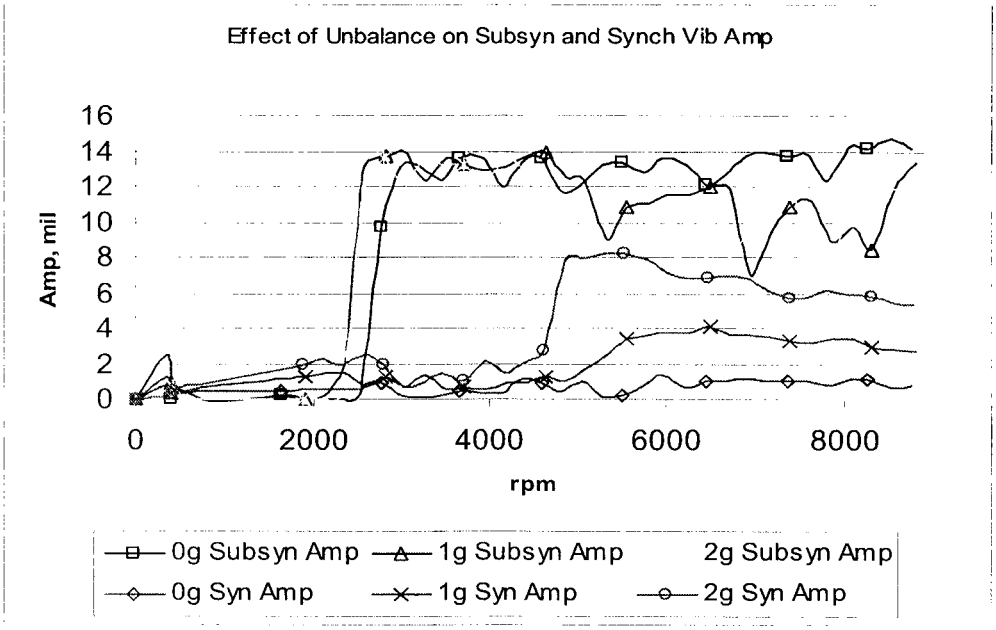

Figure 3-25 Summary of unbalance test results

Unbalance Evaluation:

To evaluate the amount of unbalance, ISO 1940-1 guidelines [28] were used. For the configuration of l'= 200 mm and l= 400 mm, the following calculations were carried out:

Machine: Rotor Kit (single stage turbine model, essential category machine)

Service Speed: 6000 rpm

Balance Grade Code: G 6.2

Maximum Permissible Specific Unbalance = 10.03 g*mm/kg

Rotor Mass= 1.047 kg

Maximum Permissible Total Unbalance = 10.5 g*mm

Unbalance Radius= 30 mm

Then, the maximum permissible total unbalance mass per G6.3 is found as 0.35 grams.

Table 3-1 is summary is for the unbalance calculations based on two *maximum service speeds* of 1800 and 6000 rpm, though the experiments were conducted up to speeds above 9500 rpm. The unbalance radius was taken as 32 mm.

Table 3-1 Permissible unbalance summary results based on ISO code for a speed of 6000 rpm

l' (mm)	l (mm)	**Permissible unbalance mass per G1, 2.5, 6.3 (g-mm)**	**Corresponding unbalance mass (g)**	**Tested balancing mass, m_u (g)**
100	200	1.47, 3.67, 9.26	0.046, 0.11, 0.29	0, 0.8, 2
60, 90, 210	300	1.57, 3.92, 9.87	0.049, 0.123, 0.31	0,1,2
200, 280, 340, 60, 120	400	1.67, 4.18, 10.53	0.052, 0.13, 0.35	0, 0.2, 0.4, 0.8, 1.2, 2, 3,4

Table 3-2 Permissible unbalance summary results based on ISO code for a speed of 1800 rpm

l' (mm)	l (mm)	**Permissible unbalance mass per G1, 2.5, 6.3 (g-mm)**	**Corresponding unbalance mass , (g)**	**Tested balancing mass, m_u (g)**
100	200	4.9, 12.24, 30.85	0.153, 0.383, 0.964	0, 0.8, 2
60, 90, 210	300	5.23, 13.07, 32.93	0.163, 0.408, 1.03	0,1,2
200, 280, 340, 60, 120	400	5.57, 13.93, 35.1	0.174, 0.435, 1.1	0, 0.2, 0.4, 0.8, 1.2, 2, 3,4

Comparing the table calculation and the masses used in the experiments reveals that the used unbalance amounts were close to the recommended amounts provided as limits in the standard.

The synchronous vibration increases at the critical speed and suppresses the fluid induced instabilities in the same region. Introducing the unbalance changes the journal position inside the bearing clearance circle and hence it influences the average circumferential velocity ratio which modifies the dynamic response of the rotor. The trends in Figure 3-26 illustrates that the shaft goes further down with the mass unbalance.

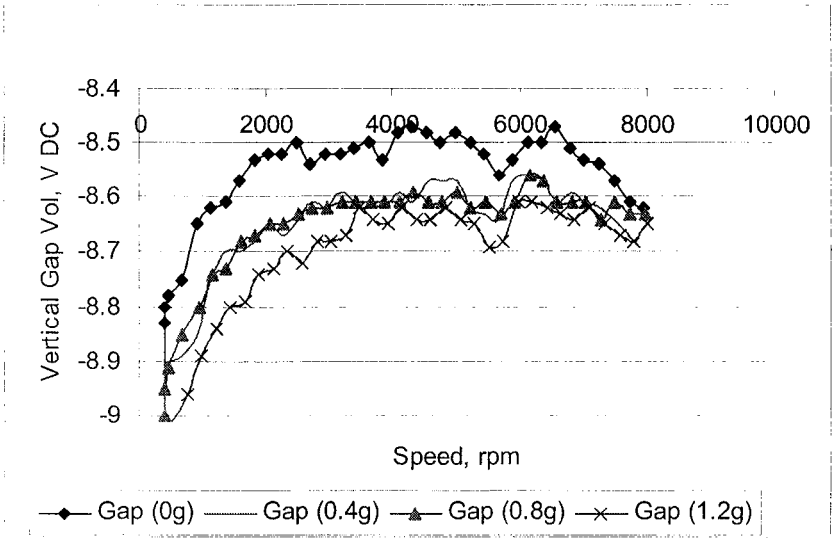

Figure 3-26 Effect of unbalance on the vertical journal position, given in gap voltage

Figure 3-27 shows the results extracted from eight experiments conducted under the following conditions: l'= 60 mm, l= 400 mm, pump discharge pressure= 1.5 psi, rotor ramp rate= 5000 rpm/min, unbalance mass increasing from 0 g to 5 g. It can be seen that the threshold of instability initially increases then decreases.

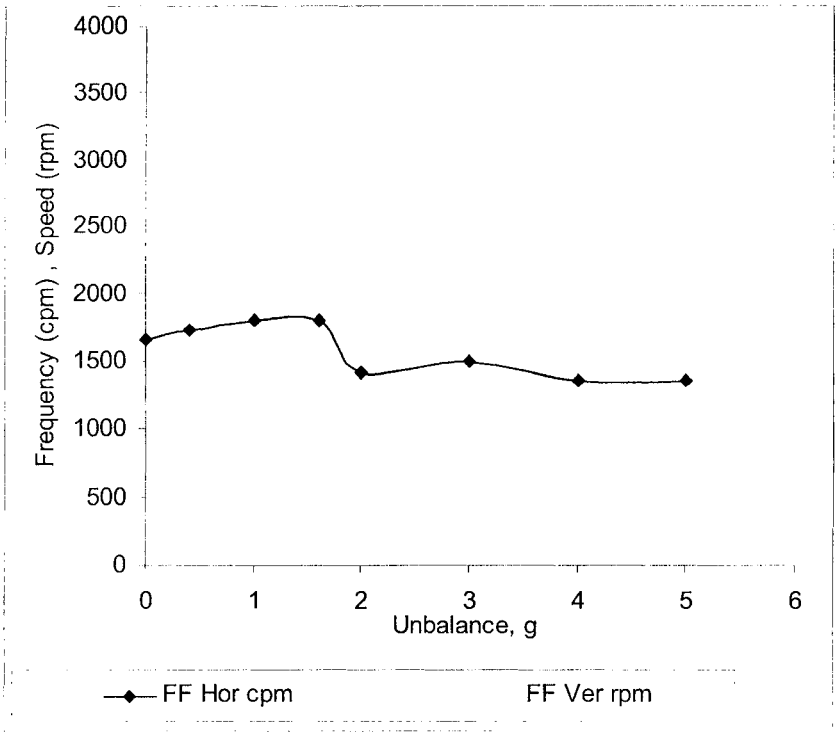

Figure 3-27 Effect of unbalance on the threshold of instability l'=60mm, l=400mm

3.3.6 Impact Tests

A series of impact tests were conducted on the rotor kit under different configurations and on the rig foundation. The following paragraphs will discuss the setting and results.

Hardware set up includes: two vibration analyzers CSI 2115 (Figure 3-28) and 2120A, medium sized modal instrumented hammer (Figure 3-29), general purpose accelerometer with magnetic base (CSI GP 610) and Bently Nevada multi-channel DAIU. Impact test results revealed that the test rig foundation natural frequency is 2265 cpm which was seen clearly in most of the results. Sample data is given in Figure 3-30.

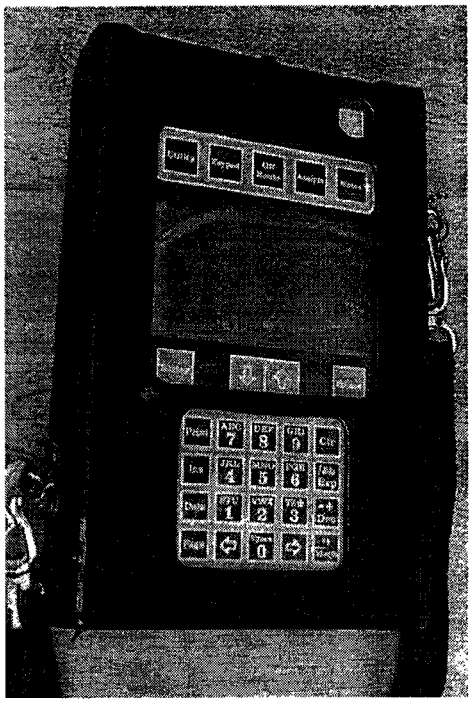

Figure 3-28 CSI 2115 Data Collector

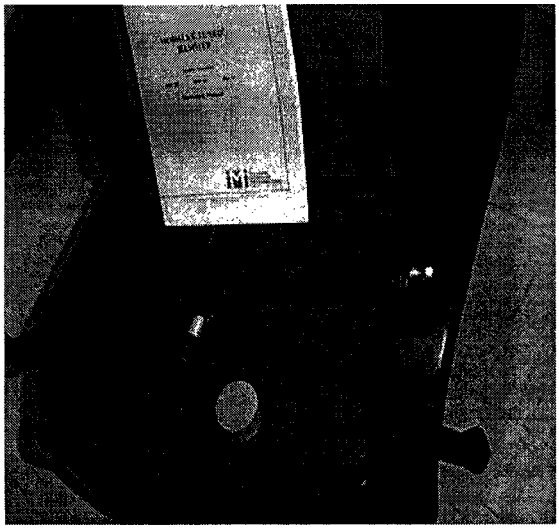

Figure 3-29 Modal Hammer

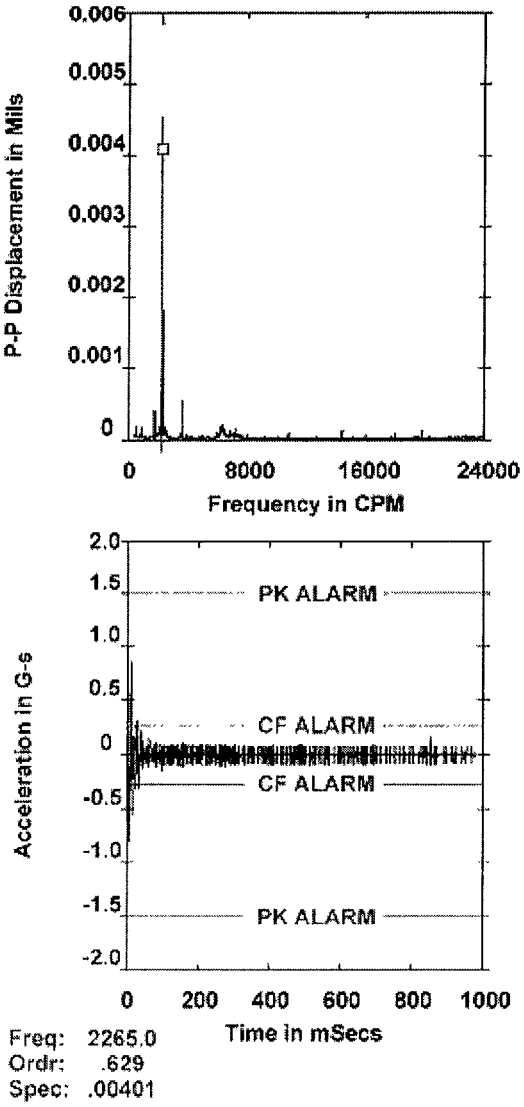

Figure 3-30 Foundation resonance frequency of 2265 cpm (impact test results)

After a series of impact tests on the rotor itself, as expected, the results show that the rotor natural frequency is minimum when the disk is in the shaft's mid-span and is increasing as the disk is moved to the ends. Samples of impact test plots are shown in Figure 3-31, including coherence and phase change across the natural frequency.

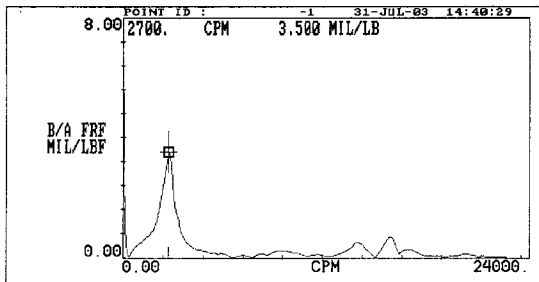

Transfer function (Displacement/ Force). Maximum displacement with lowest force at a frequency of 2700 cpm.

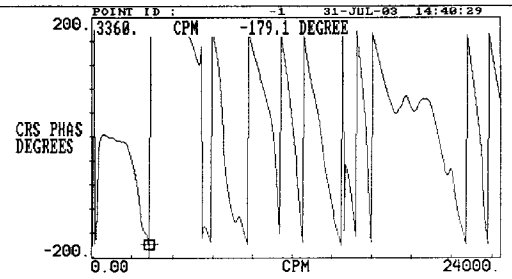

Phase change across the natural frequency showing a clear 180 deg phase shift across the natural frequency.

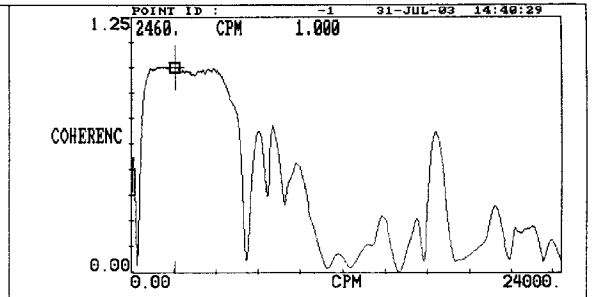

Coherence plot showing excellent input to output relation (100 %)

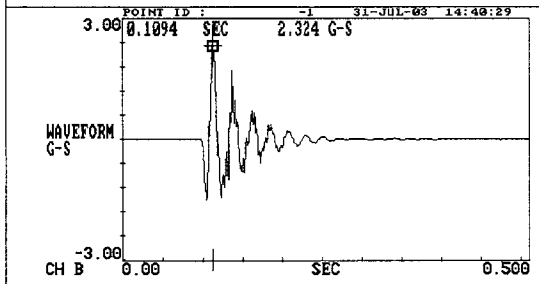

System's response decaying with time due to system's damping

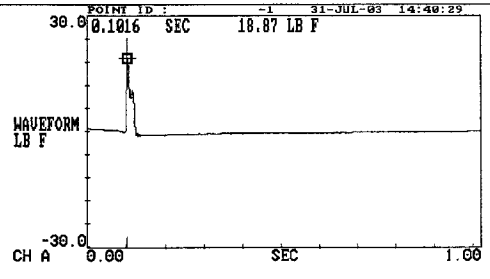

Force input as a step input force by the instrumented impact hammer

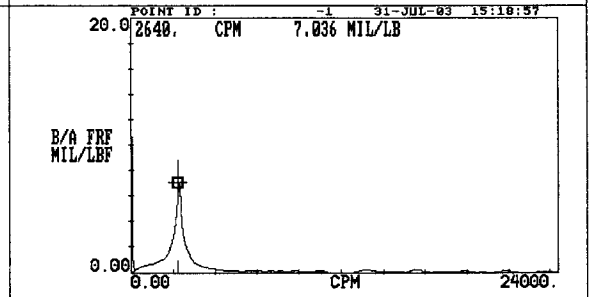

Response FFT. Natural frequency at about 2640 cpm

Figure 3-31 Graphical summary of impact test results

3.3.7 Exported data

Data was exported from the ADRE software to spread sheets for further processing and analysis. This was done because of ADRE restrictions on the predefined output plots. The exported data included the following: time, direct amplitude, 1X amplitude and phase, gap voltage and sample information. Two main constraints have to be mentioned here. First is the failure to compare efficiently data from separate tests. Second is the lack of access to adapt the variables in the programmed plots. Examples of the generated plots will be discussed in the following section. The mathematics behind these plots is discussed in the numerical chapter of the thesis.

3.3.8 Graphical representations

In this section, several plots extracted from the instability experiments are presented. Some of them are not available in the literature.

Figure 3-32 is a fundamental plot for the forthcoming plots. It embodies trends of the direct (unfiltered) vibration amplitude, the instability vibration amplitude (filtered to the instability frequency), the synchronous vibration amplitude and the calculated unbalance force. The data of the instability (frequency and amplitude) in this plot was collected manually. Such collection cannot be done using the existing instrumentations. The difficulty in doing this electronically is due to two reasons: first, filters are based on triggering signals (signal per revolution). This enables filtration of 1X and its harmonics but not on the fraction of the shaft speed, as in the case of oil instability. Second, even if there is a mapping to function the filter to detect a 0.47X amplitude, generating the plot may not be possible in the fluid induced vibrations because of the change in the frequency order, especially in the oil whip case, where the order decreases.

Figure 3-33 is the plot of the shaft average eccentricity ratio ε vector as the shaft speed increases. To produce this plot, the experimental data was manipulated from the gap voltage readings, as will be discussed in the next chapter. When the shaft is at rest, the ε is one. When ε is plotted against the vibration amplitude as in Figure 3-34, it explicitly clarifies the strong influence of ε on the threshold of instability. If the system has the potential to be instable, ε will be seen as gradually decreasing until the system becomes unstable (ε=0.38). Notice that generally speaking the instability amplitude is limited with a sealing as long as ε is not approaching small values.

The response plot is not repeatable, i.e. start up and shutdown plots are not identical due to the hysteresis in the system. This was found to be true for the amplitude, frequency and order. Notice the irreparable behavior in the startup and shutdown. Another observation on the same plot is the hysteresis effect on the shutdown part of the trend. The response in the shutdown is memory-based, i.e., the system continues to be unstable even if shaft speed is reduced to a stable speed during the startup. Stability demands a higher ε (0.57) during the shutdown.

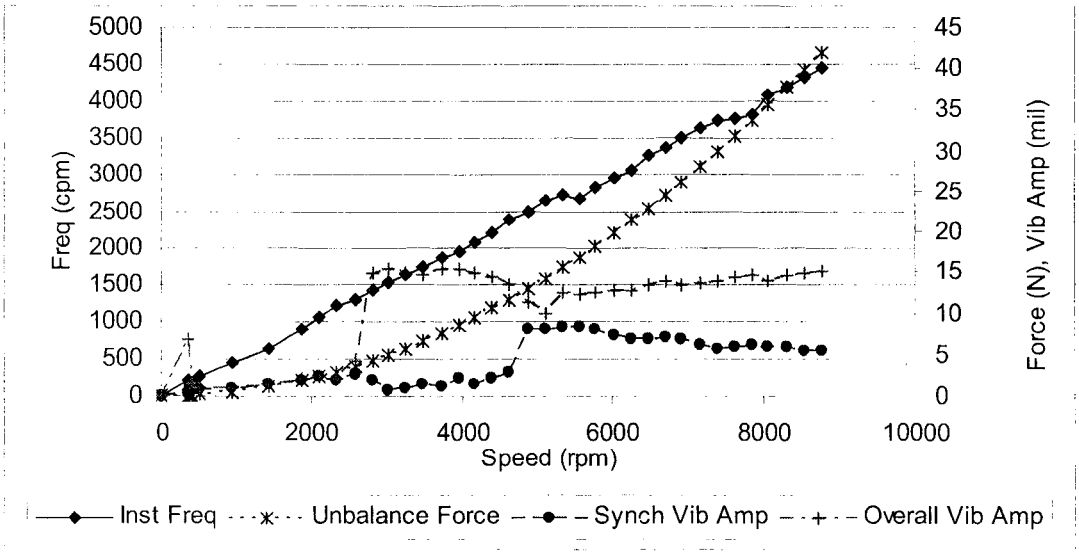

Figure 3-32 Data analyzed after exporting. Trend of instability amplitude

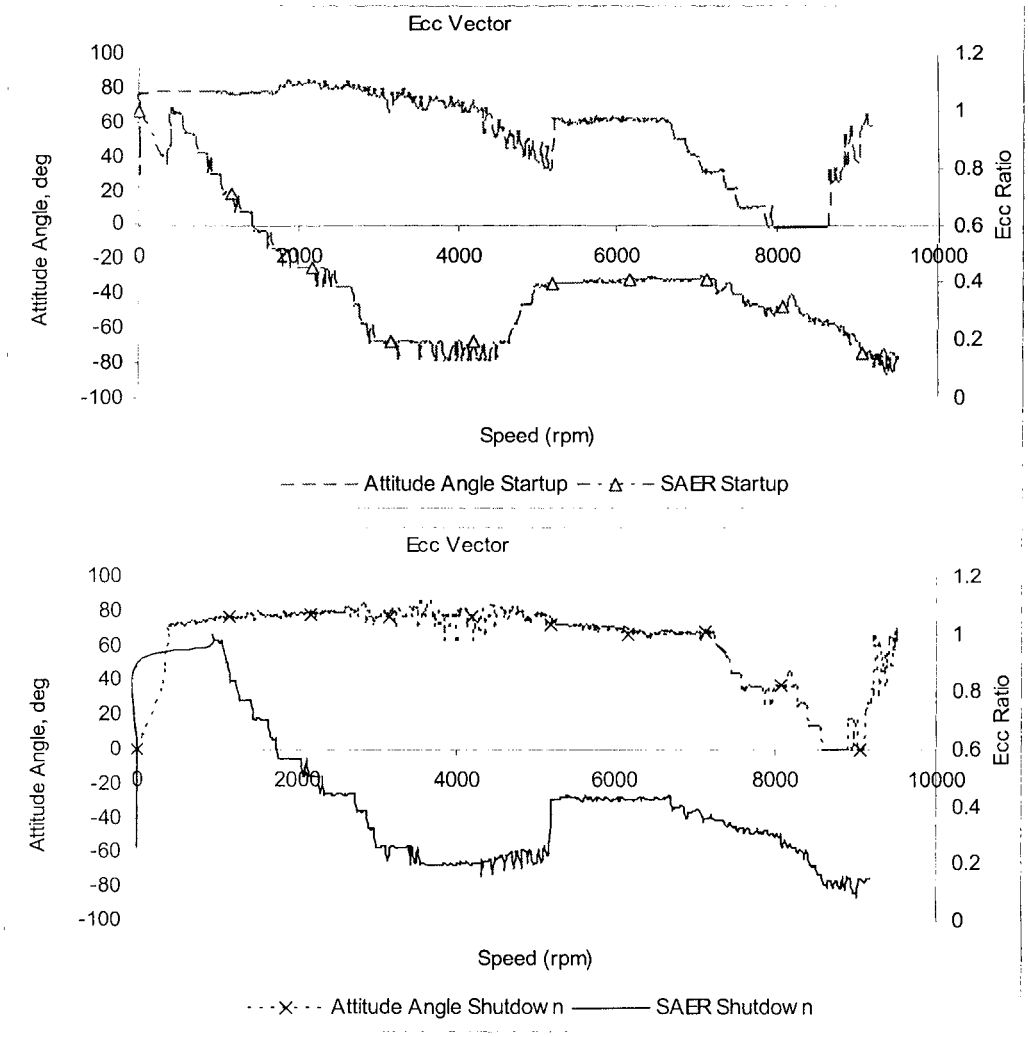

Figure 3-33 ε vector for startup (top) and shut down (bottom)

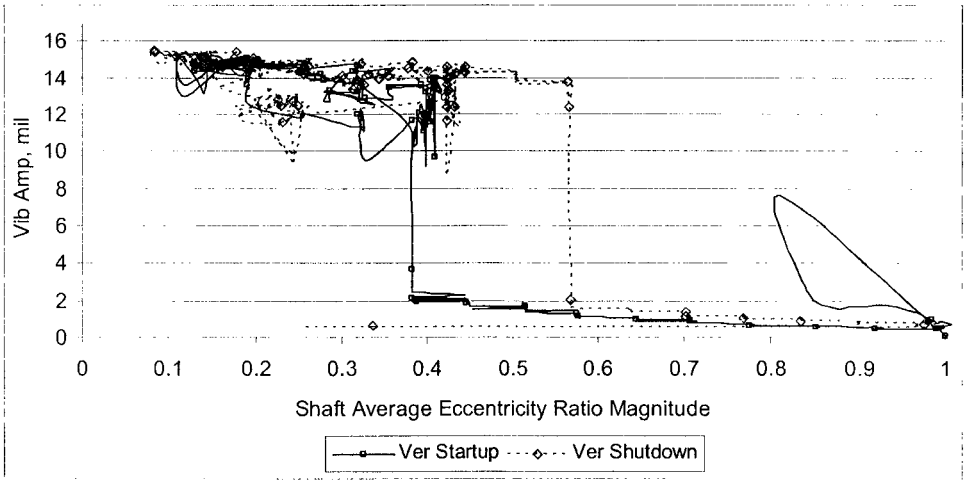

Figure 3-34 Instability amplitude as a function of ε

The magnitude of ε is the weighted displacement made by the shaft from the bearing center and the angle of ε is measured from the vertical axis in the direction of rotation. The angle starts from zero and then moves suddenly as a result of the slow roll motion, (Figure 3-34). It was noticed that ε is affected by dynamic and static loads.

Another example of the graphical representations is Figure 3-38 which shows a comparison of the unbalance force effect on the instability amplitude and on the synchronous vibration amplitude. Notice that the summation of both amplitudes is almost equal to the direct value (overall vibration). This note is related to the explanation of the constant overall vibration amplitude when the fluid induced instability is active together with the unbalance. The unbalance has a clear effect on the amplitude of both the subsynchronous and the synchronous amplitudes. It was noticed that the 1X amplitude will rise on the advantage of the instability, but the overall vibration level stays, more or less, the same.

Figure 3-36 shows the effect of unbalance on the instability order. There is a slight inconsistent fluctuation. This figure is collected from a test with a shaft length of 300 mm and a disk location of 60 mm.

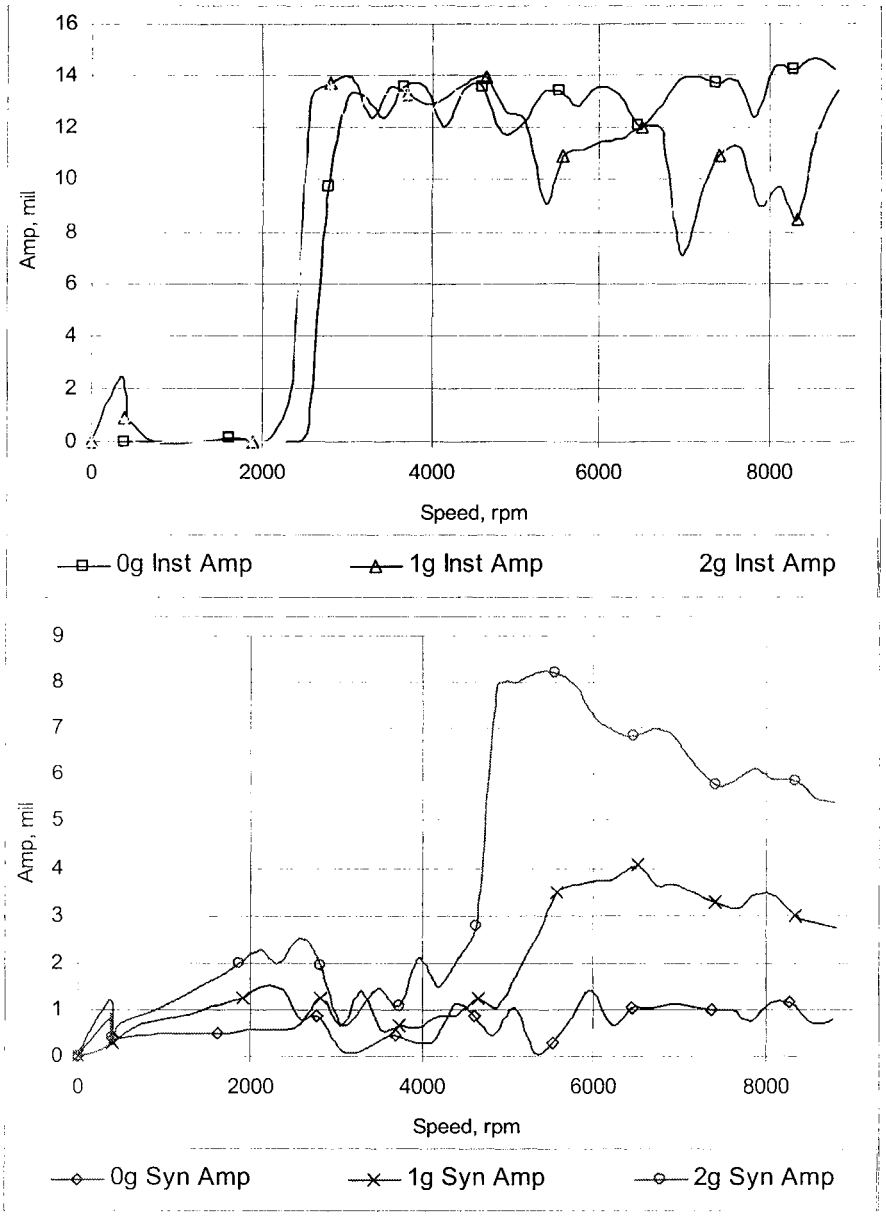

Figure 3-35 Effect of unbalance on the instability (top) and synchronous amplitudes (bottom)

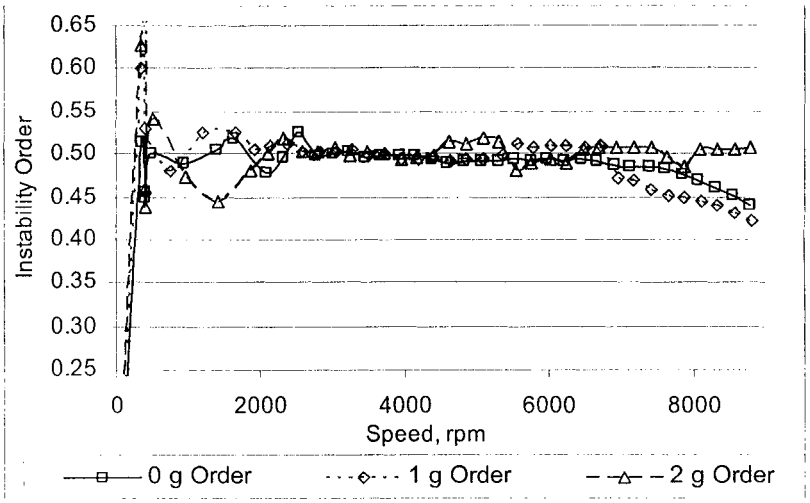

Figure 3-36 Effect of the unbalance on the instability order

CHAPTER 4

NUMERICAL COMPUTATIONS

4.1 Introduction

In this chapter, a rotor mounted on a fluid film bearing is modeled and its oil instability response is presented. The bearing is modeled as springs and dampers representing both energy storing and dissipating elements of the bearing fluid film. The following section will illustrate the method used in evaluating the stiffness and damping values. Later sections are dedicated for the analysis of the numerical results obtained from *Xl-Rotor* program applied in the fluid film instability modeling. First, general stability analysis will be addressed. Then, the effects of the shaft length and the disk location on the instability are studied.

4.1.1 Bearing Properties

To obtain the stiffness and damping of the bearing, the bearing fluid forces acting on the journal surface are calculated by integration of the pressure field. Mathematically, this can be written as:

$$\begin{bmatrix} F_r \\ F_t \end{bmatrix} = \int_0^L \int_0^{2\pi} P(\theta, z) \begin{bmatrix} \cos\theta \\ \sin\theta \end{bmatrix} R \, d\theta \, dz \qquad (4\text{-}1)$$

where F_r and F_t are the radial and tangential force components, as shown in Figures 4-1 and 4-2, P is the pressure developed in the oil film, θ is the position angle moving with the direction of rotation from the line connecting center of the journal and bearing, z is the axial journal location ($-L/2 \le z \le +L/2$, where L is the bearing length), R is the journal bearing radius.

The journal forces along with their corresponding displacements and velocities can be related to approach the stiffness and damping properties as follows:

$$F_X = -K_{xx}\Delta x - C_{xx}\Delta \dot{x} - K_{xy}\Delta y - C_{xy}\Delta \dot{y} \tag{4-2}$$

$$F_Y = -K_{yx}\Delta x - C_{yx}\Delta \dot{x} - K_{yy}\Delta y - C_{yy}\Delta \dot{y} \tag{4-3}$$

where F_X and F_Y are the decomposed journal forces when journal is displaced from its center. As an example for the notation used in the previous equations, the stiffness term $K_{xy} = \frac{\partial F_X}{\partial y}$ is acting due to a force in the x-direction but with a displacement in the y-direction, as shown in Figure 4-3. The physical representation of the other stiffness and damping coefficients follow the same subscript symbology. Notice that though the weight of the journal is pure radial vertical, the fluid film bearing has an asymmetric response (unisotropic characteristic) due to the cross-coupled stiffness. This means that if there is a load release in the vertical direction, it will be accompanied by a motion in the horizontal direction due to cross the coupled stiffness. A similar scenario applies to the damping. Remember, coordinate transformation of the forces might be applied to find Equations 4-2 and 4-3 as follows:

$$F_X = F_r \cos \phi - F_t \sin \phi \tag{4-4}$$

$$F_Y = F_r \sin \phi + F_t \cos \phi \tag{4-5}$$

where ϕ is the attitude angle as shown in Figure 4-1.

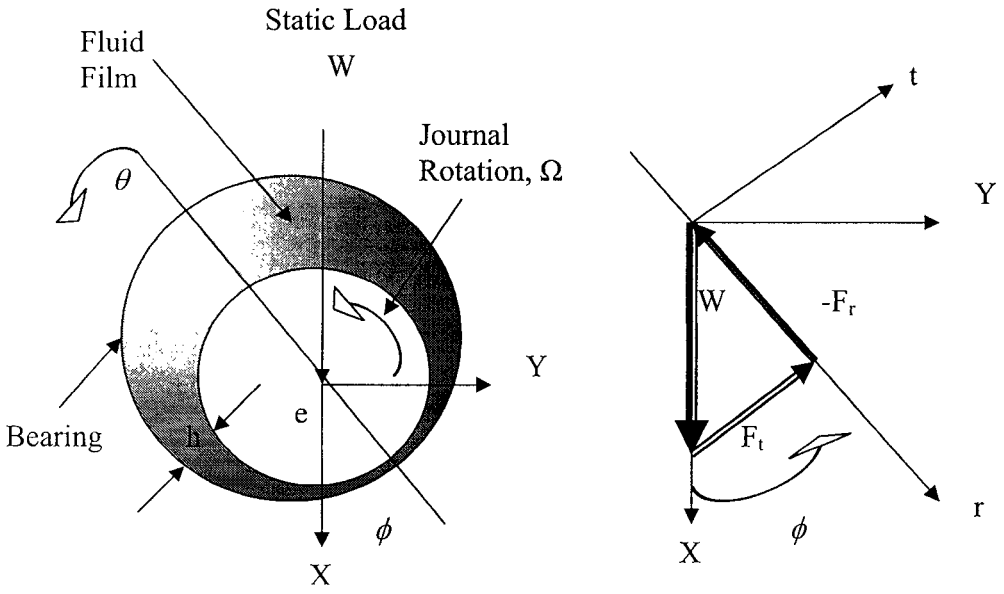

Figure 4-1 Bearing-journal Model

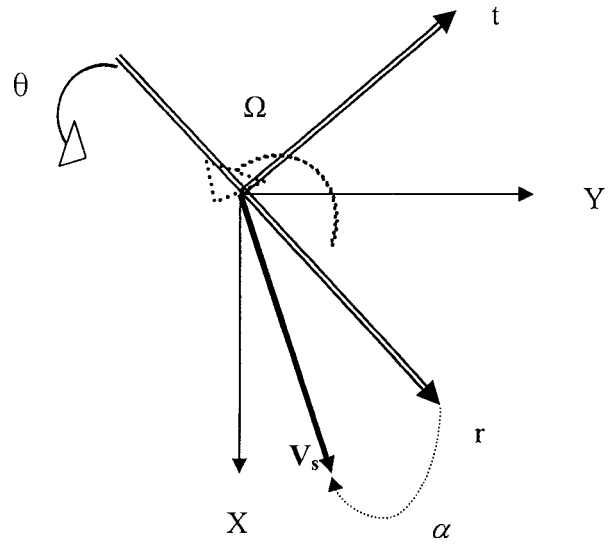

Figure 4-2 Notation for force equilibrium

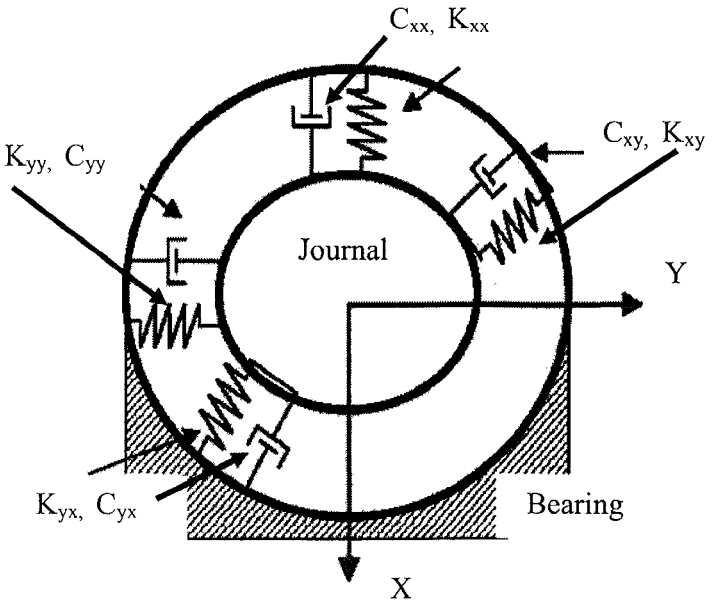

Figure 4-3 The eight bearing mechanical properties [35]

For a radial fluid film bearing drawn schematically in Figures 4-1 and 4-2, Reynolds equation is [35]:

$$\frac{1}{R^2}\frac{\partial}{\partial\theta}\left\{\frac{h^3}{12\mu}\frac{\partial P}{\partial\theta}\right\}+\frac{\partial}{\partial z}\left\{\frac{h^3}{12\mu}\frac{\partial P}{\partial z}\right\}=V_s\cos(\theta+\alpha) \tag{4-6}$$

where h is film thickness (function of θ and t), μ is the oil viscosity, V_s and α are the magnitude and lead angle of the pure squeezed velocity. Remember that C is the bearing clearance and e is the eccentricity, which are going to be used in the following formulation.

For a short bearing (L/D<2), it is established that $\frac{\partial P}{\partial\theta}\approx 0$ and consequently, Reynolds (4-6) equation can be reduced to:

$$\frac{\partial}{\partial z}\left\{\frac{h^3}{12\mu}\frac{\partial P}{\partial z}\right\} = V_s \cos(\theta+\alpha) \tag{4-7}$$

Pure squeezed velocity, V_s, is the time rate of change of e relative to a coordinate system that has an angular velocity $\Omega/2$ relative to the stationary coordinate system (X, Y). Notice that equation (4-7) can be integrated to find pressure directly since h is not function of the axial coordinates. After the integration and some manipulations, the pressure distribution can be found as,

$$P(\theta,z) = P_a + \frac{6\mu V_s \cos(\theta+\alpha)}{C^3 H^3}\left\{z^2 - (\frac{L}{2})^2\right\} \tag{4-8}$$

where P_a is the atmospheric pressure, $H = \frac{h}{C} = 1+\varepsilon\cos\theta$, ε is the eccentricity ratio and

$$h = C + e\cos(\theta) \tag{4-9}$$

Having the expression of pressure, the forces in equation (4-1) can be found by substitution of $P(\theta,z)$ in Equation (4-8). With the aid of Booker's Journal Tables, the force equations in Equation (4-1) for plain bearings are given as follows:

$$F_r = \frac{-\mu R L^3 \Omega \varepsilon^2}{C^3(1-\varepsilon^2)^2} \tag{4-10}$$

$$F_t = \frac{\pi\mu R L^3 \Omega \varepsilon}{4C^2(1-\varepsilon^2)^{3/2}} \tag{4-11}$$

At this stage, the magnitude of the load, W, can be expressed as below:

$$W = \sqrt{F_r^{\,2} + F_t^{\,2}} = \frac{1}{4}\mu\Omega R L (\frac{L}{C})^2 [\frac{\varepsilon\sqrt{16\varepsilon + \pi(1-\varepsilon)}}{(1-\varepsilon)}]$$

or

$$W = \frac{1}{4}\mu\Omega R L (\frac{L}{C})^2 [\frac{1}{\sigma}] \tag{4-12}$$

where σ is defined as the modified Sommerfeld number. For the application of plain bearing, one can rewrite it as:

$$\sigma = \frac{1}{4W}\mu\Omega R L (\frac{L}{C})^2 = \frac{(1-\varepsilon^2)^2}{\varepsilon\sqrt{16\varepsilon^2 + \pi^2(1-\varepsilon^2)}} = \pi S (L/D)^2 \tag{4-13}$$

where S is the Sommerfeld number. Figure 4-4 shows modified Sommerfeld number as a function of ε and the theoretical motion of the shaft inside the bearing clearance circle is shown in Figure 4-5. Sommerfeld number can be looked at as an indication of journal position inside bearing clearance circle as a result of all loads and bearing factors affecting the shaft position.

When the load W is decomposed into tangential and radial components, the *Attitude Angle* can be expressed as:

$$\tan\phi = -\frac{F_t}{F_r} = \frac{\pi\sqrt{1-\varepsilon^2}}{4\varepsilon} \tag{4-14}$$

The attitude angle represents the angular shift of the journal from the vertical centerline to the position of the current minimum fluid film thickness in the direction of the rotation. To link the attitude angle to S, the trajectory of the attitude

angle has been plotted on the same graph with the Sommerfeld number in Figures 4-4 and 4-5.

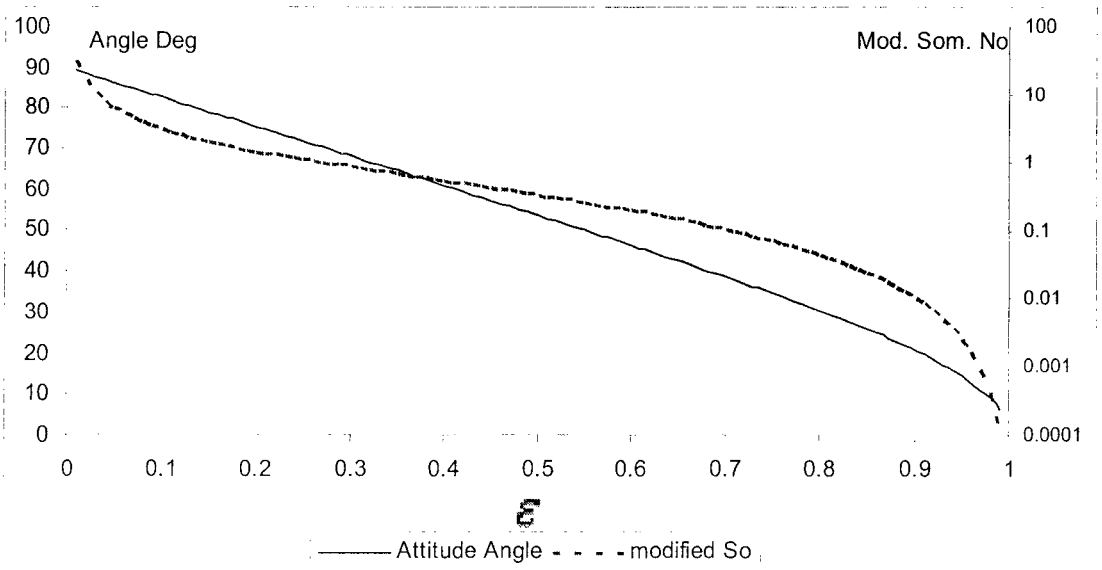

Figure 4-4 Modified Sommerfeld and Attitude Angle vs ε

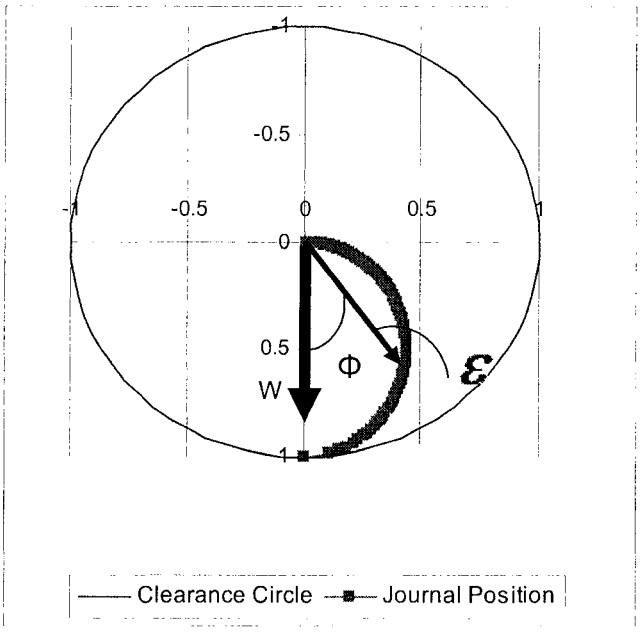

Figure 4-5 2-D prediction of journal position

Notice that the Sommerfeld number provides the necessary link between the journal loads and the bearing mechanical properties through the location of the journal in the bearing clearance circle. For a certain bearing construction, the stiffness and damping properties in Equations (4-2) and (4-3) can be found. Figures 4-6 and 4-7 are the results of this calculation for the case of plane bearing (un-damped un-grooved) with L/D=1.

Under steady state conditions, the calculations of K's and C's are made based on the following list of assumptions:

1. The lubricant is incompressible and obeys Newton's laws of viscous flow. Fluid viscosity of the lubricant is constant throughout the film.

2. Lubricant inertia effects are minor and neglected.

3. The flow in the axial (z) direction is ignored. The velocity of a lubricant particle depends on its x and y coordinates

4. The curvature of the bearing can be ignored.

For more details on the formulation, refer to [35-36].

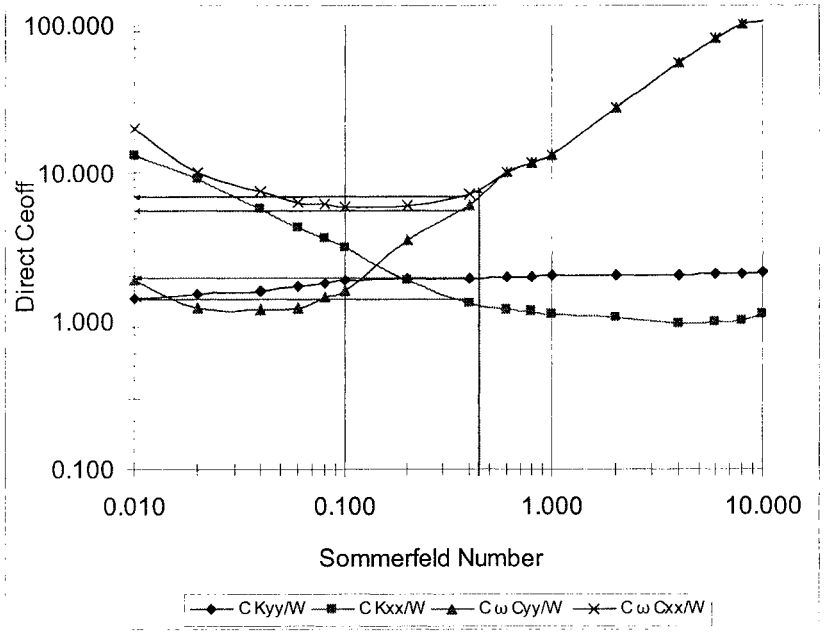

Figure 4-6 Direct properties vs Sommerfeld Number

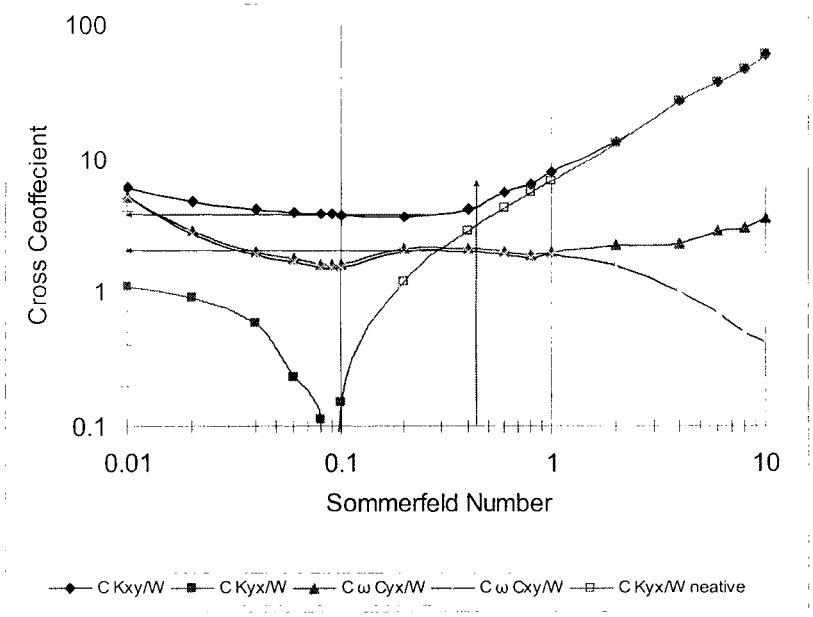

Figure 4-7 Cross properties vs Sommerfeld Number

4.1.2 Bearing Properties Sample Calculation

The following manual methodology is presented to illustrate how to find bearing parameters for a rotor setup using the Sommerfeld number and the corresponding figures (Figures 4-6 and 4-7). All assumptions mentioned earlier apply.

Journal Length, L= 0.025 m

Journal Diameter, D= 0.025 m

Oil Dynamic Viscosity, μ= 0.0274 N sec/m^2

Radial Clearance, C= 0.0004318 m (= 0.017 in)

Speed, N = 6000 rpm , hence ω= 628 rad/sec

Rotor Mass, M= 1 kg

Rotor Weight, W_{tot}= 9.81 N

Weight on Fluid Film Bearing, W= 4.905 N

Journal ratio, L/D= 1

Sommerfeld No $S = \frac{\mu DLN}{W}\left[\frac{R}{C}\right]^2 = 0.46$

Using S and Figure 4-6 Direct Parameters are found as follows:

$K_{yy}Coeff = \frac{C K_{yy}}{W} = 1.9$, thus K_{yy}=2.16E+04 N/m = 123.24 Lb/in

$K_{xx}Coeff = \frac{C Kxx}{W} = 1.5$, thus K_{xx}=1.70E+04 N/m = 97.29 Lb/in

$C_{yy}Coeff = \frac{C \omega C_{yy}}{W} = 6.1$, thus C_{yy}= 1.10E+02 N*sec/m = 0.63 Lb*sec/in

$C_{xx}Coeff = \frac{C \omega C_{yy}}{W} = 7.1$, thus C_{xx}= 1.28E+02 N*sec/m = 0.73 Lb*sec/in

Using S and Figure 4-7, Cross Parameters are found similarly as follows:

$K_{yx}Coeff = \frac{C\,K_{yx}}{W}$ = -3, thus K_{xy}= -3.41E+04 N/m = -194 Lb/in

$K_{xy}Coeff = \frac{C\,Kxy}{W}$ = 5, thus K_{xy}= 5.6E+04 N/m = 324 Lb/in

$C_{yx}Coeff = \frac{C\,\omega\,C_{yx}}{W}$ = 2, thus C_{yy}= 36.2 N*sec/m = 0.21 Lb*sec/in

$C_{xy}Coeff = \frac{C\,\omega\,C_{xy}}{W}$ = 2, thus C_{xx}= 36.2 N*sec/m = 0.21 Lb*sec/in

4.2 Numerical Solution (XI-Rotor)

4.2.1 Effect of bearing load on its properties

The general bearing model calculation relies on a long list of changing parameters (e.g. lubricant type, viscosity, bearing preload etc.) with different levels of significance on the final bearing characteristics. Particularly to the problem under consideration, both bearing load and eccentricity are major factors.

Bearing load is expressed in two forms, either weight carried by the bearing or load per bearing unit area. They are related as follows:

$$P = \frac{W}{LD} \tag{4-15}$$

where P is the bearing load, W is the weight on the bearing, L is bearing length and D is the bearing diameter.

Figures 4-8 and 4-9 are the numerical solutions from XI-Rotor [37] for the direct stiffness (K_{xx} and K_{yy}), direct damping (C_{xx} and C_{yy}), cross-coupled stiffness (K_{xy}, K_{yx}) and cross-coupled damping (C_{xy}, C_{yx}) values as functions of the Sommerfeld number for the bearing used in the analysis. Notice that K_{yy} is initially

large (as it is close to the bearing wall) and then decreases with the shaft lift. Also, notice the symmetry between each pair.

As given before, the Sommerfeld number, S, is directly proportional to the shaft, Ω, speed and hence the above plots can be converted into the speed domain. The converted plots give more sense to the behavior of the machine. This is illustrated in Figures 4-10 and 4-11.

In real life problems, the bearing load may be reduced (or intentionally increased) by shaft alignment and by changing bearing contact areas. To examine the effect of bearing load on the model, the same bearing is modeled with bearing load reduced to one-half. Notice the changes due to load reduction in Figure 4-12 and 4-13 compared to Figure 4-10 and 4-11, respectively.

The disk weight represents a major part of the system weight and is a major contributor to the fluid film bearing load. Since the disk's location is changed along the axial direction, the load on the fluid film bearings will change as the disk is relocated. Consequently, the fluid film bearing stiffness and damping are dependant on the disk location. The load effect due to disk location on the instability was not clearly addressed in the literature.

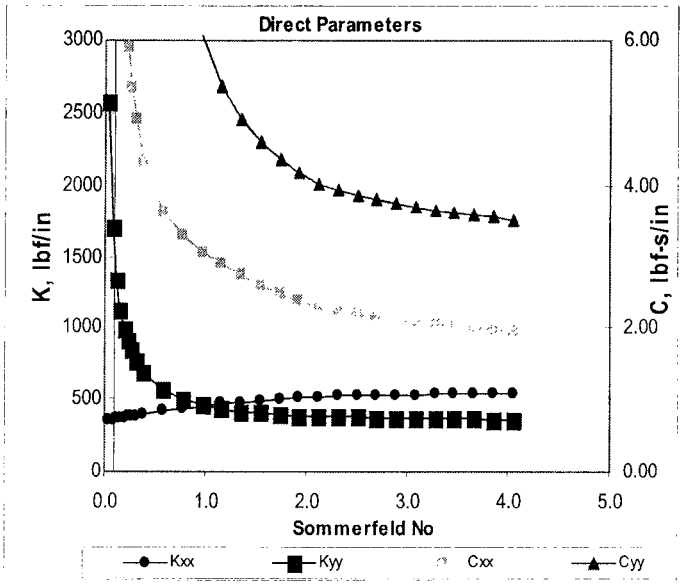

Figure 4-8 Numerical solution to model direct parameters

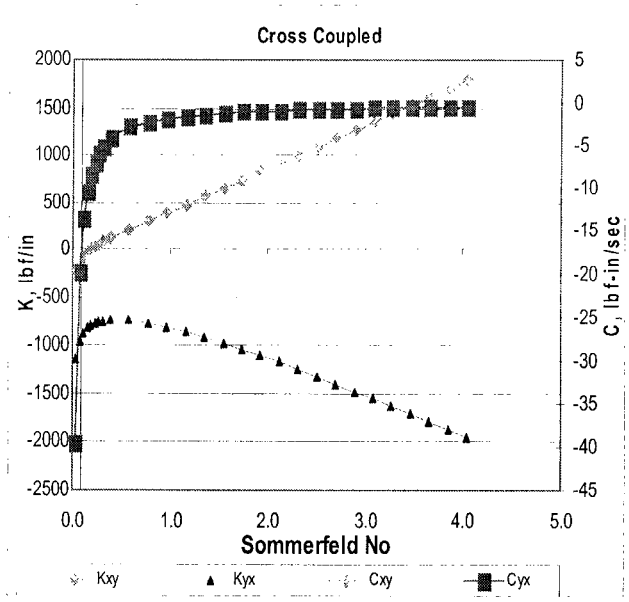

Figure 4-9 Numerical solution to model cross parameters

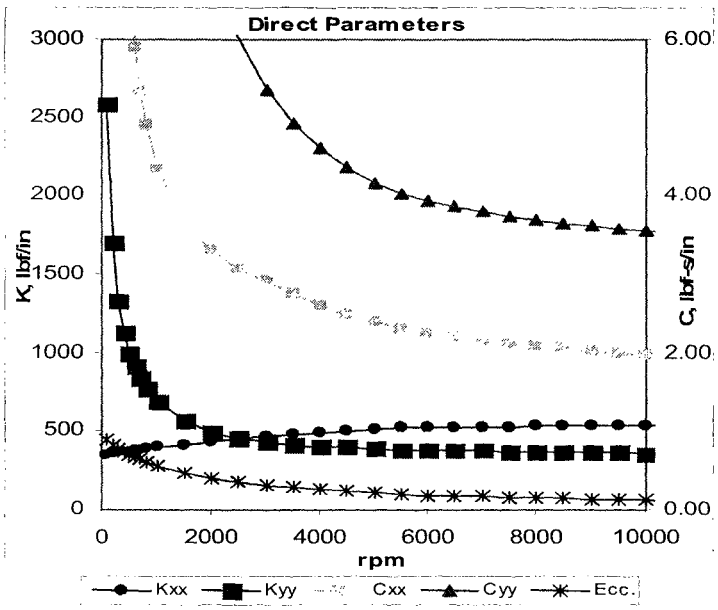

Figure 4-10 Numerical solution to model direct parameters as a function of speed

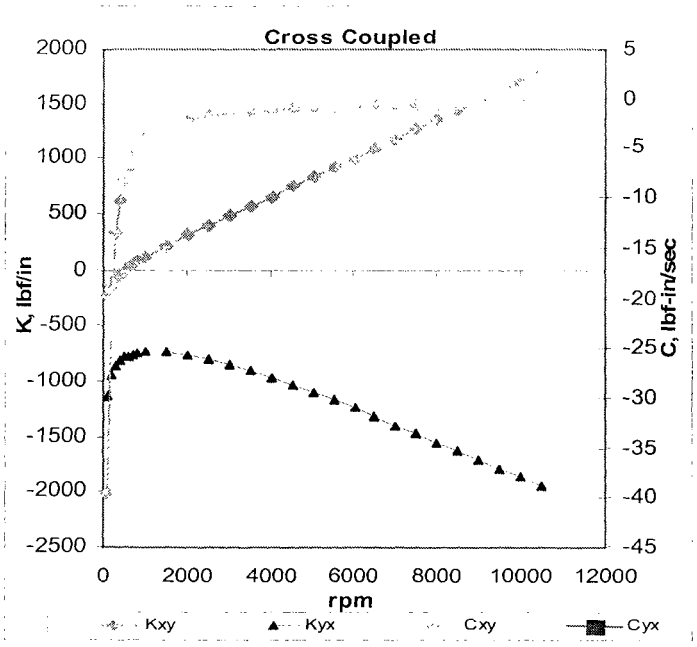

Figure 4-11 Numerical solution to model cross parameters as a function of speed

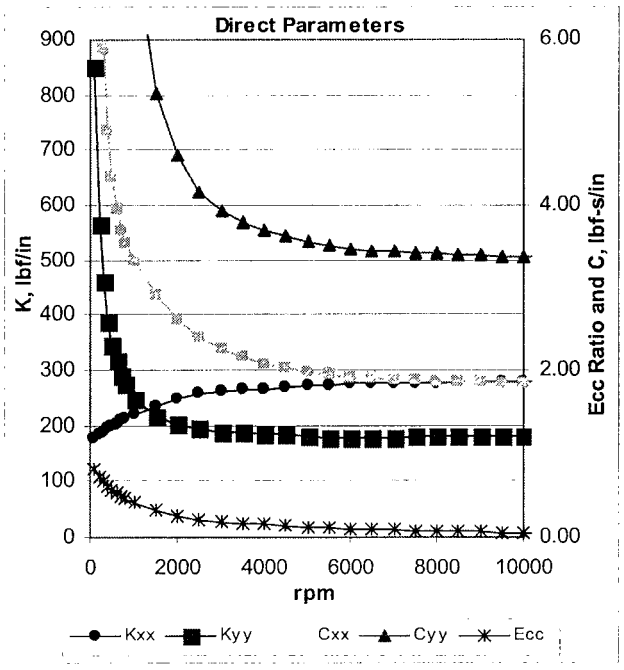

Figure 4-12 Direct properties affected by load reduction

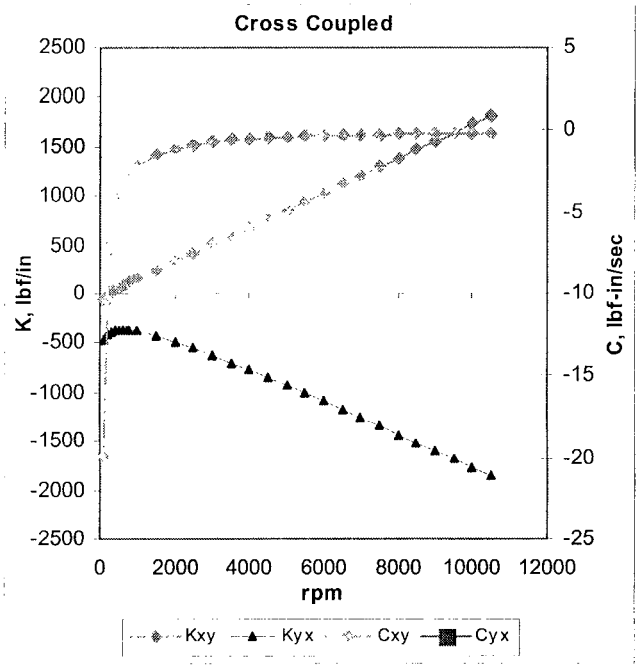

Figure 4-13 Cross properties affected by load reduction

4.2.2 The Model

The model is considered as an anisotropic system due to the significant variation in the mechanical properties in the radial direction (horizontal and vertical). When the rotor runs at slow speeds, its position is close to the bottom of the bearings; when speed increases, it never reaches the bearing center but it approaches. In all cases the stiffness and damping parameters are not equal in the vertical and horizontal directions.

Figure 4-14 shows the system modeled on Xl-Rotor. This code is based on transfer matrix and finite element calculations. The results presented are based on finite element calculations. In modeling the system, the following are defined numerically: dimensions (for shaft, disk and bearings), material properties (for shaft, disk and bearings) and boundary conditions. As an example, the model in Figure 4-14 is for the following setup: shaft length (l) is 400 mm, disk location (l') is 200 mm away from the fluid film bearing, with 20 elements (stations). The fluid film bearing is in station 1 while the sleeve bearing is modeled as pinned boundary condition at station 20. Material, dimensional and unbalance properties are shown in Tables 4-1 to 3. I_t and I_p are the transverse and polar, respectively, weight moments of inertia computed for the beam, after weighted summation for all stations. Fluid film bearing load is1.3 lbf (5.78 N). Bearing is modeled with zero preload. Oil used in lubrication is ISO VG 32 operating at 100^o F (40^o C).

Eigenvalue calculation is performed on the span of 200-10000 rpm with steps of 200 rpm. This increment was adjusted after several trials and found to be adequate. The response results are calculated for Station 2.

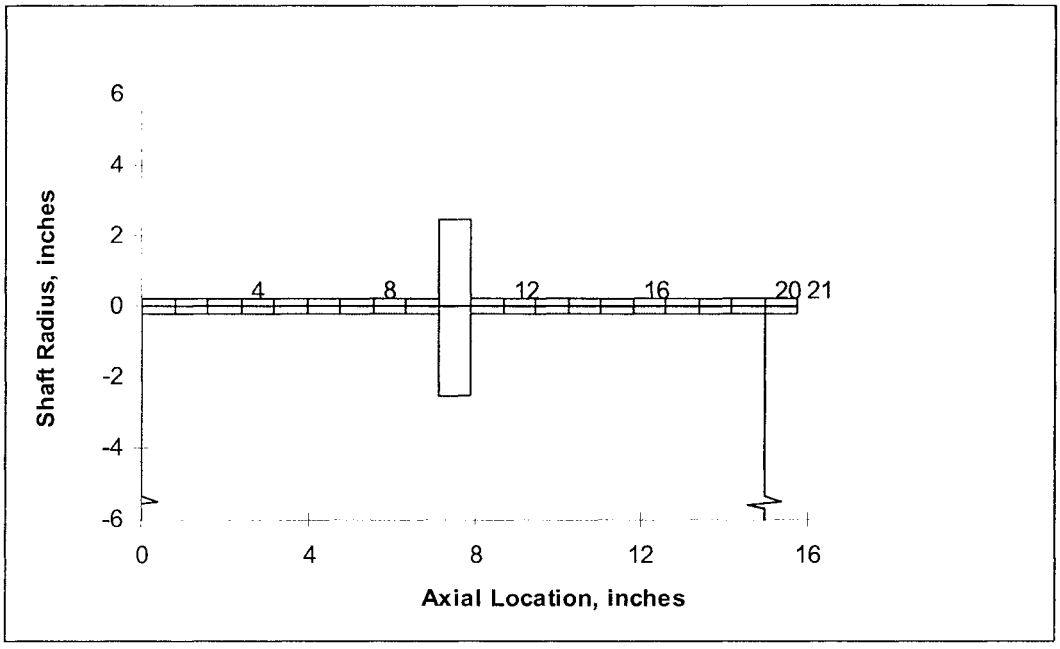

Figure 4-14 Graphical presentation of model used in Xl-Rotor software

Table 4-1 Material properties

Weight Density (lb/in^3)	Elastic Modulus (psi)	Shear Modulus (psi)
0.283	30.0E+6	12.0E+6

Table 4-2 Dimensional parameters

First Station	Last Station	Total Length (inches)	Total Mass (lbm)	Total Level Inertia I_t, (lbm-in^2)	Total Level Inertia I_p, (lbm-in^2)
1	21	15.748	2.543	24.215	0.972

Table 4-3 Unbalance parameters

Unbalance Station	Unbalance Amount (gm-in)	Unbalance Phase (degrees)
10	2.51	0

4.3 Results

4.3.1 General Results

Figures 4-15 to 4-20 show a comparison of the system's response before and after the instability has started, at speeds 3000 and 4000 rpm respectively. The displacement response is given in horizontal and vertical directions which is designated by D(2)x and D(2)y, respectively. The number between in parentheses represents the station from which the data is collected; station 2 in this particular case. Prior to the instability, the time waveform is steady and shows a pure sinusoidal behavior. The frequency of the signal can be taken from the corresponding spectrum which shows a synchronous amplitude due to the mass unbalance (Figure 4-17). As expected, the orbit is circular (Figure 4-19).

In Figure 4-16, notice the increasing amplitude of the time waveform and the distortion of the pure sinusoidal wave. Due to the instability, the frequency of the vibration is not unique and can be seen in the corresponding spectrum, in Figure 4-18. The amplitude of the unbalance (at 4000 rpm or 66.7 Hz) is small compared to that of the instability, which is clearly subsynchronous. Notice the widening in the orbit's size (Figure 4-20).

The existing definition of the instability threshold in the literature does not distinguish clearly between the initiation of the subharmonic frequency and the speed at which the system will be actually unstable. In other words, if the subharmonic frequency appeared in a small amplitude, it does not mean that the system has got into the instability yet. See the response of the system in Figure 4-21 for a speed slightly less than the "threshold of instability" at 3800 rpm. The corresponding spectrum in Figure 4-22 clearly shows both synchronous and subsynchronous amplitudes. Though it is clear from the spectrum that the subharmonic frequency is playing a role in distorting the waveform, the vibration amplitude is not increasing.

Figure 4-23 is the numerical solution for the eigenvalues (natural frequencies) of the rotor-disk-bearing system. Though the plot illustrates three natural frequencies, the numerical solution was based to find at least six solutions, some of which are above the frequency range of interest (>10000 cpm). Figure 4-24 is taken from [1] where a similar system was modeled analytically using the *CDS* to find the characteristic equation. It was linearized and then solved using assumed forms of solution. Notice the qualitative matching with the numerical solution obtained from Xl-Rotor.

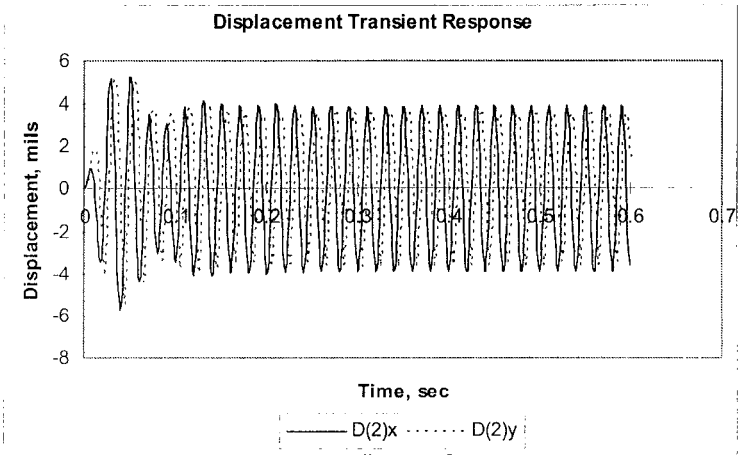

Figure 4-15 Waveform response before instability (at 3000 rpm)

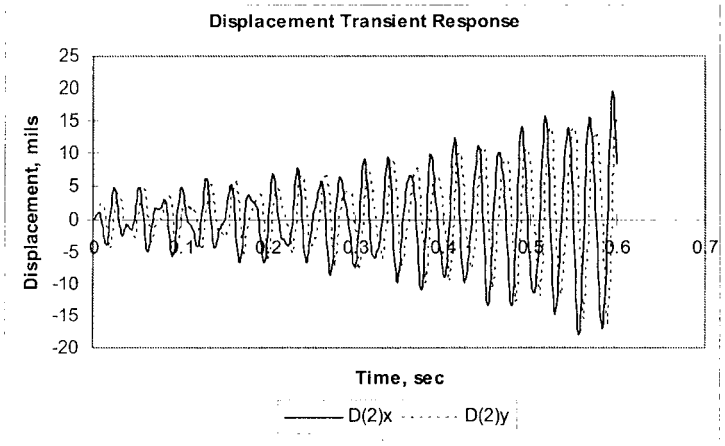

Figure 4-16 Waveform response after instability (at 4000 rpm)

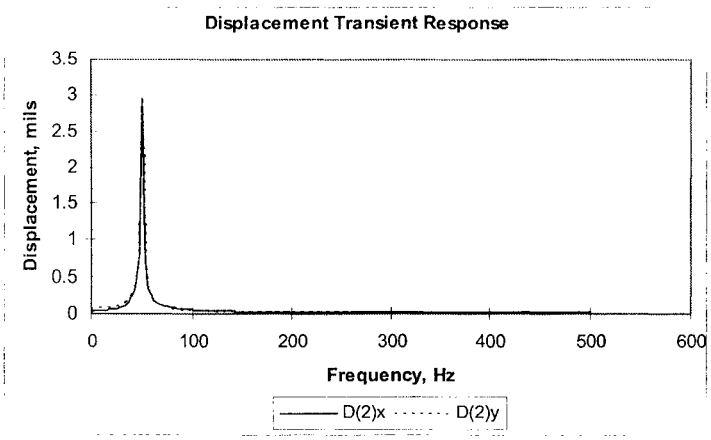

Figure 4-17 Spectrum response before instability (at 3000 rpm)

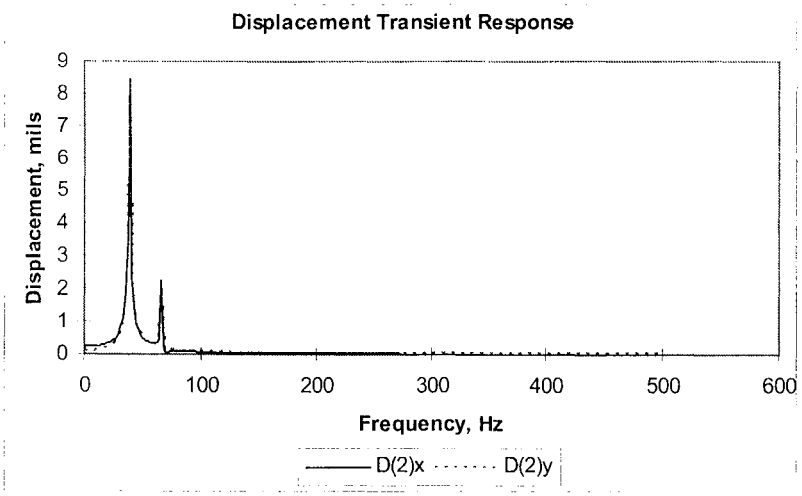

Figure 4-18 Spectrum response after instability (at 4000 rpm)

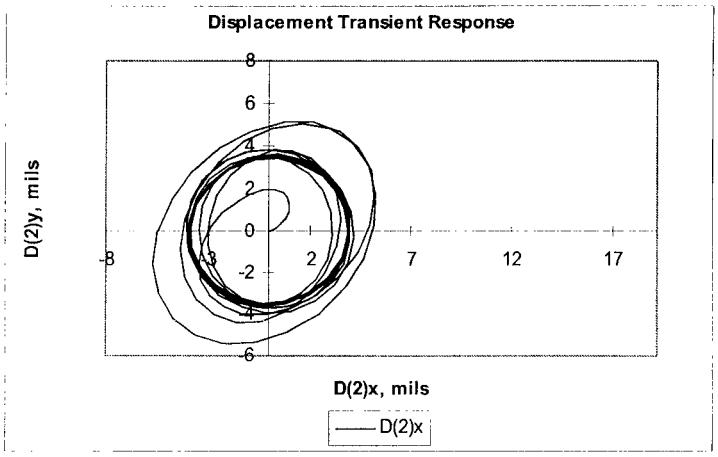

Figure 4-19 Orbit response before instability (at 3000 rpm)

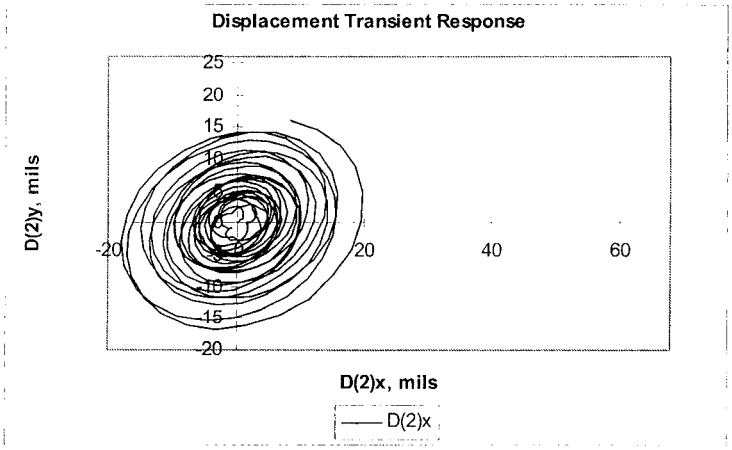

Figure 4-20 Orbit response after instability (at 4000 rpm)

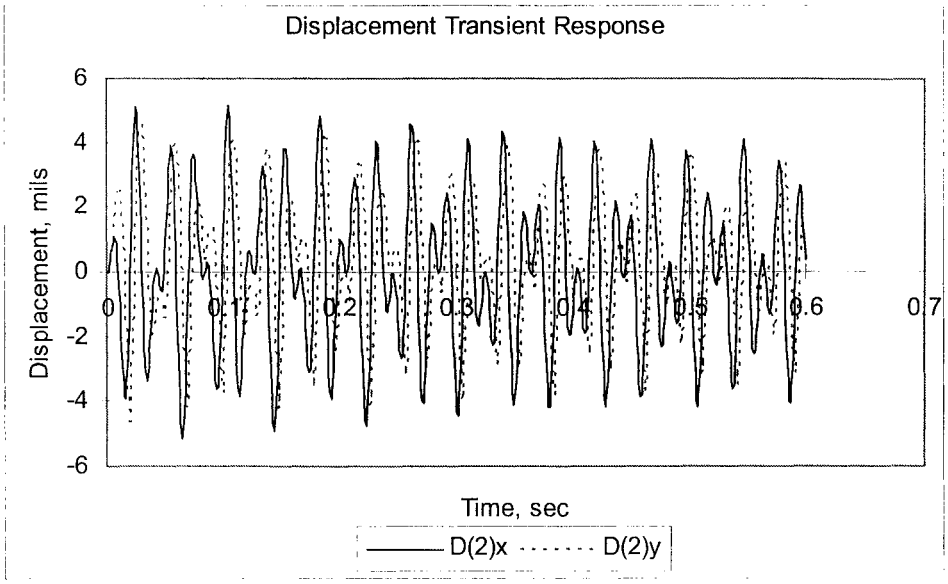

Figure 4-21 Synchronous signal distorted by sub-synchronous signal

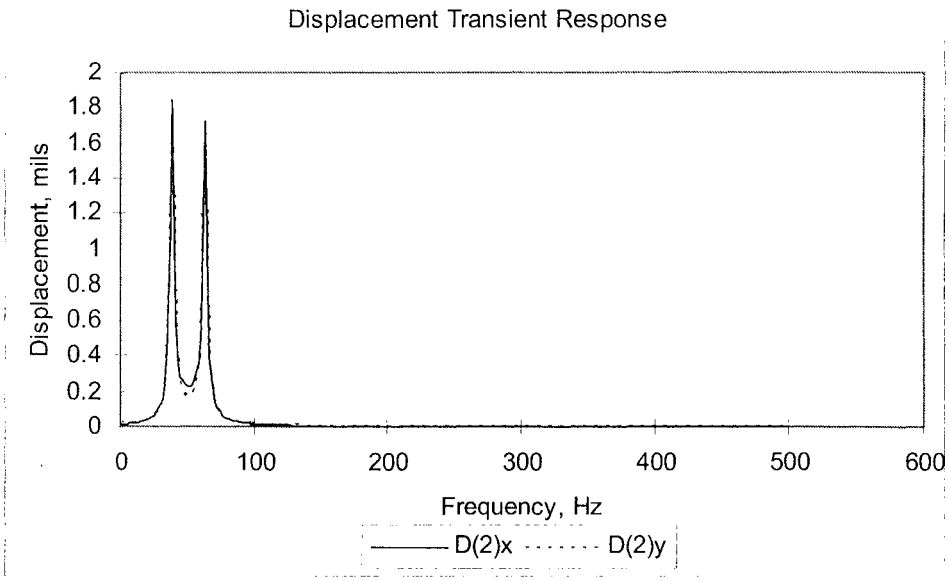

Figure 4-22 Amplitudes of synchronous and sub-synchronous vibration

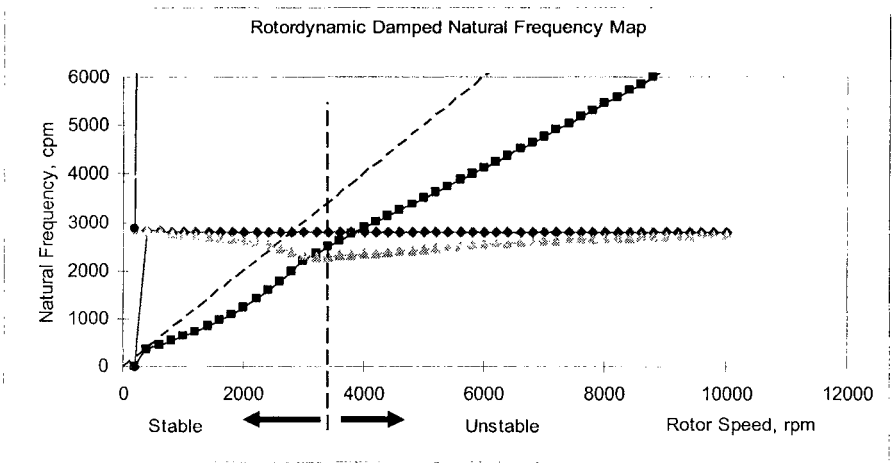

Figure 4-23 Natural frequency map (Campbell Diagram)

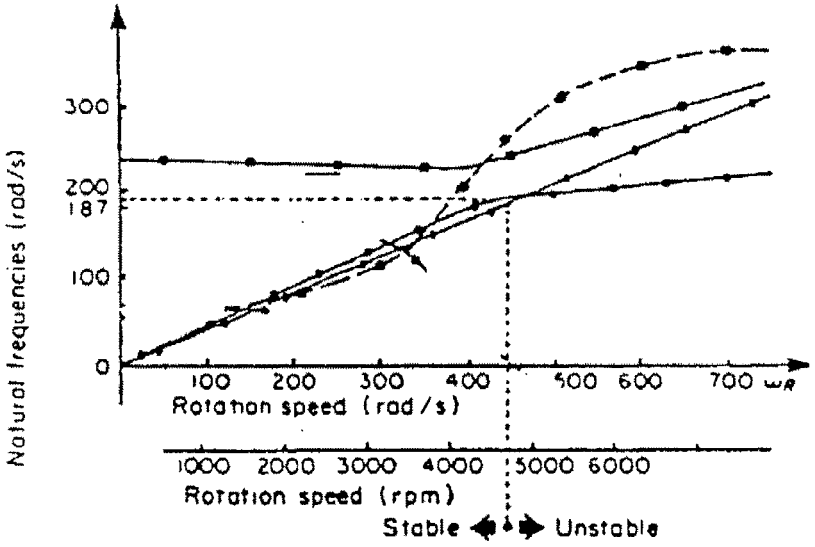

Figure 4-24 Natural frequency map for a similar system solved by CDS

(part of the original [1])

Notice in Figure 4-23 the increasing trend of some natural frequencies while others are nearly flat. This trend is interpreted as the effect of the fluid and solid properties on the system's natural frequencies, i.e. related to whirl and whip.

Bode plot in Figure 4-25 shows the response of the system due to the unbalance. From this plot, the predicted critical speed is about 2650 rpm which is in a good agreement with the experiential results for the same set up. (For example Figure 3-31 showed a natural frequency of 2640 cpm).

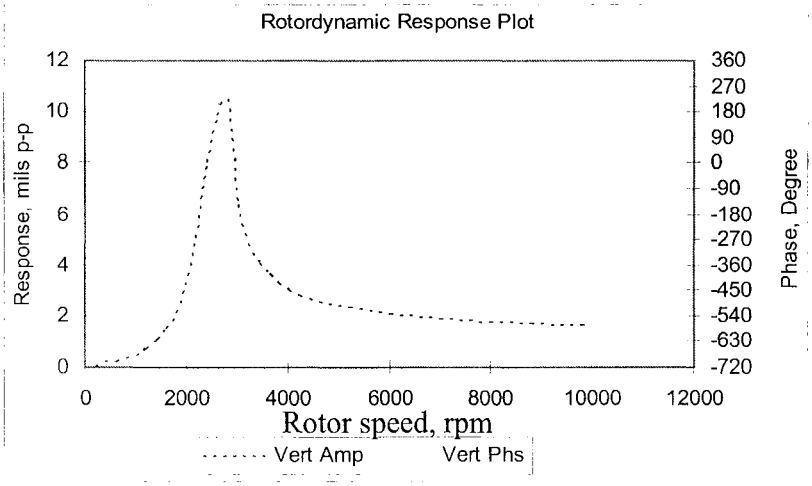

Figure 4-25 Vertical response showing critical speed

Calculated root locus (Figures 4-26 and 27) provides information about the stability status of the model. Figure 4-26 reveals that a specific solution to the natural frequencies in the range 2300-2700 cpm is prone to instability due to the value of damping coefficient being positive. When the instability data is mapped with the shaft speed, Figure 4-27 can be formed and hence one can find the startup of instability in terms of speed. For the specific example illustrated here as a model, the threshold of instability is 3900 rpm. This is decided from the fact that the damping exponent becomes positive after this speed. The vibration amplitude above this speed is unstable.

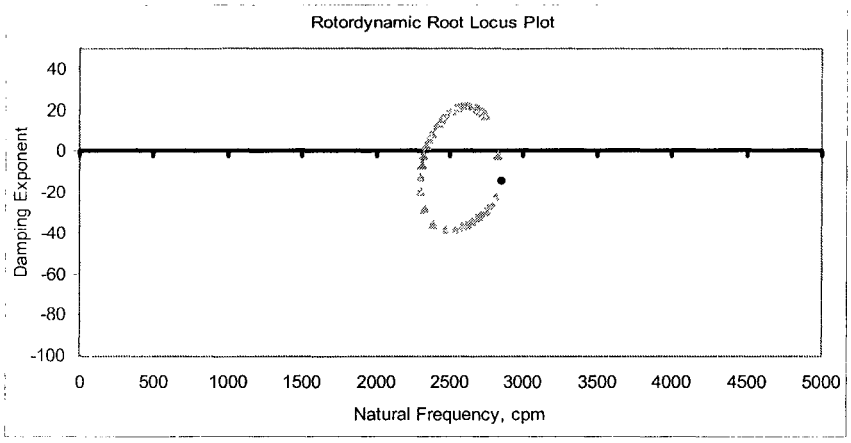

Figure 4-26 Stability of natural frequencies

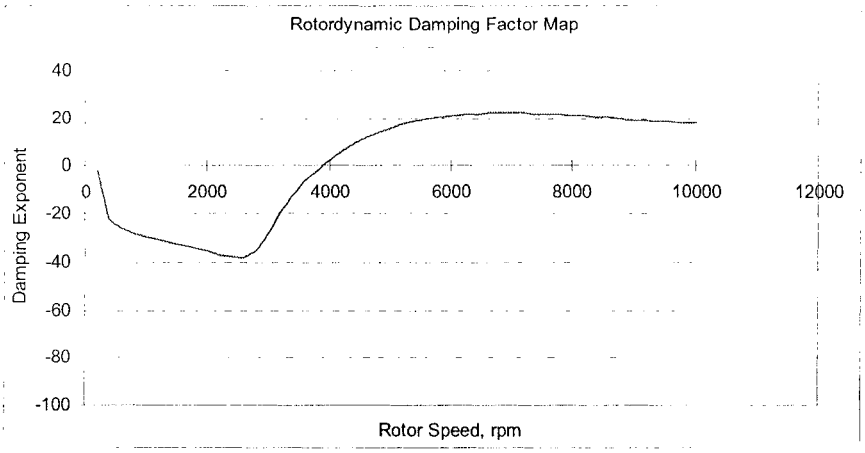

Figure 4-27 Damping exponent vs. rotor speed

4.4 Effect of Disk Location and Shaft Length

All of the previous plots were taken from the model with a single set up. For the current section, series of runs were performed in order to track the changes in the instability response of the system due to the change on the shaft length and disk axial location.

4.4.1 Effect of Disk Location

Figure 4-28 is the threshold of instability trend for a model with the shaft length of 300 mm. Notice the increasing trend in threshold of instability. A good correlation was noticed of third order which is labeled as Poly in the figure. There was found a qualitative change in trend for other shaft lengths, refer to Figures 4-28 to 30.

Figure 4-29 is taken from the runs for a longer shaft length (l= 400 mm). First thing to notice is the rise of the threshold of instability with the same starting (Station 2) and the reduction of threshold for the last station (Station 18). Another observation is the change in the response of the system when the disk is located in the first half of the shaft, where the threshold of instability is not significantly increasing, unlike the second half of the shaft. The mid span acts as border point between the two episodes of response. These observations suggested to increase the shaft length further, l=600 mm, to evaluate the response (Figure 4-30). Contrary to the previous trends which show increasing and flat trends, the threshold for the first half of the shaft showed a reduction in the threshold of instability for this setup. This implies that moving the disk far away from the fluid film bearing may rather worsen the instability for the first half of the shaft. Actually, the threshold of instability is minimum in the mid span and increases afterwards. Figure 4-31 gathers five trends for comparison.

Each of the curves shown in Figures 4-31 presents the results of eight models in terms of non-dimensional disk location. As mentioned previously, bearing load was affected by the disk location. This accommodation was not dealt with in the literature and an assumption was made to ignore the disk loading effect on the bearing load. In the models, the disk was moved from station two (closest to the fluid film bearing) to station 18 (closest to the sleeve bearing). To have comparable results, station numbers are used rather than the physical length, and so, each step movement is 10% of the total shaft length.

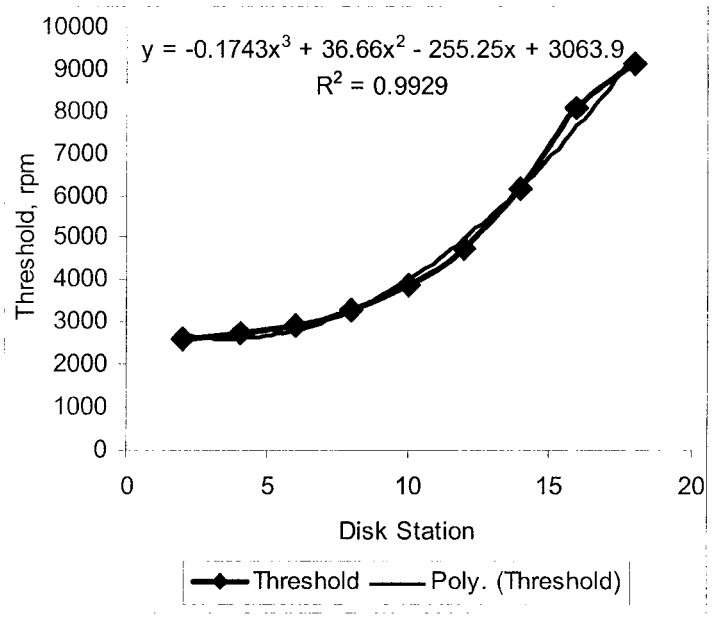

Figure 4-28 Effect of disk location on threshold for a shaft length of 300 mm

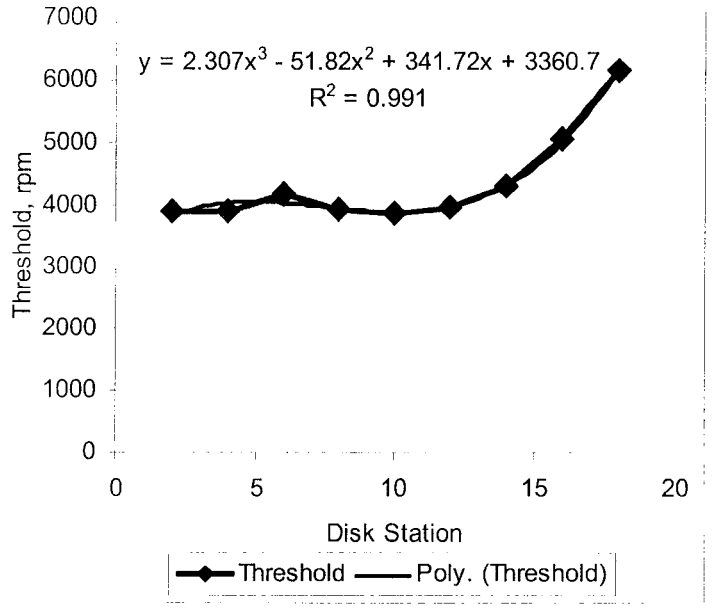

Figure 4-29 Effect of disk location on threshold for a shaft length of 400 mm

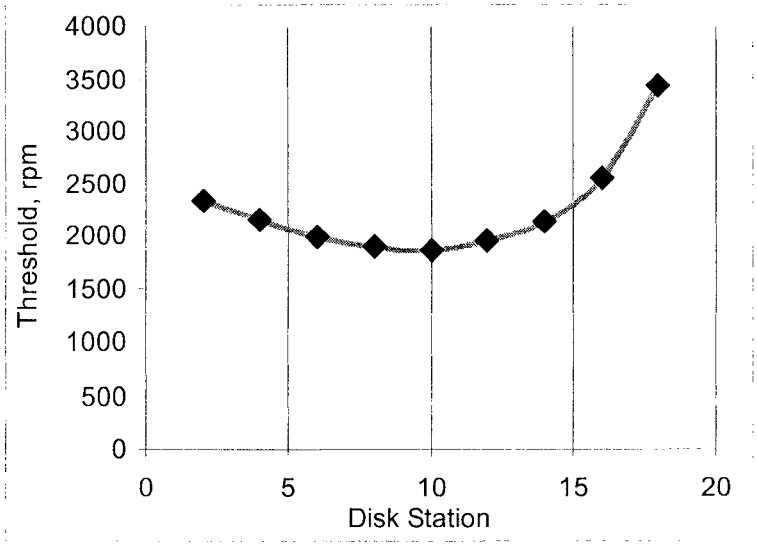

Figure 4-30 Effect of disk location on threshold for a shaft length of 600 mm.

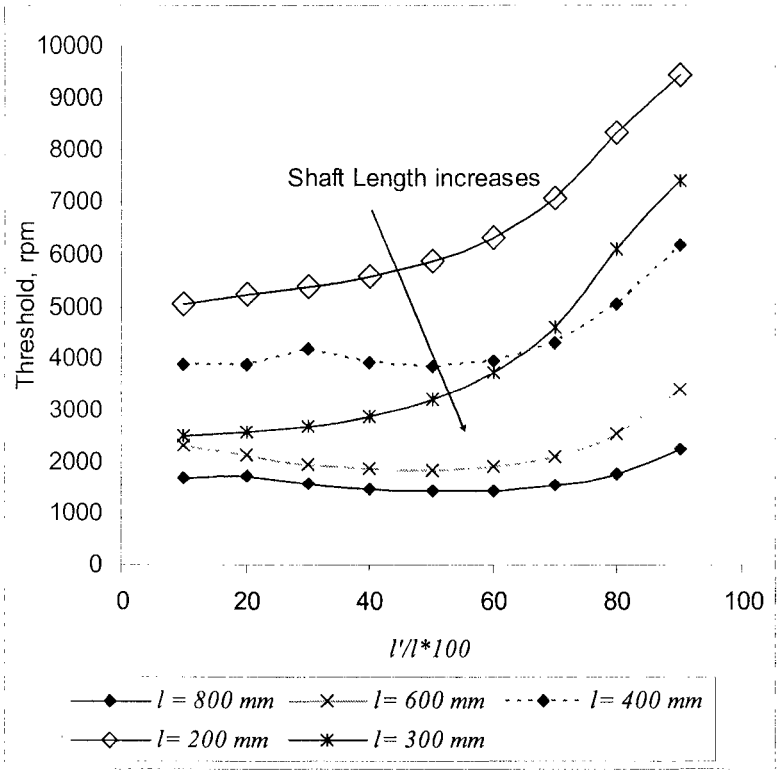

Figure 4-31 Effect of disk location on threshold for different shaft lengths

4.4.2 Effect of Shaft Length

A similar approach was done to evaluate the effect of the shaft length on the threshold of instability. The results are plotted in Figure 4-32, in terms of non-dimensional shaft length.

The general effect of increasing shaft length is to reduce the threshold of instability. With the shaft length increase, the threshold of instability approaches an asymptotic lower limit, regardless of disk location. However, it was noticed, as discussed in the last section, that the effect of both shaft length and disk location are linked together. This link is more pronounced in the cases of shorter shafts. Notice the large effect of the disk location in the case $l/2R = 20$ shaft length compared to the minor effect on comparing to $l/2R = 80$.

Moreover, it is clear from the same figure that there are two main episodes of response, before and after Station 15 ($l'/l = 0.75$). When the disk location is in station 15 or further, the shaft length has a definite decreasing effect on the threshold of instability. However, if the disk is closer than Station 15 to the fluid film bearing, the shaft length effect may decrease or increase the threshold of instability depending on the disk location.

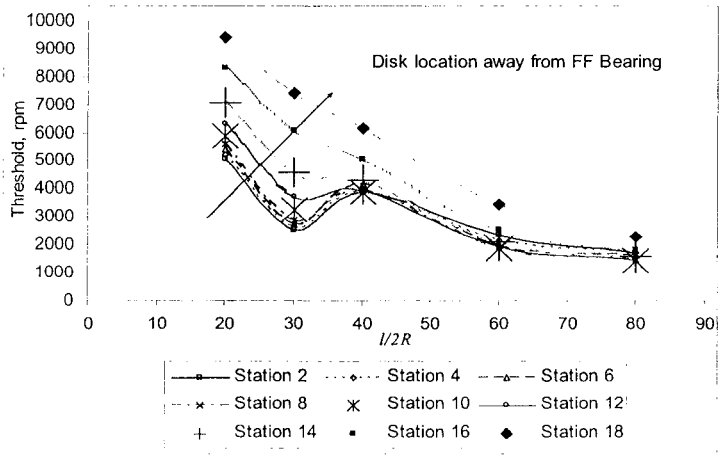

Figure 4-32 Effect of l on the threshold

4.5 Generating/Improving Plots

Due to the limitations found in the ADRE, as discusses in the previous chapter, the vibration data was exported to spread sheet environment for further processing and producing other plots. In this section, the mathematics used to produce those plots is presented briefly along with sample calculations.

Some plots were generated just by imposing some variables from different tests on the same plane- an important analysis feature that was not available in the ADRE program. An example for this is the Bode plot for tests with different unbalance masses. See Figure 3-25. Other plots were not raw data and codes similar to those used in ADRE were adapted. Figure 4-33 shows the regenerated SACL plot as a first step in generating the other plots. Figure 4-34 is for the same data processed from ADRE, given just for comparison. The flow chart in Figure 4-35 is used to produce Figure 4-33. In this two dimensional plot, the corresponding signal is stored as negative gap voltage which is related to the physical relative distance between the shaft and the probe. Using the technical specifications of the instrumentation system, the gap voltage can be converted to horizontal and vertical physical relative distances. After some further processing, the SACL is constructed by plotting the compensated vertical distance versus the compensated horizontal distance. Sample calculation on raw data (Table 4-4) is presented to calculate SACL as follows:

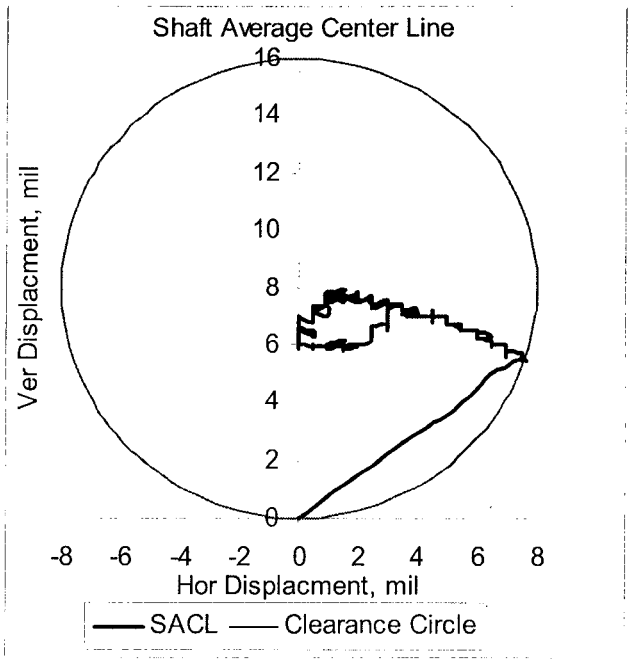

Figure 4-33 SACL regenerated plot

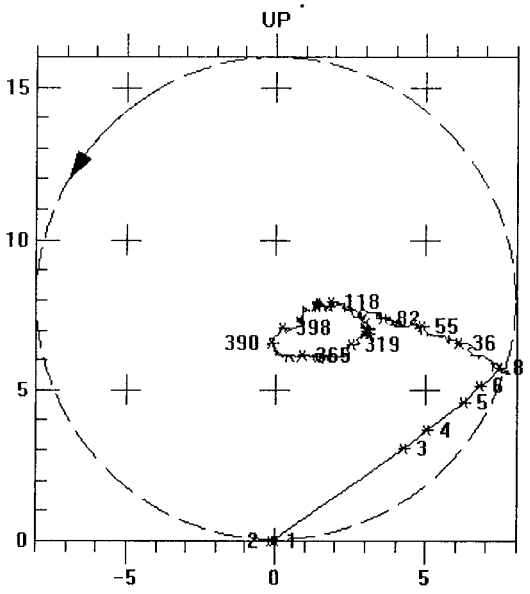

Figure 4-34 SACL produced by ADRE

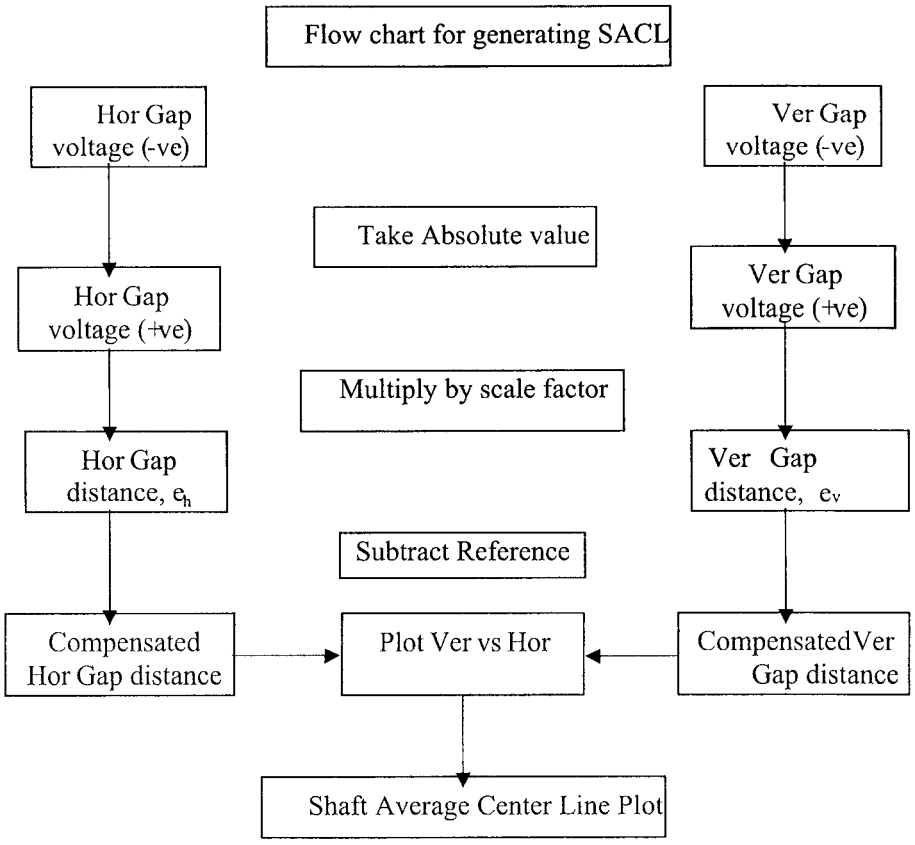

Figure 4-35 Flow chart for generating the SACL plot

Table 4-4 Sample calculations for SACL plot

Sample number	Shaft Speed, rpm	Vertical Gap Voltage, V	Horizontal Gap Voltage, V	Ver Distance, mil	Hor Distance, mil	Compensated Ver Distance, mil	Compenstade Hor Distance, mil
2	0	-10.2	-11.5	51	57.5	0	0
3	350	-9.62	-10.7	48.1	53.5	2.9	4.29
24	670	-9.02	-10.1	45.1	50.5	5.9	7

Referring to Table 4-4, Sample 2 is for static shaft, where the shaft is in direct contact with the bearing, Sample 3 is for slow role condition and Sample 24 is for a speed above the slow role condition.

For Sample 2:

Absolute value of the vertical probe Gap Voltage (V DC) = 10.2 V DC

Absolute value of the horizontal probe Gap Voltage (V DC) = 11.5 V DC

Distance between the shaft and vertical probe = 10.2 V DC/ 0.2 (V DC/mil) = 51.0 mil (The scale factor for the probe used is 0.2 V/mil)

Distance between the shaft and horizontal probe= 11.5 V DC/ 0.2 (V DC/mil) = 57.5 mil

The above two distances will be considered as reference (0,0) i.e. origin of the SACL plot for the coming calculations.

For Sample 3:

Distance between the shaft and vertical probe= 9.62 V DC/ 0.2 (V DC/mil) = 48.1 mil

Distance between the shaft and horizontal probe= 10.7 V DC/ 0.2 (V DC/mil) = 53.5 mil

Compensated vertical relative distance= 51.0-48.1=2. 9 mil (upward)

Compensated horizontal relative distance= 57.5-53.5=4.29 mil (to the right)

Calculations of other samples, e.g. Sample 24, are the same.

The shaft average eccentricity ratio (ε) plot is constructed based on the flow chart in Figure 4-36. First, the eccentricity is calculated for both the horizontal and vertical coordinates of the shaft position, with respect to the bearing's center. Then, the eccentricity from its horizontal and vertical components is calculated as a vector (magnitude and angle), and plotted as a function of shaft speed.

Both compensated horizontal and vertical distances are calculated as in the SACL plot. Sample calculation of the ε plot, based on Table 4-5, is as follows:

For Sample 3:

Horizontal Eccentricity, eh = compensated horizontal distance-0 (since the shaft starts moving from zero on the horizontal axis)= 4 mil

Vertical Eccentricity, e_v = compensated vertical distance -8 (since the shaft starts moving from the lowest point in the vertical axis, i.e., the radial clearance) = -8+2.9= -5.1 mil. Hence, ε is found as

$$\varepsilon = \sqrt{e^2{}_h + e^2{}_v}\ /C = 0.810$$

Attitude angle, ϕ = $\tan^{-1}$(vertical eccentricity/ horizontal eccentricity) $*180^\circ/\pi$ $+90^\circ = \tan^{-1}(-5.1/4) *180^\circ/\pi +90^\circ = 38.1^\circ$

Notice that the additional 90° is to have the vertical axis as the starting point, refer to Figure 4-5.

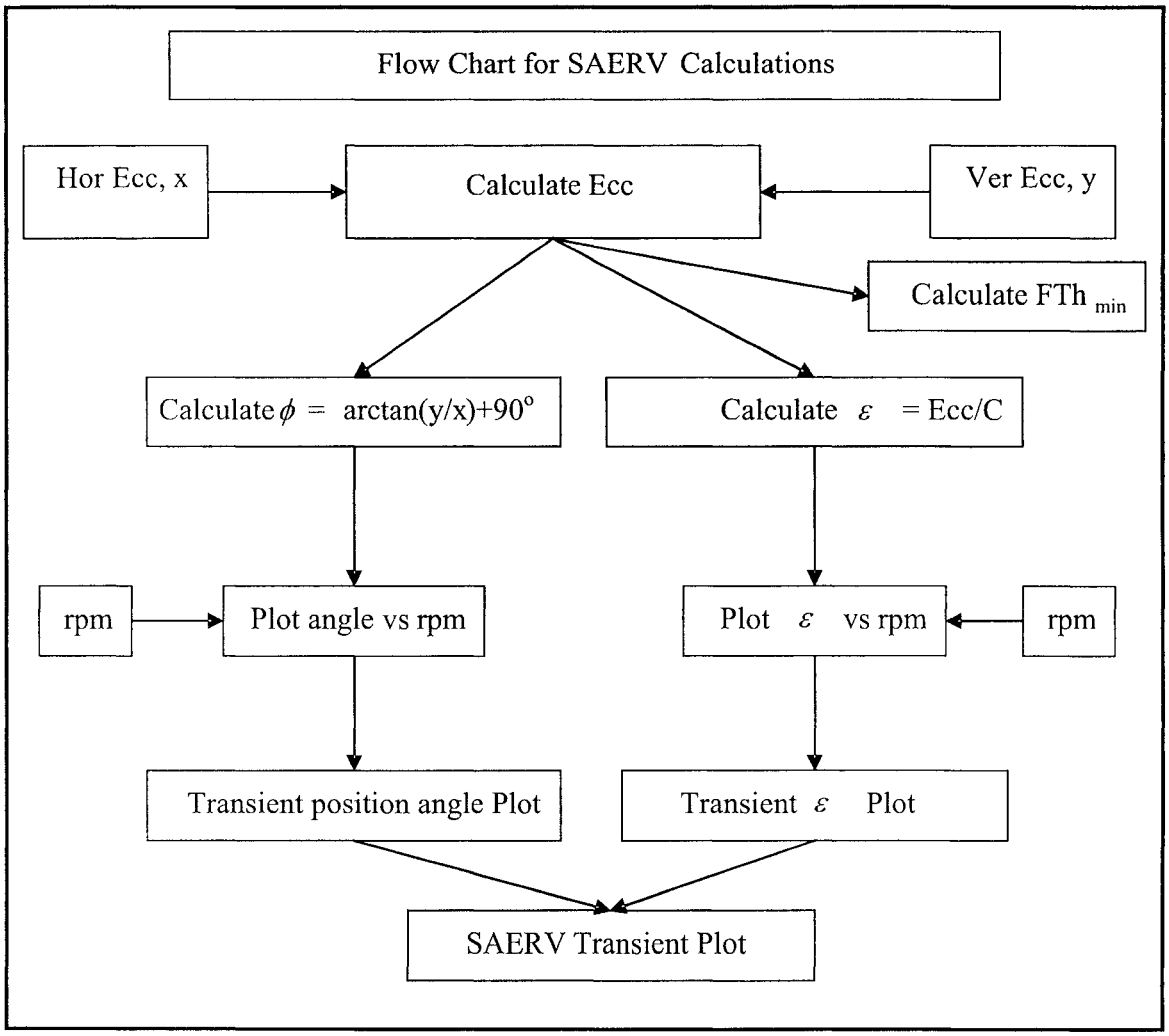

Figure 4-36 Flow chart for ε calculations

After the calculation of ε for all samples, a mapping between the variables can be made to generate the plots of interest in terms of ε. An example plot is given in Figure 3-34.

Table 4-5 Sample calculation of ε

Sample	Speed, rpm	Compensated Hor Disp, mil	Compensated Ver Disp, mil	Hor Ecc, mil	Ver Ecc, mil	Ecc Magnitude, mil	ε	Attitude angle, deg
1	0	0	0	0	-8	8	1	0
2	0	0	0	0	-8	8	1	0
3	350	4	2.9	4	-5.1	6.48	0.810	38.1
4	370	5	3.5	5	-4.5	6.72	0.840	48.0
5	391	6	4.45	6	-3.55	6.97	0.871	59.3

CHAPTER 5

CONCLUSIONS AND RECOMMENDATIONS

This chapter provides a summary of the conclusions drawn from both experimental and numerical works in addition to some comments on the experiments and recommendations for future work.

5.1 Concluding Remarks

The main types of fluid induced vibrations encountered with radial fluid film bearings, oil whirl and whip, are affected by bearing design, lubrication system and rotor configurations (which are studied in this thesis). Fluid related natural frequencies of the system are heavily dependant on the rotor speed and the behavior of the shaft journal inside the fluid film bearing.

Whirl and whip are more dangerous than the synchronous vibration because damping plays a limited role in controlling the vibration amplitude in this case unlike what happens in a typical mechanical resonance where damping suppresses the vibration amplitudes. Also, compared to the traditional resonance, the whirl will not stabilize with increasing the shaft speed because the natural frequency moves with the speed. This fact was seen in both experimental and theoretical works.

The disk location from the fluid film bearing, l', shaft length, l, and unbalance mass, m_u, of the rotor were examined by a series of tests conducted on

the rotor kit. The standard plots of orbit, SACL, cascade and other plots were helpful in the analysis.

Experimental raw data were exported to compare and generate new variables which were very helpful in understanding the problem. A critical speed comparison is presented in Table 5-1. Clearer picture of the rotor behavior was found by tracking response versus transient average eccentricity ratio vector.

Table 5-1 The ε as a function of speed

l'	l	Numerically Predicted Critical Speed	Experimental Critical Speed	Difference %
60	400	4600	5200	11.5
120	400	3000	3420	12.2
200	400	2600	2820	7.8
280	400	3000	3070	2.3

The computational work dealt with the changes on the instability vibration signature due to altering the mechanical structure of the system: disk location and shaft length. The orbit, time waveform, spectrum and other plots were used for the analysis. In addition, the stiffness and damping calculations were preformed for the rotor kit set up.

Increasing effect on the instability threshold and instability frequency were revealed by moving the disk away from the fluid film bearing. The disk location was found to be a prominent factor on the threshold of instability. It even affects the response related to the other two parameters, l and m_u.

The shaft length was found to be reducing the instability threshold in a nonlinear way. Tests were done with similar configurations (e.g. disk was kept in the mid span) to remove the effect of disk location.

Although the mass unbalance produces synchronous vibrations, it also influences the subsynchronous instability especially around the critical speed range and reduces its amplitude in some cases. Explanation of the reduction was found from the shaft average eccentricity ratio vector plots, where the unbalance force pushes the shaft to a higher eccentricity and reduces the subsynchronous instability vibrations on the expense of increasing the synchronous vibration amplitude.

The unbalance has a minor effect on the instability frequency. This was found true even if the unbalance force was large (more than 6 times the system's weight itself, in some cases). The general trend for the instability threshold is that it decreases with the increase in the unbalance weight, m_u.

The value of the shaft average eccentricity ratio, ε, may be used for predicting the stability threshold. This could be misleading because the bearing properties are dependant on the shaft position, which is *not static*. One has to check carefully the difference between the effects of the following points:

- As the speed increases, the ε decreases and the bearing effective stiffness will decrease.

- As the speed increases, the *dynamic* shaft eccentricity ratio may/may not increase depending on the applied forces and existing stiffness. Nevertheless, if the dynamic shaft eccentricity ratio increases the bearing stiffness will also increase.

The shaft average eccentricity ratio, ε, works as a limiting factor for the journal's motion because the vibration amplitude cannot exceed the bearing clearance, i.e., the value of ε value cannot exceed 1.

The instability vibration amplitude will increase until a limit cycle will be reached, when the instability vibration amplitude increases to the diameteral clearance of the fluid film bearing clearance. This perfectly explains the reasons behind starting the instability and reaching to a constant vibration amplitude thereafter in all the experiments.

In other words, though the vibration amplitude is an effect, the amplitude itself is also an important cause to change the bearing properties especially if the amplitude is large. In the bearing property charts, the large vibration amplitudes are represented by large eccentricities (smaller Sommerfeld numbers) which are related to very high values of bearing stiffness. Those cases are to the left of the Sommerfeld number charts.

Since the whirl/whip vibration is a circular orbiting, the corresponding reaction forces (stiffness and damping) will be also rotating and they will have a cycling frequency. If this concept is combined with the fact that the instability vibration has a certain frequency, one can conclude that during the instability the bearing properties are also increasing or decreasing in the periodic fashion with a frequency equal to the vibration frequency $\lambda\Omega$ for the whirl and rotor natural frequency for the whip.

Another representation to this scenario can be built if the shaft motion is traced as the whirl/whip vibration moves. In this case the minimum fluid film thickness ($= 1 - \varepsilon C$) will be known and constant in value but yet moving with time around the bearing clock. If a coordinate transformation is introduced, the motion of the fluid film thickness can be frozen. An equivalent interpretation was given by Muszynska in [1].

Instability vibration behavior was found to be unrepeatable in the case of startup compared to the shutdown as can be seen from Figure 5-1. For a system

with a potential instability, the ε reduces with the speed as shown from the numerical prediction in Figure 5-2 for a particular case. There exists three ranges concerning the stability (Figure 5-3) based on the large number of the experiments conducted:

1. Totally stable range: according to a statistics made on the experimental setups, the rotor is always stable when the speed is 2320 rpm or less.

2. Start up stable range: this covers a range of speed above the previous range and before the threshold of instability. This region is stable in the startup but not stable during shutdown once the system has gone into instability.

3. Totally unstable: after the instability starts with increasing the speed, regardless of increasing or decreasing speeds.

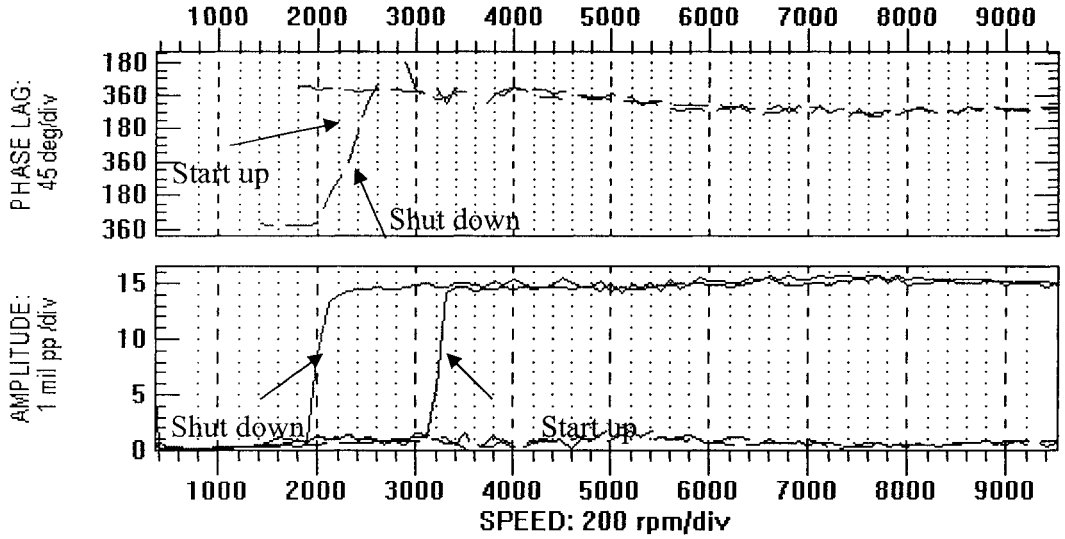

Figure 5-1 Effect of hysterisis on repeatability response

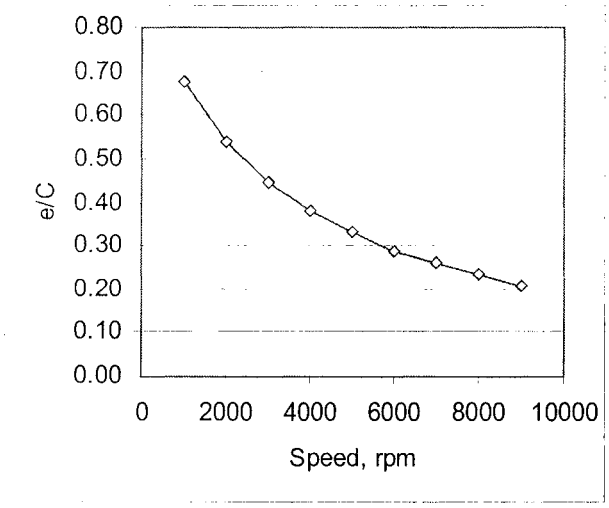

Figure 5-2 Behavior of ε as speed increases

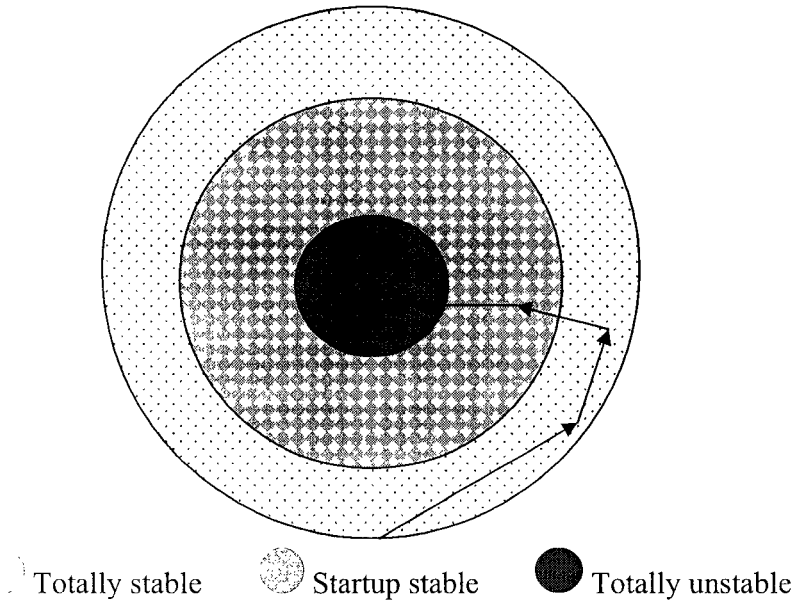

Figure 5-3 Stability regions

It was also noticed that a frequency jump may occur at higher speeds, where the instability vibration mode shape can change. Refer to Figure 5-4, for the two cases of increasing and decreasing the instability frequency. In such cases, the shaft average centerline also shows a noticeable cycling around its center (Figure 5-5).

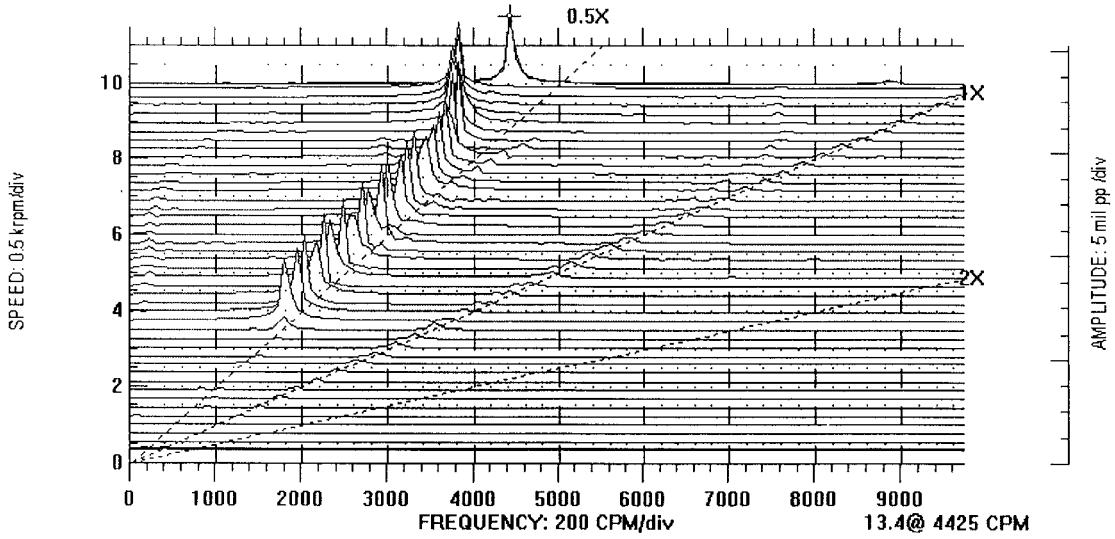

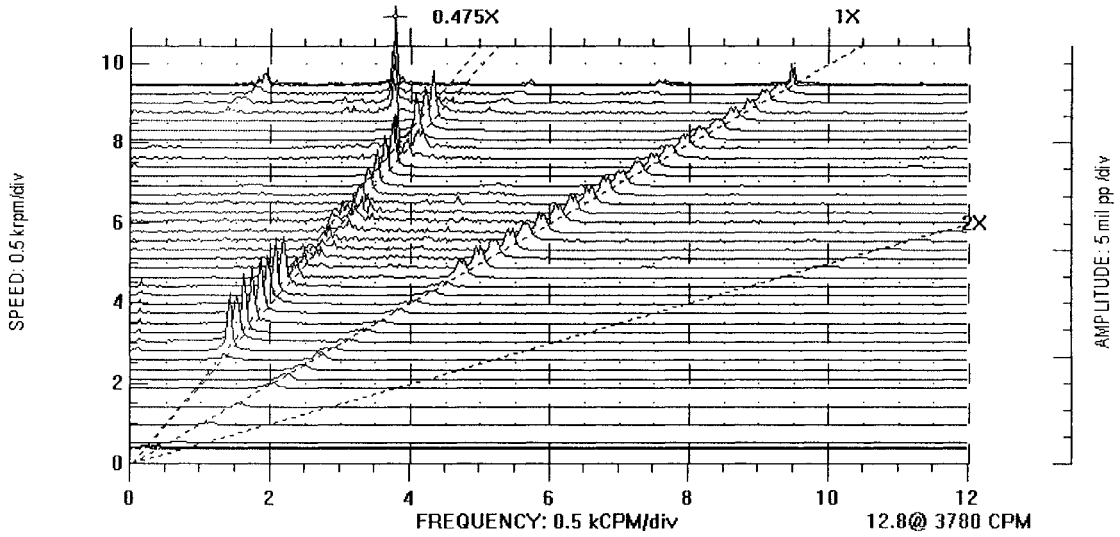

Figure 5-4 Sudden increase (up) and decrease (down) in instability frequency

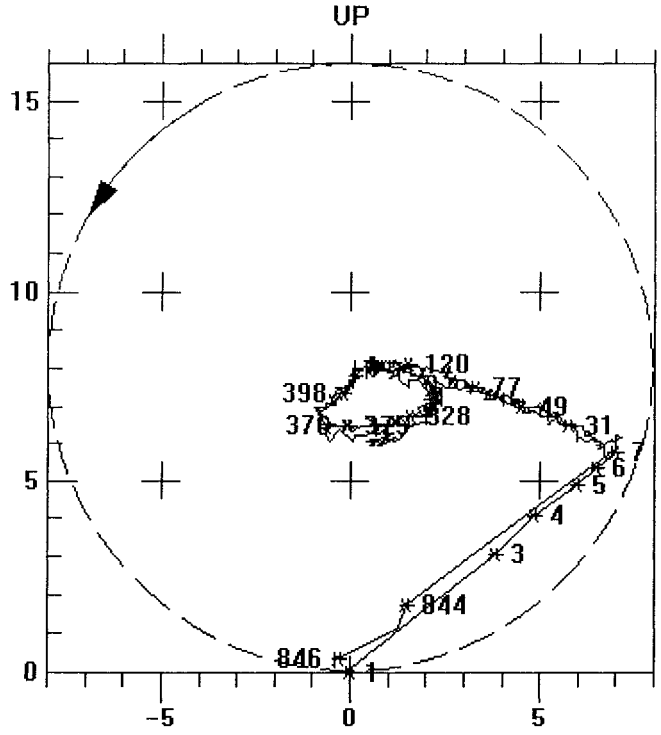

Figure 5-5 SACL cycling

After exporting and analyzing the raw experimental data, the relation between the rotor speed and instability frequency was found overlapping despite of the ramp (startup or shutdown) in the transient conditions. Tracking whirl frequency showed excellent linearity where the slope is the instability order. Available data acquisition cannot process such variable order tracking. An example is shown in Figure 5-6.

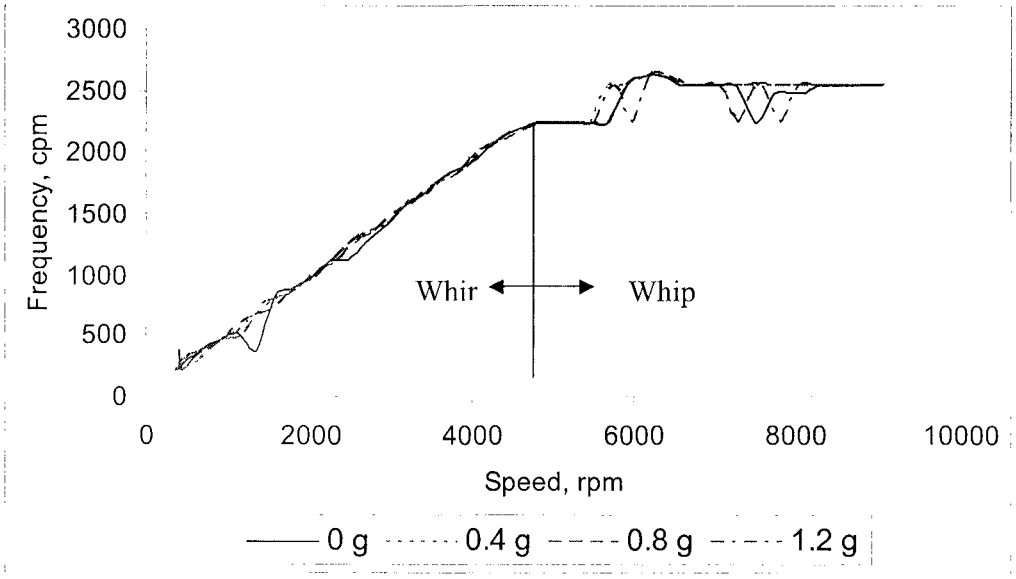

Figure 5-6 Linear relation shows a slope of order

5.2 Comments on Setup

Oil discharge pressure was adjusted manually prior to and during the experiment. A difficulty is faced in keeping a steady pressure value. The pressure jumps suddenly at two instances: when the instability appears (startup) and when it disappears (shutdown). A typical pressure change is of 0.3 psi.

For research purpose it is better to improve the frequency resolution to 10 cpm by increasing the resolution. Another alternative is applying the interpolation equations developed in applied vibration engineering field. This feature is utilized

for instance in CSI instruments but could not be applied on the experiments because the ADRE cannot export the dynamic/spectral data.

Ramp rate (up and down) could be adjusted to less than 5000 rpm/min. Experiment time consumed is directly proportional to the ramp rate. Most of the experimental data were collected under the following conditions:

Spectral Lines, *N*, were 400 lines (ADRE/DAUI system is limited to either 400 or 3200 lines). *Frequency Span*, F_{max}, was 30000 cpm and 12000 cpm in some cases to zoom the results. Applied *Window* was *Hanning*. Ramp rate was 5000 rpm/min. Based on this information, some data acquision and signal processing parameters of concern are as follows:

The resulted min resolution frequency resolution = F_{max}/lines:

12000 cpm/400 = 30 cpm (for the plots with F_{max}=12000 cpm)

30000 cpm/400 = 75 cpm (for the plots with F_{max}=30000 cpm)

Data acquisition time, DAT= N/F_{max} = 400/150 = 2.66 sec at 150 Hz (9000 rpm).

The 8-revolution data acquisition time, 8-rev DAT = 8* (1/150) = 0.0533 sec at 150 Hz (9000 rpm).

Approximate number of samples collected during each experiment (startup and shutdown) is: 800-880 *Vectors* and 60-90 *Waveforms*. The samples are sufficient but recommended to be increased to 1200 and 100, respectively. A finer sampling based on speed triggering can be applied close to the instability threshold region.

5.3 Recommendations for Future Study

Future studies are recommended to cover the parameters of the fluid film bearing itself, such as the oil pressure, viscosity and flow rate.

A feedback signal and automated control system is recommended to control the pump pressure inaccuracy and to avoid the sudden pressure changes due to the whirl/whip.

Measures are needed to isolate the test foundation from the test rotor to avoid any foundation structural resonance. It is advisable to improve the mounting of the kit on the table to prevent major structural natural frequencies below 20000 cpm.

To enhance the numerical output, it is recommended to impose the experimental shaft position and vibration values in the evaluation of the bearing parameters (stiffness and damping). A suggested flow chart is presented in Figure 5-7.

Improvement of accuracy on the vibration amplitudes will not result in extra information. This is true because the order of the amplitude error is negligible compared to the actual amplitude values. Frequency accuracy is a possible area to improve. This may include an increase in spectral lines, reduction in ramp rate and increase in data acquisition speed as discussed in the signal acquisition and processing.

For the instability applications (for known frequency range of interest), the use of broadband filters for 0.4X to 0.5X is helpful in trending rather than specific frequency, e.g. 0.475X. Tape recorder is an excellent choice for post experiment signal processing. If possible, one can use a hardware/software with higher resolution lines. Furthermore, a software can be utilized to find the interpolated frequencies to improve the accuracy of the frequency and amplitude values.

It is also good to use a software with the ability of exporting all data to other environments in a tabular format. Available commercial ADRE versions are able to export vectors but not the spectra or waveforms.

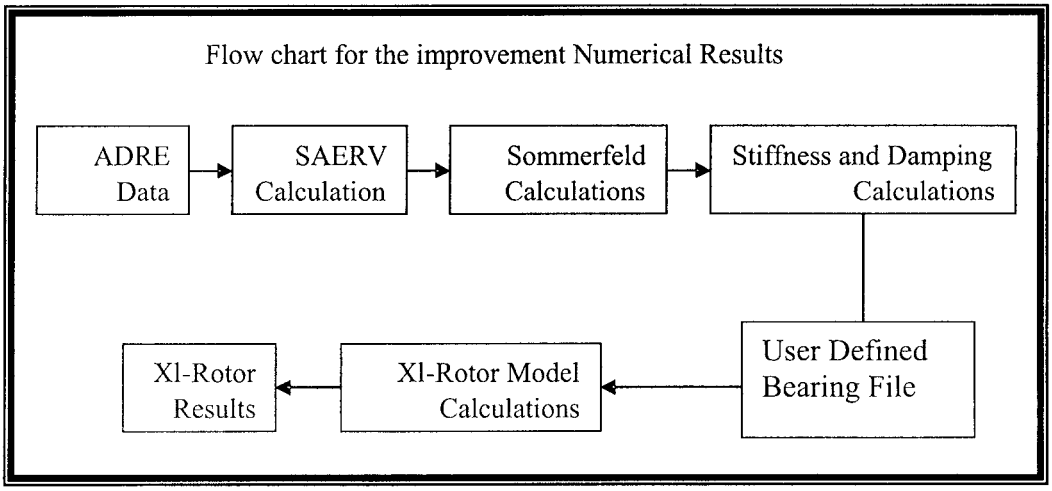

Figure 5-7 Flow chart for experimental based bearing properties calculation

References

[1] Muszynska, A. Whirl and Whip-Rotor/Bearing Stability Problems. Journal of Sounds and Vibration. Vol. 110(3), pp 443-462. 1989.

[2] Muszynska, A. Fluid–Induced Instability of Rotors: Whirl and Whip-Summary of Results. Vibration and Noise.

[3] Oravsky, Vladimir. Some Types, Classification and Definitions of Instability in Rotating Machinery. ISCORMA1 Paper. 2001.

[4] Bently, D.E. and Goldman, P. Destabilizing Effect of the Aerodynamic Forces in Centrifugal Compressors. ISROMAC-7, Feb. 1998.

[5] Muszynska, A. Synchronous and Self-Excited Rotor Vibrations Caused by a Full Annular Rub. Proceedings of the Eighth Machinery Dynamics Seminar". Canada. pp 22.1-22.21 .October 1984.

[6] Lund, J.W. Stability and Damped Critical Speeds of Flexible Rotors in Fluid Film Bearings. Journal of Engineering for Industry. pp 509-517. May 1974.

[7] Lund, J.W. and Saibel, E. Oil Whip Whirl Orbits of Rotor in Sleeve bearings. Journal of Engineering for Industry. pp 813-823. Nov. 1967.

[8] Lund, J.W. and Orcutt, F.K. Calculations and Experiments on the Unbalance Response of Flexible Rotors. Journal of Engineering for Industry. pp 785-795. Nov. 1967

[9] Elshman. Rotor Dynamics and Balancing. Short course notes. Vibration Institute Press.

[10] Harris, Cyril M. Shock and Vibration Handbook. McGraw-Hill 2nd Ed. 1976.

[11] Shapiro, W and Colsher, R. Dynamic Characteristics of Fluid-film Bearings. Turbomachinery Symposium. P 39. 1977.

[12] Jang, G.H. and Kim, Y.J. Calculations of Dynamic Coefficients in the Hydrodynamic Bearing Considering Five Degrees of Freedom for a General Rotor Bearing System. Journal of Tribology. Vol 121. pp 499-505. July 1999.

[13] Rao, T.V.V.L.N. and Biswas, S. An Analytical Approach to Evaluate Dynamic Coefficients and Nonlinear Transient Analysis of Hydrodynamic Journal Bearing. Tribology Transactions. Vol 43(1) pp 109-115. 2000.

[14] Bently, D.E. Advanced Machinery Dynamics Course. Bently Nevada Short Course Notes. Oct 1999.

[15] RBMware User's Manual. Computational Systems, Inc. 2002.

[16] Data Manager 2000 Configurations. Bently Nevada Best Practices Report. 2002.

[17] Muszynska, A. The Fluid Force Model in Rotating Machine Clearances Identified by Modal Testing and Model Applications. ISCORMA1 Paper. 2001.

[18] Bently, D.E. How to Detect and Identify Fluid Induced Instabilities. Applied Machinery Diagnostics Short Course. Bently Nevada. 2000.

[19] Muszynska, A. and Bently, D. E.. Anti-Swirl Arrangements Prevent Rotor/Seal Instability. Journal of Vibration, Acoustics, Stress and Reliability in Design. ASME Transactions April 1989, Vol. 111 pp 156-162.

[20] Muszynska, A. and Bently, D.E.. Rotor Active "Anti-Swirl" Control.

[21] Muszynska, A. Improvement in Lightly Loaded Rotor/Bearing and Rotor/Seal Models. Journal of Vibration, Acoustics, Stress, and

Reliability in Design. ASME Transactions.. Vol 110 pp 129-136. April 1988

[22] Ganesan, R. Nonlinear Vibration and Stability of a Rotor –Bearing System with Nonsymmetric Clearances. Journal of Engineering for Gas Turbine and Power. ASME Transactions. April 1997.

[23] Tam, L.T, Muszynska, A. and others. Numerical and Analytical Study of Fluid Dynamic Forces in Seals and Bearings. Journal of Vibration, Acoustics, Stress, and Relaibility in Design. ASME Transactions. Vol 110 pp 315-325. July 1988.

[24] Muszynska, A. Identification of Modal Parameters of Rotating Systems Using Perturbation Techniques. Twelfth Biennial ASME Conference. Mechanical Vibration and Noise. pp 1-6 .Sep. 1989.

[25] Wang, Nenzi and Ho, Chang-Li. Engineering Optimum Design of Fluid Film Lubricated Bearings. Tribology Transactions. Vol 43(3) pp 377-386. 2000.

[26] Muszynska, A. Multimode Whirl and Whip in Rotor /Bearing Systems. Bently Rotor Dynamics Research Corporation.

[27] Bently, D.E. Dynamic Stiffness Measurements of Rotating Machinery. Presentation. Turbo Machinery Symposium. Sep 1998.

[28] ISO 1940-1: Mechanical Vibration - Balance Quality Requirements of Rigid Rotors - Determination of Permissible Residual Unbalance. 1986.

[29] Leader, Malcolm E. Understanding the Journal Bearings. Reprint in [9] pp 77-88.

[30] Jackson, Charles and Leader, Malcolm. How to Avoid Operating Problems. Hydrocharbone Processing. Nov 1979.

[31] Bently, D.E and Muszynska, A. Why Have Hydrostatic Beariungs Been Avoided As A Stability Element For Rotating Machines?. Bently Rotor Dynamics Research Corporation.

[32] Rotor Kit RK4 Manual. Fluid Film Option Manual (Rotor Kit RK4). Bently Nevada.

[33] ADRE 4.9. Automated Data Acquisition for Rotating Equipment, Bently Nevada. 2002.

[34] Goodwin, M.J. Dynamics of Rotor-Bearing Systems. Unwin Hyman Ltd. 1989.

[35] Andrés, Luis San. Lubrication Theory. Course Notes. http://www.mengr.tamu.edu:70/mechanics-systems/lsanandres/me626/notes/default.htm 2000.

[36] Rao, J.S. Rotor Dynamics. John Wiley & Sons. New Delhi 1983.

[37] Murphy, B. Xl-Rotor: Rotor Dynamic Spread Sheet. 2003. www.xlrotor.com

VITAE

Name: Ali Muhammed Ali Al-Shurafa

Berth Date: 22/10/1976

Education: B.S. in Mechanical Engineering from KFUPM, Dhahran. Second Honor. 1999.
M.S. in Mechanical Engineering from KFUPM, Dhahran. 2004.

Experience: 2000-2003 Vibration engineer in Saudi Electricity Company.
2003-present Faculty member in Mechanical and Manufacturing Engineering Technology Department. Jubail Industrial College. Jubail.